

Copyright
by
Lingyuan Gao
2018

**The Dissertation Committee for Lingyuan Gao Certifies that this is the approved
version of the following Dissertation:**

**Oxygen Vacancy Roles in Transition Metal Oxides and Related
Heterostructures**

Committee:

Alexander A. Demkov, Supervisor

James R. Chelikowsky

Allan H. MacDonald

Keji Lai

Graeme A. Henkelman

**Oxygen Vacancy Roles in Transition Metal Oxides and Related
Heterostructures**

by

Lingyuan Gao

Dissertation

Presented to the Faculty of the Graduate School of

The University of Texas at Austin

in Partial Fulfillment

of the Requirements

for the Degree of

Doctor of Philosophy

The University of Texas at Austin

August 2018

Dedication

To my parents

Acknowledgements

Born in Urumqi, a very remote city (in the center of Asia) from developed area of China, I never expected that I would go so far in my life. For many kids educated in China, at young age they are highly expected to be scientists in the future. However, with time going on, most of them make some other wise choices for their lives. After so many years, I gradually understood that the high expectations of parents originate from the honorable feeling when their kids get a high score. I'm on this route, probably stimulated by the physics Olympic contest at a high school stage: ranking in the top 20 out of all students of a whole province, I could have gone straight to a university, without any other tests. However, I missed that chance, partly as I messed up with the experimental part (That's why I couldn't be an experimentalist, I guess). But after being admitted to the Peking University, I still chose physics as my major. After four years of study, I went abroad and started my pursuit of a PHD at the University of Texas at Austin.

Looking back from now, there are so many people that I need to acknowledge. Without their help, I couldn't stand where I am today.

The first person I need to acknowledge is my advisor Alex Demkov. The first time I met Alex was in a solid state class in the Fall of 2012. Allan couldn't come, so Alex taught for him. I still remember what Alex taught on that day was about the Fermi distribution. He left me with an impression of a lot of smiles and that he could write down formulas without any pause. "Hmm, he should be a nice person", that was his first impression on me. At my second semester, I took a quantum mechanics class with Alex. At that time, I was still working on plasma and gradually realized this was not what I truly wanted to do, but I was still hesitating then. I talked to Alex many times during his

office hours and those conversations benefited me a lot. Finally, I made up my mind and joined the group in the January 2014.

I still remember how I was like when I initially joined the group. It seemed I was interested in nothing and I couldn't help with being asleep at group meetings, until Alex talked to me. Then I realized though he had a nice personality, he was serious and rigorous about working. That finally woke me up and pushed me back on the road. Throughout these four years, he gave me so many insightful ideas, helped me solve tons of academic issues, supported me financially, shared precious life experiences with me, excited and encouraged me when I was in a low mode, reassured me when I was in panic, and finally led me on the way of exploring the scientific world. His devoted, careful, courageous and optimistic attitude towards both work and life greatly affects me and I will bear that in mind forever.

The second person I need to acknowledge is our former postdoc Chungwei Lin. Chungwei is such a brilliant scientist and has a very good understanding of physics. Apart from being knowledgeable, he is patient and nice to explain my questions in details. Though we have only communicated for one year locally, I learned a lot from him during this process. Even when he moved to Boston, he is still willing to discuss with me and glad to help me in every aspect of my work.

I also need to acknowledge Prof. Allan MacDonald and Prof. Jim Chelikowsky. I've taken four classes with Allan. His lecture is very enlightening, involved with lots of his deep thinking. The way he presented the physics world is so graceful and it really broadened my vision and helped me build my own blueprint of understanding of physics. Though I'm not a many-body physicist, I enjoyed every conversation with Allan and I did absorb something from him. Jim's name appeared in the textbook for so many times and initially I felt intimidated when talking to such a famous person. However, he is

really an easy-going person and I feel really lucky that I could have a chance to learn from him and use the code invented by him. I'm very thankful for his support and appearance at my APS talk. I'd also like to thank Jaime Souto Casares, the former postdoc working with Jim. He is really friendly, and helped me a lot with programming and debugging.

I'd also like to thank the whole community of our group. Agham Posadas is the research scientist in our group and he is so knowledgeable about experiment. I'd like to thank him for helping me clear so many doubts. Kurt Fredrickson, who was in his 5th year when I joined the group, gave me tremendous advices on how to use the code. Even after he graduated, he was still able to help me via emails and gave me lots of useful suggestions. Andrew O'Hara, same year as Kurt, helped me a lot when I started my research and performing real calculations. I don't have any overlap with Alex Slepko, Hosung Seo and Jaekwang Lee, but they are always responsive to my emails and try to answer my questions at their best. I had good collaboration with Kristy J Kormandy. Patrick Ponath gave me many good advices on graduation and job searching. For the current group members, I gained a lot from discussions with Ali Hamze and Donghan Shin. Wei Guo and Tobias Hadamek also taught me experimental knowledge. John Elliott Ortmann is very responsible. He made our collaboration much easier and the whole process was enjoyable. Jaqueline G. Kremer has been my officemate for three years. We got along very well with each other and her considerateness and kind-heartedness warmed me a lot. I gave my best wishes to all of all my group members on their future study and career.

Life would be a disaster without a company of my friends. Due to the word limitation, I could not thank everyone. Here I have several friends that I need to give special credits. Meng Li, Kai Hao and Fei Xue are members of our "basketball gang". We

chatted a lot, argued nonsense a lot, but truly gained happiness a lot. We shared sorrow together, but also overcame the difficulties and made progress together. I have known Bangguo Xiong and Kai Zhong over 10 years since our undergraduate. The friendship unites us tightly from Peking to UT, and I believe this will continue in the rest of our lives. Yicong Wang has been my roommate for 5 years. We took care of each other and helped each other throughout these 6 years. Without all these guys, I couldn't imagine what my life would be like.

At last, I want to thank my family. My parents are the people that I could dump everything completely. Every time when I was frustrated, discouraged, or met trouble, they'd like to listen to me patiently. Though our lives are so different, they still brought up the best solutions or advices from their view. I might make a lot of trouble to them, but they never talked about that and only showed their selfless care to me. When I was stuck somewhere, I made countless complaints to my best friend, also as my family and brother Rui Lu. He took them all, and gave excitement back to me. These spiritual inspiration helped me regain my courage, firm my belief, continue to carry on along the road, and finally be able to finish this journey.

Abstract

Oxygen Vacancy Roles in Transition Metal Oxides and Related Heterostructures

Lingyuan Gao, PhD

The University of Texas at Austin, 2018

Supervisor: Alexander A. Demkov

Transition metal oxides have exhibited many emergent phenomena. Recent advancements in growth techniques have made their applications in devices even more promising. During growth, an oxygen vacancy is one of the most abundant types of point defects. In this dissertation, I use density functional theory to investigate the oxygen vacancy role in transition metal oxides and related heterostructures. I show how oxygen vacancies influence the phonon spectrum of HfO₂ films. With *ab-initio* calculations, a spin-polarized two-dimensional electron gas is predicted at the interface of a ferromagnetic insulator EuO and oxygen-deficient SrTiO₃. Experimental results agree with the theoretical discovery and a positive linear magnetoresistance is observed for this two-dimension electron system. Based on the first principles calculation results, we use the conventional Boltzmann transport theory to show that Zeeman splitting caused by proximity magnetism from EuO is responsible for the behavior of this unusual magnetoresistance.

Table of Contents

List of Tables	xii
List of Figures	xiii
Chapter 1 Introduction	1
Chapter 2 Computational Methodology: Density Functional Theory	6
2.1 Background: From Many-Body Hamiltonian to Independent Electron Approximation	6
2.2 Hohenberg-Kohn Theorems and Kohn-Sham Equation	10
2.3 Exchange-Correlation Density Functional and Advanced Methods	14
2.4 Pseudopotential	18
2.5 Plane-Wave Basis	23
2.6 Real Space Density Functional Method	28
Chapter 3 Effect of oxygen vacancies and strain on the phonon spectrum of HfO ₂ thin films	38
3.1 Introduction	38
3.2 Computational and Experimental Method	40
3.3 Phonon Spectrum of Monoclinic Hafnia	41
3.4 Influence of Strain	45
3.5 The Role Of Oxygen Vacancies	51
3.6 Conclusion	58
Chapter 4 <i>Ab-initio</i> study of spin-polarized two-dimensional t_{2g} electron gas at EuO/ SrTiO _{3-δ} interface	60
4.1 Introduction	60
4.2 Computational Method	62

4.3 Electronic Structure and Discussion	65
4.4 The Effect of on-Site Coulomb Repulsion U	71
4.5 Conclusion	77
Chapter 5 Large Positive Linear Magnetoresistance in the two-dimensional t_{2g} electron gas at EuO/SrTiO _{3-δ} Interface	78
5.1 Experimental Result.....	79
5.1.1 Epitaxial Growth.....	79
5.1.2 Photoemission Measurement	81
5.1.3 Electrical Characterization.....	85
5.2 Introduction to Origins of Positive Linear Magnetoresistance	89
5.3 Properties of Confined Two-Dimensional Electron Gas in SrTiO ₃	91
5.4 Classical Conductivity for Two-Dimensional Electron Gas.....	94
5.5 Magnetoresistance in Spin-Polarized SrTiO ₃ Two-Dimensional Electron Gas	97
Chapter 6 the LaAlO ₃ /SrTiO ₃ Quantum Well	102
6.1 Computational Details	102
6.2 Bulk Density of States of SrTiO ₃ and LaAlO ₃	105
6.3 Band Offset and Orbital Analysis for SrTiO ₃ /LaAlO ₃ Supercell	107
6.4 EELS Modeling for SrTiO ₃ /LaAlO ₃ Supercell	112
6.5 Quantum Well States in SrTiO ₃ /LaAlO ₃ Supercell	118
References.....	122

List of Tables

Table 3.1. Structural parameters of monoclinic HfO ₂ . Th. = theoretical, Exp. = experimental.....	42
Table 3.2. Calculated Raman frequencies (in cm ⁻¹) for monoclinic HfO ₂ and available experimental data. Th. = theoretical, Exp. = experimental.....	44
Table 3.3. Calculated Raman frequencies of monoclinic hafnia (in cm ⁻¹) in four different cases: without strain, with 1% in-plane biaxial compressive and tensile strain applied to <i>a</i> and <i>c</i> axes, and strain applied on sample (sample strain). Calculation results are compared with eleven identified Raman peaks in experiment.	46
Table 3.4. Zone-centered frequencies (in cm ⁻¹) below 127 cm ⁻¹ for pure hafnia supercell case, O ₃ and O ₄ vacancy cases. The corresponding k-points in the primitive cell are also listed.	53
Table 3.6. Frequencies (in cm ⁻¹) of vacancy-related modes in O ₄ vacancy cell and corresponding inverse participation ratio (IPR) values. Modes with large IPR values are highlighted.	56

List of Figures

Figure 1.1 Complexity and multifunctionality of perovskites, an important class of transition metal oxides which attract lots of attention [1].	1
Figure 1.2 Three polymorphs of bulk HfO ₂ . Oxygen atoms are in red and Hf atoms are in olive. Arrows in (a) show displacements necessary to transform to the tetragonal phase [2].	2
Figure 1.3 Structure of perovskite ABO ₃ . A is the green ball, B is the blue ball in the center, while O is the red ball.	3
Figure 1.4 Illustration of antiferrodistortive rotation of SrTiO ₃ . At the same horizontal plane, the neighbouring octahedra are rotated in opposite direction around the in-plane axis.	4
Figure 2.1 Schematic representation of Kohn-Sham ansatz.	12
Figure 2.2 Schematic representation of the self-consistent loop for solution of Kohn-Sham equations [17].	14
Figure 2.3 Comparison between the all-electron WF and pseudo WF. We can see the pseudo WF is much smoother than all-electron WF in the near-core region but matches it pretty well outside that region.	19
Figure 2.4 An illustration of Monkhorst-Pack Scheme. For two-dimensional lattice, 16 k points can be reduced to 3 inequivalent k points [30,31].	26
Figure 2.5 Break-up of a submesh cell into six tetrahedra [33].	27
Figure 2.6 Illustration of the linearly-interpolated weight function $\omega_j(\mathbf{k})$ that is used in integration [33].	28

Figure 2.7 (a) A tetrakaidecahedron nanocrystal with the (001) and (111) facets, (b) A cuboid nanocrystal with (001) and (110) facets, (c) The relative potential of a tetrakaidecahedron nanocrystal across the $x + y = 0$ plane, (d) The relative potential of a cuboid nanocrystal across the $x + y = 0$ plane. In (a) and (b), surface atoms are highlighted yellow.....31

Figure 2.8 The relative electrostatic potential viewed across differently sliced planes: (a) to (f) are for the tetrakaidecahedron and (g) to (l) are for the cuboid. (a) The atomic view of a (001) facet, (b) the potential across the plane placed 4 Å above the (001) facet, (c) same 1 nm above the (001) facet, (d) the atomic view of the (111) facet, (e) the potential across the plane placed 4 Å above the (111) facet, (f) same 1 nm above the (111) facet, (g) The atomic view of a (001) facet, (h) the potential across the plane placed 4 Å above the (001) facet, (i) same 1 nm above the (001) facet, (j) The atomic view of a (110) facet, (k) the potential across the plane placed 4 Å above the (110) facet, (l) same 1 nm above the (110) facet. In (a) and (d), surface atoms are highlighted yellow.....35

Figure 2.9 The calculated ionization potentials for five cuboids of different sizes. A fitting line is also plotted to show the linear relationship between atom number $n^{-1/3}$ and ionization potential (IP). Intercept of the fitting line is noted as the bulk work function W37

Figure 3.1 (a) Calculated phonon dispersion of monoclinic hafnia. Blue, black and red lines represent no strain, 1% compressive and tensile strain applied to a and c axes case, respectively. (b) Phonon density of states for no strain case.....43

Figure 3.2 Relative atomic displacements of the lowest Raman mode. Arrows denote the direction of the movement at each atom and the length is proportional to displacement amplitude. Monoclinic angle is between a and c axes. Bonds are also plotted to show different coordinations of O atom. 3-folded O atoms are marked by red and 4-folded O atoms are marked by magenta.44

Figure 3.3 X-ray diffraction scan of sputtered hafnia on a platinum substrate, measured at a grazing incidence (1°). The scan demonstrates that polycrystalline monoclinic hafnia is formed after annealing47

Figure 3.4 Experimental Raman spectra of HfO₂. (a) Bottom: measured Raman spectra of 50 nm HfO₂ on Pt using 532 nm laser (blue) and top: Lorentzian fit (green – for each peak, black – sum over all Lorentzians). Spectra are vertically offset for clarity. The HfO₂ was heated to 600 °C, then cooled to room temperature, forming a polycrystalline monoclinic phase. (See Figure 3.3) (b) Low wavenumber range: measured HfO₂ (blue, same as in a) vs. control experiment without sample and without objective in the laser path (red) showing similar features below 120 cm⁻¹. (c) Control measurement of the low wavenumber Raman spectrum (same as red curve in (b), measured data in black solid line) compared with rotational Raman modes of N₂ (red dashed) and O₂ (blue dash-dot). The low wavenumber modes at 59, 83, and 107 cm⁻¹ are clearly observed in the Raman spectra of the thin HfO₂ sample (marked “ambient peaks” in (a)) and are of comparable intensity due to the weak Raman response of the HfO₂ and the enhanced Raman signal of the rotational modes, where N₂ and O₂ modes overlap.49

Figure 3.5 (a) The first Brillouin zone (FBZ) of the conventional monoclinic (MCL) lattice. Under this convention, $(0.5, 0, 0)$, $(0, 0.5, 0)$, $(0, 0, 0.5)$, $(0.5, 0.5, 0)$, $(0, 0.5, 0.5)$, $(0.5, 0, 0.5)$, $(0.5, 0.5, 0.5)$ are the Z, X, Y, A, C, D, E points in the figure. Black lines represent the FBZ of the primitive cell while the red lines denote the FBZ of the doubled supercell. The primitive cell and supercell reciprocal lattice vectors \mathbf{b}_i and \mathbf{b}_i' are also shown with black and red arrows, respectively, and $\mathbf{b}_i' = 2\mathbf{b}_i$. We can see the high symmetry points in the primitive FBZ can be translated back to the Gamma point by purple vectors, which is the combination of \mathbf{b}_i' . (b) The phonon spectrum folding along the direction from Γ to E.52

Figure 3.6 (a) Distribution of square of the inner product $f_{\alpha\beta}$ in O_3 vacancy cell. (b) Distribution of square of the inner product $f_{\alpha\beta}$ in O_4 vacancy cell. (c) g_{α} for vacancy-related modes in O_3 vacancy cell. (d) g_{α} for vacancy-related modes in O_4 vacancy cell.55

Figure 3.7 (a) Bar plot of the mode. The X axis represents atomic number in the cell and first 32 atoms are Hf atoms, while other 63 atoms are O atoms. Colors of different atoms are selected according to Figure 3.7(c). (b) Bar plot of the mode. Colors of different atoms are selected according to Figure 3.7(d). (c) The simulation cell containing an O3 vacancy. Red balls represent oxygen atoms and cyan balls represent Hf atoms. The O3 vacancy is created by removing the grey atom. Atoms that have significant displacements in 96.4 cm⁻¹ mode are highlighted with black. (d) The simulation cell containing an O4 vacancy. The O4 vacancy is created by removing the grey atom. Atoms that have significant displacements in 755.6 cm⁻¹ mode are highlighted.....58

Figure 4.1 High-angle annular dark-field scanning transmission electron microscopy [100] projection image of the EuO/STO interface.....64

Figure 4.2 The simulation cell of (EuO)₃/TiO₂-(SrO-TiO₂)₆/(EuO)₃ heterostructure. (a) Top view of two different types of interfaces: Eu on top of a hollow site in a TiO₂ plane (top-H) and on top of an oxygen in a TiO₂ plane (top-O); (b) 2 × 2 supercell with a single vacancy at the sub-interface SrO plane. Only half of the cell is presented due to mirror symmetry. The oxygen vacancy site is marked in black.64

Figure 4.3 Density of states (DOS) projected on a specific atom for each layer in top-H heterostructure without and with a vacancy. Only the results for the upper half cell are shown due to symmetry. Eu, O, Ti, Sr states are marked by magenta, red, dark blue and green, respectively. EuO surface states are indicated with the square. (a) and (c) panels correspond to the spin-up while (b) and (d) correspond to spin-down components, respectively.	67
Figure 4.4 DOS projected on the Ti <i>d</i> states in each layer. Layer 1 represents the central “bulk” part of SrTiO ₃ , while layer 4 represents the interfacial layer. (a) DOS of top-H heterostructure with a vacancy; (b) DOS of top-H heterostructure without vacancies but artificially doped with two extra electrons.	70
Figure 4.5 Similar to Figure 4.2, the atom-projected DOS for each layer in heterostructure containing a vacancy with $U_{\text{Ti-d}} = 8$ eV.	73
Figure 4.6 (a) The e_g - t_{2g} splitting in bulk SrTiO ₃ for $U_{\text{Ti-d}} = 5$ eV and (b) $U_{\text{Ti-d}} = 8$ eV. ...	76
Figure 5.1 (a) Schematic plot of the EuO/SrTiO ₃ heterointerface. (b) Reciprocal space map of the STO (002) and EuO (113) peaks for 7 nm EuO on STO. The EuO rocksalt unit cell is rotated 45° with respect to the surface unit cell of the perovskite.	79
Figure 5.2 (a) X-ray diffraction coupled scans with corresponding (b) in-plane reciprocal space map and positions in reciprocal space for (c) STO and (b) EuO with a 45° rotation of the surface unit cell.	80

Figure 5.3 (a) High-angle annular-dark-field scanning transmission electron microscopy [100]-projection image of the EuO/STO interface. (b) Corresponding false color map shows a distribution map from the Ti L-edge fit (SrTiO ₃ , red; SrTiO _{3-δ} , green). (c) Ti-L coefficient as a function of position shows a sharp peak at the interface.....	81
Figure 5.4 Resonant soft-X-ray ARPES of 2-nm EuO/STO heterointerface through the Ti <i>L</i> -edge. (a) XAS spectrum. (b) Resonant photoemission from the valence band as a function of excitation energy. Intensity the near- <i>E_F</i> region is scaled up by ~30. (c) Resonant intensity for constant <i>E_B</i> in the valence band, Eu level and 2DEG. The valence band and 2DEG signals follow the Ti <i>L</i> -edge XAS spectrum that confirms their Ti-derived character. (d,e) SX-ARPES images at <i>hν</i> = 460.3 and 466 eV enhancing the <i>d_{xy}</i> - and <i>d_{yz}</i> -derived states, respectively. The intensity waterfalls are reveal polaronic nature of the interface charge carriers. (f) Fermi surface of the interface states measured at <i>hν</i> = 466 eV.	83
Figure 5.5 (a) Resonance photoemission spectra of valence band near Eu 3d threshold. Strong resonance of the Eu ²⁺ states in the valence band at <i>hν</i> = 1128 eV and Eu ³⁺ states at <i>hν</i> = 1130 eV. No resonating states at the <i>E_F</i> . (b) Valence band spectrum at <i>hν</i> = 457 eV shows the prevalence of Eu ²⁺ ...	84
Figure 5.6 (a) Sheet resistance for a 7-nm EuO film as a function of temperature. (b) Hall resistance <i>R_{XY}</i> for a 7-nm EuO film at 120 K. Solid lines indicate linear fits.	86

Figure 5.7 (a) Magnetoresistance (MR) data measured in a perpendicular magnetic field at 20 K, 100 K, and 300 K. Solid lines indicate fits to the data. The MR increases linearly with the magnetic field at 20 K, quadratically at 100 K, and is field-independent at room temperature. (b) Linear c_1 and quadratic c_2 MR fit coefficients for the same film as a function of temperature. (c) Field-cooled magnetization M of a similar 7-nm EuO film as a function of temperature at constant in-plane magnetic field of 0.01 T. Inset: corresponding magnetization loop measured at 10 K.	88
Figure 5.8 Schematic plot of the two dimensional t_{2g} electron gas in SrTiO ₃	98
Figure 6.1. A (LAO) _{4.5} /(STO) _{5.5} simulation cell with two symmetric n-type interfaces.	104
Figure 6.2. Total DOS of bulk STO projected onto TiO ₂ and SrO layers. Zero of energy is set at the top of the valence band.	105
Figure 6.3. (a) PDOS for Sr, Ti and O atoms individually. (b) Magnified PDOS of O atoms (10 ×).	106
Figure 6.4. (a) Total DOS of bulk LAO projected onto AlO ₂ and LaO layers Zero of energy is set at the top of the valence band. (b) PDOS of bulk La, Al and O atoms individually.	106
Figure 6.5 (a). Total DOS of the LAO/STO QW, layer by layer. (b) Total DOS of QW, layer by layer without La f components. DOS on 3 LaO layers are magnified by 5 times to show evanescent states, which is highlighted by square box.	109
Figure 6.6. p -PDOS of QW, layer by layer and experimental EELS O K edge.	110
Figure 6.7. Ti- d PDOS of QW, layer by layer.	111

Figure 6.8. (a) 3D charge density of electron gas. (b) 2D yz plane of the electron gas (c) Same as Figure 8(b). Color bar range is from [0, 10%]. (d) PDOS of evanescent states highlighted by square box in Figure 6.8(c).	112
Figure 6.9. Computed O K edge spectrum in bulk SrTiO ₃ as a function of the simulation cell size.....	113
Figure 6.10. Computed Ti L ₂ / L ₃ edge in bulk SrTiO ₃	114
Figure 6.11. Computed oxygen K edge spectrum in bulk LaAlO ₃ as a function of the simulatino cell size (2.0 eV broadedning is applied). Experimental data is shown in the top panel for comparison.	115
Figure 6.12. Computed L ₂ / L ₃ edge in the QW structure.....	116
Figure 6.13. (a) O K edge for the LAO/STO QW heterostructure (broadening of 2.0 eV is applied). Thick soild lines are calcaulted and thin lines are experiment. (b) p-PDOS for the LAO/STO QW heterostructure layer by layer.....	117
Figure 6.14. Density functional theory calculations of quantum well states. (a) The calculated density of states (DOS) displaying the sum of $d_{xz/yz}$ states for three-, four-, and five-u.c. QW structures. The red, green, and blue arrows indicate the transition energy between the ground state and first- excited state in five-, four-, and three-u.c. QWs, respectively. (b) Charge distribution in real space corresponding to the five QW subbands in an (LAO) _{7.5} /(STO) _{4.5} cell. The energy of each state is labeled below the figure. Each plot is accompanied with its schematic wave function on the right. The width of each state is 0.2 eV. La, Al, Sr, Ti, and O atoms are colored as dark blue, magenta, green, light blue and red, respectively.	120

Figure 6.15. The calculated density of states (DOS) displaying the sum of $d_{xz/yz}$ states for stoichiometric (asymmetric) QW structures. (a) Pure $(\text{LAO})_7/(\text{STO})_4$ cell. (b) La doped $(\text{LAO})_7/(\text{STO})_4$ cell. Each QW state peak is denoted by the black arrow.....121

Chapter 1 Introduction

Transition metal oxides (TMO) exhibit many intriguing phenomena: from being insulating, semiconducting and even metallic, to showing ferroelectricity, ferromagnetism, superconductivity and colossal magnetoresistance (Figure 1.1). Different electronic phases are inherently related to internal degrees of freedom of TMO, which include orbital, charge, spin and lattice degree of freedom. With delicate designing and controlling, one has a great opportunity to exploit novel functionalities out of these materials.

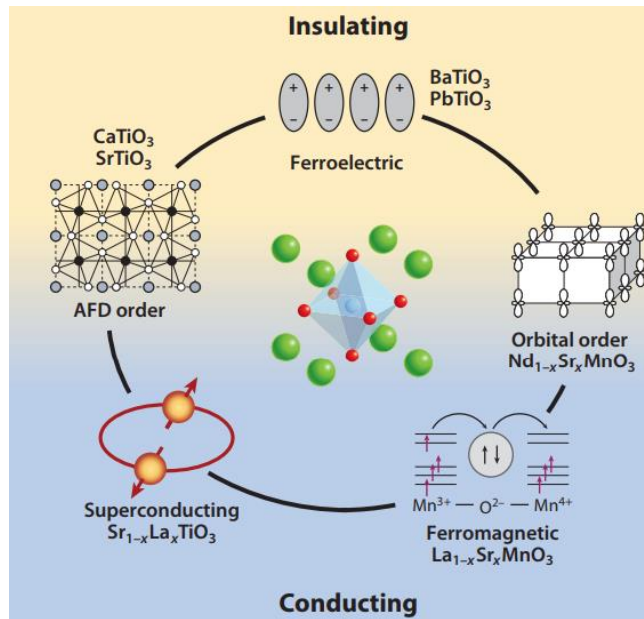


Figure 1.1 Complexity and multifunctionality of perovskites, an important class of transition metal oxides which attract lots of attention [1].

In this dissertation, we will primarily focus on two types of transition metal oxides. The first one is HfO₂, which is very important in technological applications. HfO₂ is a hard material with high bulk modulus, high melting point and high chemical stability. Because of its high static dielectric permittivity, it has replaced SiO₂ as a gate dielectric

in the metal-oxide-semiconductor field-effect transistor (MOSFET). At atmospheric pressure, bulk hafnia has three polymorphs: At low temperature, it is monoclinic with a space group $P2_1/c$, and transforms to a tetragonal structure with a space group $P4_2/nmc$ at 1720°C, and finally transforms to a cubic structure with a space group $Fm3m$ at 2600°C. The three phases are illustrated in Figure 1.2.

The second oxide we are going to talk about is SrTiO_3 . SrTiO_3 has a perovskite structure with a chemical formula ABO_3 . In the primitive cubic cell, A atom is at the cube corner, B atom is at the cube center, while three O atoms are at the center of three faces. Thus a corner-shared octahedron BO_6 can be formed. In general, both A and B are cations and X are anions. Illustration of the perovskite structure is presented in Figure 1.3 as below.

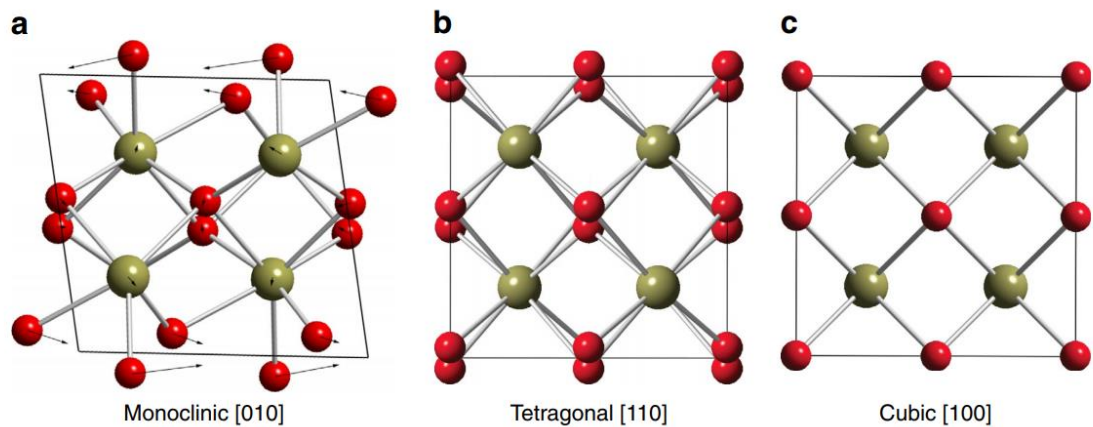


Figure 1.2 Three polymorphs of bulk HfO_2 . Oxygen atoms are in red and Hf atoms are in olive. Arrows in (a) show displacements necessary to transform to the tetragonal phase [2].

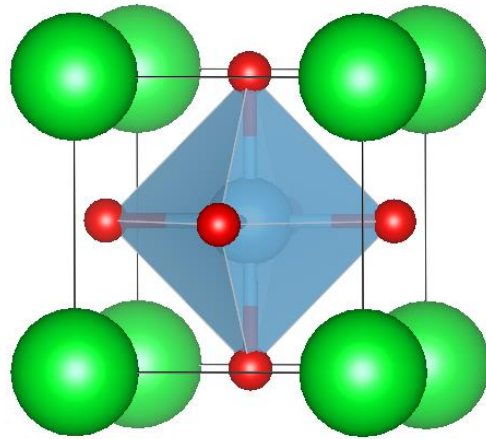


Figure 1.3 Structure of perovskite ABO_3 . A is the green ball, B is the blue ball in the center, while O is the red ball.

$SrTiO_3$ also undergoes several structural phase transitions with the change of temperature. At room temperature it has a cubic structure with space group $Pm\bar{3}m$. When temperature is at 105 K, it transforms from the cubic to tetragonal structure with an antiferrodistortive rotation (Figure 1.4): The neighbouring TiO_6 octahedra will rotate in opposite direction and changes the c/a ratio accordingly [3–5]. In addition, $SrTiO_3$ also exhibits quantum paraelectricity: The dielectric constant ϵ can increase from 300 at room temperature to 30000 at about 4 K [6].

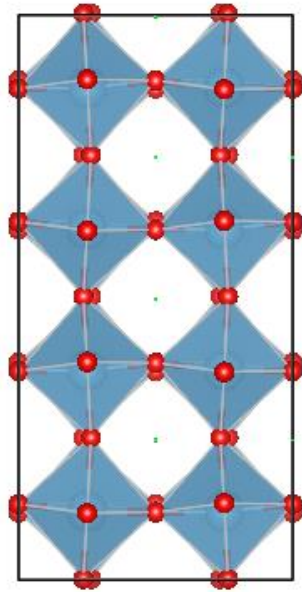


Figure 1.4 Illustration of antiferrodistortive rotation of SrTiO_3 . At the same horizontal plane, the neighbouring octahedra are rotated in opposite direction around the in-plane axis.

If we bring two complex oxides together, emergent phenomena would occur at interface. When two oxides have different chemical potentials, charge transfer could take place between them. This could create a quasi-two-dimensional electron gas at the interfaces. The 2D system has attracted much attention as it exhibits many new effects, which are not observed in bulk constituent oxides. Among them, the most prominent are ferromagnetism and superconductivity. Recently, many experiments have shown that 2D system occurring in the SrTiO_3 -based heterostructures can host both ferromagnetic and superconducting orders, which makes SrTiO_3 -based heterostructures even more remarkable [7].

Much progress in the thin film growth techniques has been made recently [8]. To grow SrTiO_3 and related heterostructures, atomic layer deposition (ALD), pulsed laser

deposition (PLD). Molecular beam epitaxy (MBE), laser MBE and sputtering method are often used. However, during the growth process, many defects can be introduced into the system, which would affect the structural and electronic properties significantly. For example, by annealing SrTiO₃ under low pressure, oxygen vacancies are easily created. Also, as-grown films are almost always nonstoichiometric, though this can be corrected by high-temperature annealing. In HfO₂, oxygen vacancies may affect leakage current through the oxide, and charge vacancies can contribute to dielectric loss [9]. In SrTiO₃, oxygen vacancies are the most abundant types of point defects. They could induce structural distortions, free or localize carriers and hence can influence conductivity, and also change the optical properties dramatically. Therefore, investigating oxygen vacancies effect in transition metal oxide and related heterostructures is of fundamental importance.

The dissertation is a summary of theoretical work. However, for most of the studies we are working together with experimental collaborators. To make the story complete, experimental results are also presented. The rest of the dissertation is organized as follows. In Chapter 2, the computational method based on density functional theory is introduced. In Chapter 3, we discuss the effect of strain and oxygen vacancies on the phonon spectrum of HfO₂ films. In Chapter 4, we present the ab-initio study of spin-polarized two-dimensional electron gas at the interface of EuO and oxygen-deficient SrTiO₃. In Chapter 5, based on calculation results from Chapter 4, we propose a theoretical explanation for the experimentally observed positive linear magnetoresistance of two-dimensional electron gas in the EuO/SrTiO_{3-δ} systems.

Chapter 2 Computational Methodology: Density Functional Theory

In this chapter, we review density functional theory (DFT), which is the main computational methodology we use throughout this dissertation. The chapter is organized as follows: In 2.1, we introduce the fundamental many-body problem to be solved and an independent-electron-approximation treatment at early stage. In 2.2, we discuss the foundation of DFT Hohenberg-Kohn theorem and the auxiliary Kohn-Sham equations. In 2.3, we list different forms of density functional that are related with exchange-correlation term in the equations. Also, the LDA+U and hybrid functional methods are discussed in this chapter. In 2.4, we talk about the pseudopotential method, which can simplify the calculation. In 2.5, we introduce a widely used plane-wave basis in DFT and the related parameters. In 2.6, we introduce another real-space DFT method, which can solve the Kohn-Sham equations in real space and we give one example of using this method to calculate the work function of metallic nanocrystals.

2.1 BACKGROUND: FROM MANY-BODY HAMILTONIAN TO INDEPENDENT ELECTRON APPROXIMATION

The starting point of a theory describing a solid-state system is the interacting many-body Hamiltonian, which involves both electrons and nuclei,

$$\begin{aligned}
 H &= T_I + V_{I-I} + T_e + V_{e-e} + V_{I-e} \\
 &= - \sum_I \frac{\hbar^2}{2M_I} \nabla_I^2 + \frac{1}{2} \sum_{I \neq J} \frac{Z_I Z_J e^2}{|R_I - R_J|} - \sum_i \frac{\hbar^2}{2m_e} \nabla_i^2 + \frac{1}{2} \sum_{i \neq j} \frac{e^2}{|r_i - r_j|} \\
 &\quad - \sum_{I,i} \frac{Z_I e^2}{|R_I - r_i|}, \tag{2.1}
 \end{aligned}$$

where T_I , V_{I-I} , T_e , V_{e-e} , V_{I-e} represent the kinetic energy of the nuclei, nucleus-nucleus interaction, kinetic energy of electrons, electron-electron interaction, and the electron-nucleus interaction, respectively. \hbar , M_I , Z_I , R_I , m_e , r_i represent the Planck

constant, ion mass, ion charge, ion position, electron mass and electron position, respectively. This is a complicated problem and to reduce the complexity, the first good approximation is the Born-Oppenheimer or adiabatic approximation [10]. As ions move much slower compared to electrons due to their large mass, the core of this approximation is to separate the total wave functions (WFs) into a product of the WF of electrons and the WF of ions:

$$\Psi(r, R) = \psi(r) \psi(R), \quad (2.2)$$

where $\psi(r)$ is the electronic WF, and $\psi(R)$ is the ionic WF. In this way, T_I and V_{I-I} can be separated from the total Hamiltonian and for the electrons, we only use:

$$H = T_e + V_{e-e} + V_{I-e} = - \sum_i \frac{\hbar^2}{2m_e} \nabla_i^2 + \frac{1}{2} \sum_{i \neq j} \frac{e^2}{|r_i - r_j|} - \sum_{I,i} \frac{Z_I e^2}{|R_I - r_i|} \quad (2.3)$$

Looking at the current Hamiltonian, we realize the only hard term to deal with is the two-body interaction term, as it includes terms describing the interaction of two electrons. To solve this problem, historically, the simplified approach is to replace the interacting Hamiltonian with a non-interacting Hamiltonian, which can incorporate the two-body interactions into an effective potential on one electron.

There are two independent-electron approaches: the first is called the ‘‘Hartree-like’’ approximation [11], and the second is called the ‘‘Hartree-Fock’’ approximation. For the ‘‘Hartree-like’’ approximation [12], the total WF is written down as the product of WF of the individual electrons. Then the energy and WF of each electron can be found from a Schrodinger-like equation:

$$\left[- \sum_i \frac{\hbar^2}{2m_e} \nabla_i^2 + V_{eff}^\sigma(\mathbf{r}) \right] \psi_i(\mathbf{r}) = \varepsilon_i^\sigma \psi_i(\mathbf{r}) \quad (2.4)$$

This is the heart of the independent-electron approximation, as it includes the Coulomb interaction as an effective potential and reduces the many-electron problem to a

one-electron problem. After solving WF for each electron in the system, the total WF can be constructed from the product of all these one electron states.

For the ‘‘Hartree-Fock’’ approximation, the starting point is to establish an antisymmetrized determinant WF with N orbitals for each electron, and then use it to compute the expectation value of the Hamiltonian in 2.3. The WF has a form of Slater determinant:

$$\Phi = \frac{1}{(N!)^{1/2}} \begin{vmatrix} \phi_1(\mathbf{r}_1, \sigma_1) & \phi_1(\mathbf{r}_2, \sigma_2) & \phi_1(\mathbf{r}_3, \sigma_3) & \dots \\ \phi_2(\mathbf{r}_1, \sigma_1) & \phi_2(\mathbf{r}_2, \sigma_2) & \phi_2(\mathbf{r}_3, \sigma_3) & \dots \\ \phi_3(\mathbf{r}_1, \sigma_1) & \phi_3(\mathbf{r}_2, \sigma_2) & \phi_3(\mathbf{r}_3, \sigma_3) & \dots \\ \vdots & \vdots & \vdots & \vdots \end{vmatrix}, \quad (2.5)$$

where $\phi_1(\mathbf{r}_i, \sigma_i)$ is a product of WF space part $\psi_i(\mathbf{r}_i)$ and spin part $\alpha_i(\sigma_i)$. Also, $\psi_i(\mathbf{r}_i)$ is orthogonal with each other. With this antisymmetric WF, we can compute the expectation value of the Hamiltonian of (2.3), which is the total energy of the system. In the atomic units, the expectation value is:

$$\begin{aligned} \langle \Phi | H | \Phi \rangle &= \sum_{i, \sigma} \int d\mathbf{r} \psi_i^{\sigma*}(\mathbf{r}) \left[-\frac{1}{2} \nabla^2 + V_{ext}(\mathbf{r}) \right] \psi_i^{\sigma}(\mathbf{r}) \\ &+ \frac{1}{2} \sum_{i, j, \sigma_i, \sigma_j} \int d\mathbf{r}' d\mathbf{r} \psi_i^{\sigma_i*}(\mathbf{r}) \psi_j^{\sigma_j*}(\mathbf{r}') \frac{1}{|\mathbf{r} - \mathbf{r}'|} \psi_i^{\sigma_i}(\mathbf{r}) \psi_j^{\sigma_j}(\mathbf{r}') \\ &- \frac{1}{2} \sum_{i, j, \sigma} \int d\mathbf{r}' d\mathbf{r} \psi_i^{\sigma*}(\mathbf{r}) \psi_j^{\sigma*}(\mathbf{r}') \frac{1}{|\mathbf{r} - \mathbf{r}'|} \psi_j^{\sigma}(\mathbf{r}) \psi_i^{\sigma}(\mathbf{r}') \end{aligned} \quad (2.6)$$

The first term includes all single-particle term and $V_{ext}(\mathbf{r})$ is the V_{I-e} term of (2.3). The second term is the classical Coulomb repulsion so it represents ‘‘direct interaction’’ between two electrons. Energy of this term is also called the Hartree energy. For the third term, at the same position, orbitals at bra vectors and ket vectors are different. So we call this term the ‘‘exchange interaction’’. To minimize the total energy, the Lagrange multipliers method is used and a Schrodinger-like equation for each $\psi_i(\mathbf{r})$ is:

$$\left[-\sum_i \frac{\hbar^2}{2m_e} \nabla^2 + \sum_{j,\sigma_j} \int d\mathbf{r}' \psi_i^{\sigma_j*}(\mathbf{r}') \psi_j^{\sigma_j*}(\mathbf{r}') \frac{1}{|\mathbf{r}-\mathbf{r}'|} \right] \psi_i^\sigma(\mathbf{r}) - \frac{1}{2} \sum_j \int d\mathbf{r}' \psi_j^{\sigma*}(\mathbf{r}') \psi_i^{\sigma*}(\mathbf{r}') \frac{1}{|\mathbf{r}-\mathbf{r}'|} \psi_j^\sigma(\mathbf{r}) = \varepsilon_i^\sigma \psi_i^\sigma(\mathbf{r}) \quad (2.7)$$

This is called the Hartree-Fock equation. We note the unphysical interaction between $\psi_i(\mathbf{r}_i)$ and $\psi_i(\mathbf{r}_i)$ in the “direct interaction” is cancelled in the “exchange interaction”, so we don’t need to require $i \neq j$ in the sum. This unphysical interaction is called the “self-interaction”, and we will talk about its importance later. We want to emphasize the Hartree-Fock approximation only considers the correlation originating from the Pauli principle: The Orthogonality of basis orbitals $\psi_i(\mathbf{r}_i)$ is based upon the exclusion principle that electrons are automatically kept away when they have the same spin. However, in reality the single determinant is not enough. The fact that two electrons with the same orbital but opposite spins can’t be at the same place due to Coulomb repulsion is not considered. This in general, is called the “correlation effect”, which is different from the “exchange effect” originating from the exchange term.

The simplest model system that can be solved by the independent-electron approach is the homogenous electron gas (HEG), where the ions are replaced by a uniform positively charged background. Thomas and Fermi solved this model under the non-interacting approximation, namely, only the kinetic energy term is considered [13,14]. The eigenvector is the normalized plane wave $\psi_{\mathbf{k}}(\mathbf{r}) = \frac{1}{V^{1/2}} e^{i\mathbf{k}\cdot\mathbf{r}}$, and the total ground state is a Slater determinant constructed with plane waves, and the wave vectors of these plane waves are all inside the Fermi sphere. Using the total electron number conservation, we can get the Fermi wave vector:

$$\frac{4\pi}{3} (k_F^\sigma)^3 = \frac{(2\pi)^3}{V} N^\sigma, \quad k_F^\sigma = (3\pi^2)^{\frac{1}{3}} n^{\frac{1}{3}} (n^\uparrow = n^\downarrow) \quad (2.8)$$

The total kinetic energy per electron for unpolarized case is:

$$T_0^\sigma = \frac{3}{5} E_{F0}^\sigma, \quad E_{F0}^\sigma = \frac{1}{2} (k_F^\sigma)^2 \quad (2.9)$$

Dirac solved the model analytically under the Hartree-Fock approximation [15].

Now the eigenenergy of the HEG model also contains the exchange energy term:

$$\varepsilon_k = \frac{1}{2} k^2 + \frac{k_F}{\pi} f(x), f(x) = - \left(1 + \frac{1-x^2}{2x} \ln \left| \frac{1+x}{1-x} \right| \right), x = \frac{k}{k_F} \quad (2.10)$$

It is seen clearly that for both approximations, the total energy is related, and can even be expressed with the electron density. This suggests the idea to formulate the total energy as:

$$E_{TF}(n) = C_1 \int d^3r n(\mathbf{r})^{5/3} + C_2 \int d^3r n(\mathbf{r})^{4/3} + \int d^3r V_{ext}(\mathbf{r}) n(\mathbf{r}) + \int d^3r d^3r' \frac{n(\mathbf{r}) n(\mathbf{r}')}{|\mathbf{r} - \mathbf{r}'|}, \quad (2.11)$$

where the first term is the kinetic energy with $C_1 = \frac{3}{10} (3\pi^2)^{2/3}$, the second term is the exchange energy with $C_2 = -\frac{3}{4} \left(\frac{3}{\pi}\right)^{1/3}$ (for non-spin-polarized case), the third term is the electron-ion interaction and the fourth term is the classical electrostatic Hartree energy. Though the Thomas-Fermi-Dirac approximation is crude, it is the original form of density functional theory, which expresses the total energy as the density functional.

2.2 HOHENBERG-KOHN THEOREMS AND KOHN-SHAM EQUATION

There are two parts to the Hohenberg-Kohn theory [16]:

Theorem I: For any system of interacting particles in an external potential $V_{ext}(\mathbf{r})$, the potential $V_{ext}(\mathbf{r})$ is determined uniquely, except for a constant, by the ground state particle density $n_0(\mathbf{r})$.

Theorem II: A universal functional for the energy $E[n]$ in terms of the density $n(\mathbf{r})$ can be defined, valid for any external potential $V_{ext}(\mathbf{r})$. For any particle $V_{ext}(\mathbf{r})$, the exact ground state energy of the system is the global minimum value of this

functional, and the ground density $n(\mathbf{r})$ that minimizes the functional is the exact ground state density $n_0(\mathbf{r})$.

We refer the reader to see the proof in [16]. Theorem I tells that the ground state density uniquely determines the external potential (except for a constant). Corresponding corollary follows that as the Hamiltonian is uniquely determined, the many-body WFs are also determined. Therefore, all properties of the system are determined only by the ground state electron density $n(\mathbf{r})$. For Theorem II, it follows that if the functional $F_{HK}[n] = T[n] + E_{INT}[n]$ was known, then by minimizing the total energy functional $E_{HK}[n]$ as the sum of $\int d^3r V_{ext}(\mathbf{r})n(\mathbf{r})$ and $F_{HK}[n]$ respect to $n(\mathbf{r})$, one would find the exact ground state density and energy.

The Hohenberg-Kohn theorem states that the Hamiltonian can be fully determined by the ground state density $n_0(\mathbf{r})$. However, many-body WFs of the interacting many-body system are hard to calculate, which means $n_0(\mathbf{r})$ is also difficult to obtain. In 1965, Kohn and Sham introduced an ansatz to replace the interacting many-body problem with a different auxiliary independent-particle problem. The Kohn-Sham ansatz has two assumptions:

1. The exact ground state density can be represented by the ground state of an auxiliary system of non-interacting particles. This is called “non-interacting-V-representability”.
2. The auxiliary Hamiltonian is chosen to have the usual kinetic operator and an effective local potential $V_{eff}^\sigma(\mathbf{r})$ acting on an electron of spin σ at point \mathbf{r} .

The schematic representation of Kohn-Sham ansatz is shown in Figure 2.1: by equating the ground state density of the original interacting system with that of some chosen non-interacting system, we convert the many-body interacting problem to the non-interacting problem. The auxiliary Hamiltonian has the form like:

$$H_{aux}^\sigma = -\frac{1}{2}\nabla^2 + V^\sigma(\mathbf{r}) \quad (2.12)$$

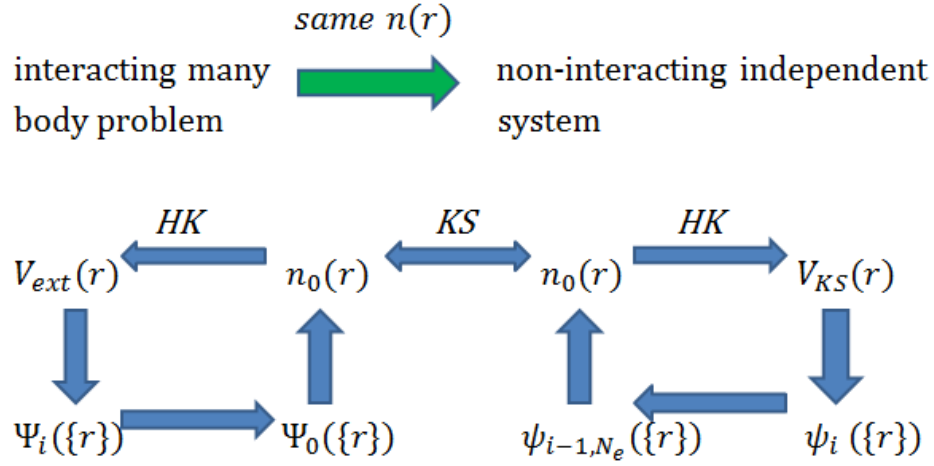


Figure 2.1 Schematic representation of Kohn-Sham ansatz.

For a system of N independent electrons, the ground state has one electron in each of the N^σ orbitals $\psi_i^\sigma(\mathbf{r})$ with the lowest eigenvalues ε_i^σ of Hamiltonian (2.12). The density of the auxiliary system is given by the sums of squares of the orbitals for each spin:

$$n(\mathbf{r}) = \sum_\sigma n(\mathbf{r}, \sigma) = \sum_\sigma \sum_{i=1}^{N^\sigma} |\psi_i^\sigma(\mathbf{r})|^2 \quad (2.13)$$

The independent-electron kinetic energy T_s is:

$$T_s = -\frac{1}{2} \sum_\sigma \sum_{i=1}^{N^\sigma} \langle \psi_i^\sigma | \nabla^2 | \psi_i^\sigma \rangle = \frac{1}{2} \sum_\sigma \sum_{i=1}^{N^\sigma} \int d^3r |\nabla \psi_i^\sigma(\mathbf{r})|^2 \quad (2.14)$$

Similar to the Thomas-Fermi-Dirac approximation, the classical electrostatic Hartree energy is:

$$E_{Hartree}[n] = \frac{1}{2} \int d^3r d^3r' \frac{n(\mathbf{r})n(\mathbf{r}')}{|\mathbf{r} - \mathbf{r}'|} \quad (2.15)$$

The Kohn-Sham approach rewrites the total energy functional of the many-body into single-electron form:

$$E_{KS}[n] = T_s[n] + E_{Hartree}[n] + \int d^3r V_{ext}(\mathbf{r})n(\mathbf{r}) + E_{xc}[n], \quad (2.16)$$

where

$$E_{xc}[n] = \langle T \rangle - T_s[n] + \langle V_{int} \rangle - E_{Hartree}[n] \quad (2.17)$$

Here $E_{xc}[n]$ is called the exchange-correlation functional. All unknown many-body terms are incorporated into this term. Therefore, to improve the accuracy of the density functional theory, we need to make the approximation of the exchange-correlation functional as good as possible. This will be discussed in the next sub-chapter.

We use the variational method to deal with the Kohn-Sham total energy functional $E_{KS}[n]$. By varying the WF $\psi_i^\sigma(\mathbf{r})$ and using the Lagrange multiplier method, we get the well-known Kohn-Sham equations as a set of equations for all N electrons in the system:

$$\left(-\frac{1}{2}\nabla^2 + V_{ext}(\mathbf{r}) + V_{Hartree}(\mathbf{r}) + V_{xc}^\sigma(\mathbf{r}) \right) \psi_i^\sigma(\mathbf{r}) = \varepsilon_i^\sigma \psi_i^\sigma(\mathbf{r}) \quad (2.18)$$

The equations have the form of independent-particle equations with a potential that must be found self-consistently with the resulting density. Steps of solving these equations are shown as a flow in the Figure 2.2 below [17]. Initially, we give a n^{in} as the input density. We use the density n^{in} to construct the effective potential, solve Kohn-Sham equations and get the output density n^{out} . If the output density n^{out} doesn't agree with n^{in} , we use a mixture of n^{in} and n^{out} to solve the Kohn-Sham equations until the final output is equal to the input density. If the exact form of $E_{xc}[n]$ is known, they would give the exact ground state information.

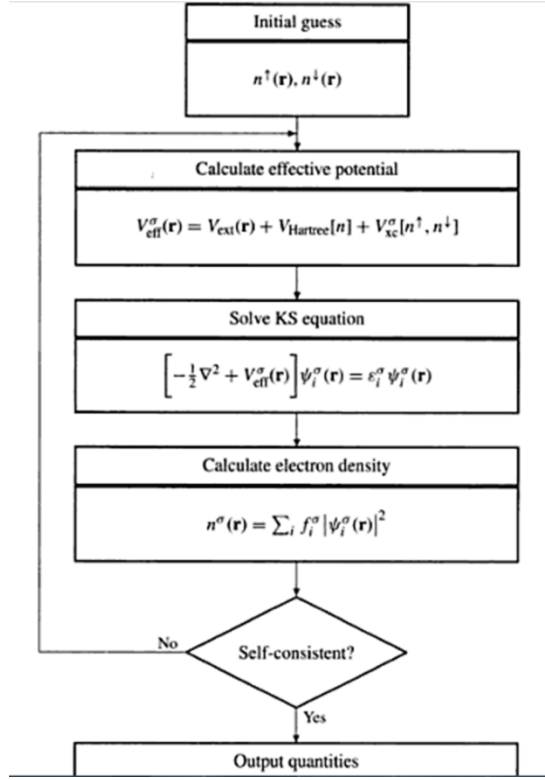


Figure 2.2 Schematic representation of the self-consistent loop for solution of Kohn-Sham equations [17].

2.3 EXCHANGE-CORRELATION DENSITY FUNCTIONAL AND ADVANCED METHODS

As discussed by Kohn and Sham, solids can be compared with the HEG, in which the effects of exchange and correlation are local in nature. Therefore, they propose making the local density approximation (LDA), where the exchange-correlation energy is an integral over all space with the exchange-correlation energy density taken as that of the HEG at each point:

$$\begin{aligned}
 E_{xc}^{LSDA}[n^\uparrow, n^\downarrow] &= \int d^3r n(\mathbf{r}) \epsilon_{xc}^{hom}(n^\uparrow(\mathbf{r}), n^\downarrow(\mathbf{r})) \\
 &= \int d^3r n(\mathbf{r}) [\epsilon_x^{hom}(n^\uparrow(\mathbf{r}), n^\downarrow(\mathbf{r})) + \epsilon_c^{hom}(n^\uparrow(\mathbf{r}), n^\downarrow(\mathbf{r}))] \quad (2.19)
 \end{aligned}$$

The exchange energy of the HEG is the second term in equation (2.10), and the correlation energy can be calculated with the Quantum Monte Carlo (QMC) methods [18]. The most widely used form for the exchange-correlation functional is that formulated by Perdew and Zunger [19], and has parameterized analytic forms for $E_c^{LSDA}[n^\uparrow, n^\downarrow]$ based on the QMC results. The initial thought of treating a solid as the HEG sounds not that rational. However, the calculation results agree with the experimental results very well. This demonstrates that for most solids, effects of exchange and correlation are in the short range, which is similar to the HEG.

The most notorious flaw of the LDA is the spurious self-interaction term. As we have discussed in the context of the Hartree-Fock method, the unphysical interaction between $\psi_i(\mathbf{r}_i)$ and $\psi_i(\mathbf{r}_i)$ in the “direct interaction” is cancelled in the “exchange interaction”. However, in LDA, it is only partially cancelled. Nevertheless, LDA still works very well for most of the solid systems, as the self-interaction vanishes quickly for delocalized orbitals or over extended systems. On the other hand, the Hartree-Fock method is more important for inner shell orbitals and atoms, as the exchange energy is more important there. For low density valence electrons, the correlation energy is as important as the exchange energy.

Though LDA is very successful, the functional can be further improved by considering the gradient of the density $\nabla n(\mathbf{r})$ along with the density $n(\mathbf{r})$ at each point. This would input more local density information into the functional. However, the gradients in solids are very large and the expansion breaks down. Therefore, different ways are proposed to modify the behavior of the functional for large gradients. The method is called the generalized-gradient expansion (GGA). The generalized form is

$$\begin{aligned}
E_{xc}^{GGA}[n^\uparrow, n^\downarrow] &= \int d^3r n(\mathbf{r}) \epsilon_{xc}(n^\uparrow(\mathbf{r}), n^\downarrow(\mathbf{r}), |\nabla n^\uparrow(\mathbf{r})|, |\nabla n^\downarrow(\mathbf{r})|) \\
&= \int d^3r n(\mathbf{r}) \epsilon_x^{hom}(n) F_{xc}(n^\uparrow(\mathbf{r}), n^\downarrow(\mathbf{r}), |\nabla n^\uparrow(\mathbf{r})|, |\nabla n^\downarrow(\mathbf{r})|) , \tag{2.20}
\end{aligned}$$

where $\epsilon_x^{hom}(n)$ is the exchange energy of the HEG and F_{xc} is a dimensionless function. There are three different forms of F_{xc} that are most widely used: Becke(B898) [20], Perdew and Wang (PW91) [21], and Perdew, Burke and Ernzerhof [22], which use different numerical forms of F_x . The GGA usually leads to the exchange energy being lower than that of the LDA and this leads to greater lowering of the exchange energy in atoms than in molecules and solids. Therefore, GGA will reduce the binding energy, and correct the LDA overbinding problem. On the other hand, the behavior of the functional depends on a specific physical condition: One form of F_x working well for some properties or some systems doesn't guarantee that it will work for others.

Though LDA or GGA are successful for many solid state systems, they are not applicable to all situations. One deficiency is their inability to describe the strong correlated systems, such as the transition element or a rare-earth element, with partially filled d or f orbitals. With the orbital-independent LDA or GGA methods, the rare-earth or transition metal oxides are predicted to be metallic, which is obviously not true. In fact, d or f orbitals are well localized and there is a gap between the occupied and unoccupied parts. To solve this problem, a regular LDA or GGA method is coupled with the additional orbital-dependent interaction, and this method is the so-called LDA/GGA+U [23,24]. In this methodology, electrons are separated into two subsystems: localized d or f orbitals and delocalized s or p electrons. For the former group, a mean-field type approximation of Coulomb d - d or f - f interaction is applied by considering a $\frac{1}{2}U \sum_{i \neq j} n_i n_j$ (n_i is the site occupation). For the latter group, the regular LDA or GGA

approximation is used. A simple example is illustrated here: Consider a d ion with a fluctuating number of d electrons. In LDA or GGA, the Coulomb d - d interaction energies is $E = \frac{UN(N-1)}{2}$, where $N = \sum n_i$ is the total number of d electrons. If we subtract this term and add a Hubbard-like term, the functional will be like:

$$E = E_{LDA} - \frac{UN(N-1)}{2} + \frac{1}{2}U \sum_{i \neq j} n_i n_j \quad (2.21)$$

The orbital energies ε_i are derivatives of (2.21) with respect to the orbital occupation n_i :

$$\varepsilon_i = \varepsilon_{LDA} + U \left(\frac{1}{2} - n_i \right) \quad (2.22)$$

For occupied orbitals, $n_i = 1$, and $\varepsilon_i = \varepsilon_{LDA} - \frac{1}{2}U$. For unoccupied orbitals, $n_i = 0$, and $\varepsilon_i = \varepsilon_{LDA} + \frac{1}{2}U$. We note now that the effective potential $V_i(r)$ also becomes dependent on the orbital occupancy. This gives the correct physics for Mott-Hubbard insulators, for which the energy gap exists between the upper and lower Hubbard bands.

Another deficiency in LDA/GGA is the uncanceled self-interaction. We have discussed it above and this won't cause trouble for the extended solid systems. However, it will be problematic for atomic or molecular systems. Since the self-interaction term is fully cancelled in the Hartree-Fock method, people sometimes mix the Hartree-Fock theory with LDA or GGA to cancel the self-interaction. The mixing of these two methods is called the hybrid functional. The hybrid functional improves a lot of the accuracy of the molecular and atomic bonding and is very welcomed in the chemistry community [25].

The hybrid functional approach is based on the coupling constant integration:

$$E_{xc} = \int_0^1 U_{XC}^\lambda d\lambda, \quad (2.23)$$

where λ is the coupling-strength parameter. When $\lambda = 0$, U_{xc} is the exchange-correlation potential energy of the non-interacting reference system, which is just the Hartree-Fock exchange energy. When $\lambda = 1$, U_{xc} is the exchange-correlation potential energy of the fully-interacting real system. To first order, the integral (2.23) can be approximated with the linear interpolation:

$$E_{xc} = \frac{1}{2}(U_{XC}^0 + U_{XC}^1), \quad (2.24)$$

where U_{XC}^0 is the pure exchange energy of the Kohn-Sham Slater determinant, and U_{XC}^1 is the exchange-correlation functional of the LDA or GGA. With this hybrid functional, results for the atomization energies, ionization potentials and proton affinities for many molecules and atoms are largely improved [25].

2.4 PSEUDOPOTENTIAL

In a solid state system, electrons can be divided into two groups: core electrons and valence electrons. Core electrons are tightly bound to ionic cores and hardly take part in the chemical bonding, while valence electrons determine the bonding of atoms, which form molecules and crystals. On the other hand, WFs of valence electrons oscillate rapidly near the core region, as to be orthogonal to WFs of core electrons. As will be discussed in Section 2.5, usually people take plane waves as the basis set. From this point of view, to correctly describe valence electrons, a very large plane-wave basis set is needed. This will make the calculation extremely difficult.

The pseudopotentials are constructed to reproduce the scattering of the full ionic potential. Since core electrons remain almost unchanged during interaction, and valence electrons feel an effective core screened by core electrons, the sharp Coulomb potential near the core region can be replaced by an effective pseudopotential, which keeps the

nuclei and core states frozen. As a consequence, all-electron WFs of valence electrons are replaced with much smoother WFs, and valence electrons can still be accurately described outside the core region. The comparison between the all-electron WF and pseudo WF is illustrated in Figure 2.3 below.

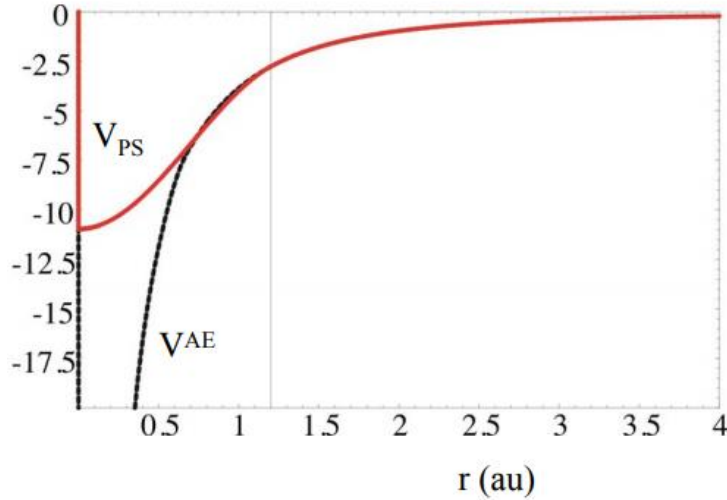


Figure 2.3 Comparison between the all-electron WF and pseudo WF. We can see the pseudo WF is much smoother than all-electron WF in the near-core region but matches it pretty well outside that region.

Three different pseudopotentials are most popular in the community: the norm-conserving pseudopotentials [26], ultrasoft pseudopotentials [27] and projected augmented wave method [28]. Most of the pseudopotentials are based on all-electron calculations. By assuming a spherical screening approximation, we could solve Kohn-Sham equation:

$$\left[-\frac{1}{2} \frac{d^2}{dr^2} + \frac{l(l+1)}{2r^2} + V[\rho; r] \right] rR_{nl}(r) = \varepsilon_{nl} R_{nl}(r), \quad (2.25)$$

where $V[\rho; r]$ is the one-electron potential. It includes three parts:

$$V[\rho; r] = -\frac{Z}{r} + V_H[\rho; r] + V_{xc}^{LDA}(\rho(r)) \quad (2.26)$$

Here, $V_H[\rho; r]$ is the Hartree potential, $V_{xc}^{LDA}(\rho(r))$ is the exchange-correlation potential and $\rho(r)$ is the corresponding electron density of occupied WF $R_{nl}(r)$. For a “norm-conserving” pseudopotential, it needs to satisfy several different conditions: First, we want the pseudo WFs have non nodes to make it as smooth as possible. Second, the angular momentum l component of the radial pseudo WF should be equal to the all-electron WF beyond a cutoff radius r_c :

$$R_l^{PP}(r) = R_l^{AE}(r), \quad r > R_c \quad (2.27)$$

Third, the charge within r_c should be equal to both WFs:

$$\int_0^{r_c} |R_l^{PP}(r)|^2 r^2 dr = \int_0^{r_c} |R_l^{AE}(r)|^2 r^2 dr, \quad (2.28)$$

where PP and AE stands for pseudopotential and all-electron, respectively. This is where the terminology “norm conserving” comes from. Fourth, eigenvalues for two WFs also should be the same:

$$\varepsilon_l^{PP} = \varepsilon_l^{AE} \quad (2.29)$$

It is clear that the pseudo WF is not unique so we have freedom to choose a desired form. Once the pseudo WF is fixed, we can get the screened pseudopotential by inverting equation (2.25):

$$V_{scr,l}^{PP}(r) = \varepsilon_l - \frac{l(l+1)}{2r^2} + \frac{1}{2rR_l^{PP}(r)} \frac{d^2}{dr^2} [rR_l^{PP}(r)] \quad (2.30)$$

Equation (2.30) tells us that in order to have a continuous PP, the pseudo WF should have continuous derivatives up to second order, and also behave as r^l at the origin. The continuity of the first derivative also indicates that at the point r_0 the WF is uniquely determined by its logarithmic derivative:

$$\left. \frac{d}{dr} \ln[R_l(r, \varepsilon)] \right|_{r=r_0} = \frac{1}{R_l(r, \varepsilon)} \left. \frac{dR_l(r, \varepsilon)}{dr} \right|_{r=r_0} \quad (2.31)$$

This leads the condition (2.27) to become:

$$\frac{1}{R_l^{PP}(r, \varepsilon)} \frac{dR_l^{PP}(r, \varepsilon)}{dr} = \frac{1}{R_l^{AE}(r, \varepsilon)} \frac{dR_l^{AE}(r, \varepsilon)}{dr} \quad (2.32)$$

There is another important property of the PP which is called “transferability”. This means that if the pseudopotential generated for atom is in chemical environments such as solids or molecules, the calculation results are the same compared with the all-electron calculations in that environment. The simple approach to increase the transferability is to decrease r_c so $R_l^{PP}(r)$ is equal to $R_l^{AE}(r)$ in a larger range. However, that means we need to have more Fourier components in the plane-wave basis as when r_c decreases, $R_l^{AE}(r)$ rapids more rapidly. This indicates that if we want to improve the transferability, we have to sacrifice the smoothness of the pseudopotential.

Troullier and Martins [26] suggested a method for generating smooth pseudopotentials. The pseudo WF is defined as:

$$R_l^{PP}(r) = \begin{cases} R_l^{AE}(r) & r \geq r_c \\ r^l \exp[p(r)] & r \leq r_c \end{cases} \quad (2.33)$$

where $p(r)$ is a polynomial of order six in r^2 ,

$$p(r) = c_0 + c_2 r^2 + c_4 r^4 + c_6 r^6 + c_8 r^8 + c_{10} r^{10} + c_{12} r^{12} \quad (2.34)$$

The seven coefficients can be determined by seven conditions, which are one norm-conservation, five continuity conditions of the pseudo WF and its derivatives up to the fourth order, and zero curvature of the pseudo WF at the origin.

Norm-conserving pseudopotentials reach the goal of accuracy, but the “transferability” is lost to some extent. A different approach was suggested by Vanderbilt [27]. There, the norm-conservation condition is relaxed, which would cause a charge deficit in the core region. But the pseudo WF is allowed to be softer, and the scattering properties and the transferability of the pseudo potential can be improved by using projector function for each angular momentum channel. This method reduces the size of plane-wave basis set compared with the norm-conserving pseudopotential.

However, more projections and operations are needed, which also decreases the computational efficiency.

The projector augmented wave method is an approach to reformulate the orthogonalized plane wave method. The strategy of this method is to divide the valence WF into a partial-wave expansion within an atom-centered sphere and envelope functions outside the spheres. The envelope function is expanded into plane waves or some other convenient basis set. Then two parts are matched with the value and the derivative at the sphere radius. The integrals of WFs are evaluated by the augmentation method. Different from other two methods discussed above, this method keeps the all-electron WF instead of the pseudo WF. First, a smooth pseudo WF $\tilde{\psi}(r)$ can be defined and a linear transformation can connect this pseudo WF $\tilde{\psi}(r)$ and the all-electron WF $\psi(r)$:

$$\psi(r) = T\tilde{\psi}(r) \quad (2.35)$$

Since $\tilde{\psi}(r)$ is smooth, it can be expanded with different partial waves m in each sphere:

$$|\tilde{\psi}\rangle = \sum_m c_m |\tilde{\psi}_m\rangle \quad (2.36)$$

Hence the all-electron WF is written as:

$$|\psi\rangle = |\tilde{\psi}\rangle + \sum_m c_m \{|\psi_m\rangle - |\tilde{\psi}_m\rangle\} \quad (2.37)$$

If the transformation is linear, then coefficients can be obtained by projection in each sphere:

$$c_m = \langle \tilde{p}_m | \tilde{\psi} \rangle \quad (2.38)$$

For projection operator (vector) \tilde{p}_m , it satisfies the orthogonal condition:

$$\langle \tilde{p}_m | \tilde{\psi}_{m'} \rangle = \delta_{mm'} \quad (2.39)$$

Therefore, the all-electron valence WF can be obtained from the pseudo valence WF:

$$|\psi\rangle = |\tilde{\psi}\rangle + \sum_m \langle \tilde{p}_m | \tilde{\psi} \rangle \{|\psi_m\rangle - |\tilde{\psi}_m\rangle\} \quad (2.37)$$

For any operator \hat{A} in the original all-electron problem, a transformed operator \tilde{A} operating on the pseudo WF can also be introduced:

$$\tilde{A} = T^+AT = A + \sum_{m,n} |\tilde{p}_m\rangle (\langle \psi_m | A | \psi_n \rangle - \langle \tilde{\psi}_m | A | \tilde{\psi}_n \rangle) \langle \tilde{p}_n | \quad (2.38)$$

This method has been incorporated in VASP and we use this method for most calculations in this dissertation.

2.5 PLANE-WAVE BASIS

Equation (2.4) has shown that the many-electron problem in a solid can be approximated as a one-electron problem, and all the many-body terms can be incorporated into an effective one-electron potential $V_{eff}(\mathbf{r})$. Typically in a crystal atoms are arranged periodically so the effective potential is also periodic:

$$V(\mathbf{r} + \mathbf{R}) = V(\mathbf{r}) \quad (2.39)$$

Here \mathbf{R} is the Bravais lattice vector. With a periodic potential, WF of electrons solved from equation (2.4) will have the form:

$$\psi_{\mathbf{k}}(\mathbf{r}) = e^{i\mathbf{k}\cdot\mathbf{r}} u_{\mathbf{k}}(\mathbf{r}) \quad (2.40)$$

where

$$u_{\mathbf{k}}(\mathbf{r} + \mathbf{R}) = u_{\mathbf{k}}(\mathbf{r}) \quad (2.41)$$

This is called Bloch theorem, and it indicates that the one-electron WF in solids can be written as a product of a plane wave and a periodic function. Considering that any periodic function can be expanded in a complete reciprocal lattice vector basis set, we get:

$$\psi_{\mathbf{k}}(\mathbf{r}) = \frac{1}{\sqrt{\Omega}} \sum_{\mathbf{G}} c_{i,\mathbf{G}} e^{i(\mathbf{q}+\mathbf{G})\cdot\mathbf{r}}, \quad (2.42)$$

where Ω is the volume of the solid, \mathbf{G} is the reciprocal lattice vector and \mathbf{q} is the plane-wave vector \mathbf{k} within the first Brillouin zone. On the other hand, since $V_{eff}(\mathbf{r})$ is periodic, we can also do a Fourier expansion for $V_{eff}(\mathbf{r})$ to get the Fourier components:

$$V_G = \frac{1}{\Omega_0} \int d\mathbf{r} e^{-i\mathbf{G}\cdot\mathbf{r}} V(\mathbf{r}), \quad (2.42)$$

where Ω_0 is the volume of the unit cell. All of these suggest that it is convenient to solve the one-electron Schrodinger equation in the reciprocal space.

First we get the matrix element for the kinetic energy term:

$$\left\langle \mathbf{G}' \left| -\frac{\nabla^2}{2} \right| \mathbf{G} \right\rangle = \frac{\hbar^2 |\mathbf{G}|^2}{2m} \delta_{\mathbf{G},\mathbf{G}'} \quad (2.43)$$

Then we get the matrix element for the $V_{eff}(\mathbf{r})$ term:

$$\left\langle \mathbf{G}' \left| -V_{eff}(\mathbf{r}) \right| \mathbf{G} \right\rangle = V_{\mathbf{G}-\mathbf{G}'} \quad (2.44)$$

Therefore, we will have N_q independent matrices, and for each matrix, the size is $(N_G \times N_G)$, where N_q is the number of k points in the first Brillouin zone, and N_G is the number of Fourier components determined by the cutoff energy parameter E_{cutoff} ($E_{cutoff} = \frac{\hbar^2 \mathbf{G}^2}{2m}$). Typically, for the transition metal oxide, we take the value as 600 eV.

With all these Matrix elements, we could solve the Schrodinger equation:

$$\sum_{n'} H_{n,n'}(\mathbf{q}) c_{i,n'}(\mathbf{q}) = \varepsilon_i(\mathbf{q}) c_{i,n'}(\mathbf{q}) \quad (2.45)$$

The dimension of $c_i(\mathbf{q})$ is the number of Fourier components N_G , equal to the number of bands in the band structure.

As for a specific calculation, it involves integration over the Brillouin zone. The continuous integration can be replaced by summation over a finite grid of k points. The most widely adopted scheme to sample the Brillouin zone was proposed by Monkhorst and Pack [29]. In a three-dimensional system, the three reciprocal lattice vectors along

each lattice vector are recorded as \mathbf{b}_1 , \mathbf{b}_2 and \mathbf{b}_3 , respectively. Coordinate of each k point is given as:

$$\mathbf{k}_{prs} = u_p \mathbf{b}_1 + u_r \mathbf{b}_2 + u_s \mathbf{b}_3, \quad (2.46)$$

where $u_r = \frac{2r - q_r - 1}{2q_r}$, $r = 1, 2, \dots, q_r$. q_r determines number of k points in the r direction and all $q_r \times q_p \times q_s$ points are distributed homogenously over the Brillouin zone.

Another function is defined as:

$$A_m(\mathbf{k}) = N_m^{-1/2} \sum_{|\mathbf{R}| \in C_m} e^{i\mathbf{k} \cdot \mathbf{R}}, \quad (2.47)$$

where the sum is over all \mathbf{R} vectors which are related by the operations of the lattice point group. N_m is the number of members in the m th star of \mathbf{R} . Therefore, any integration function $f(\mathbf{k})$ can be approximated as a summation of $A_m(\mathbf{k})$:

$$f(\mathbf{k}) = \sum_m f_m A_m(\mathbf{k}) \quad (2.48)$$

We note that the lattice point group can reduce the summation work significantly and will influence the weight factor for inequivalent k points. Here we give a simple example. Consider a two-dimensional lattice and we take 4 points along both the row and column. As illustrated in Figure 2.4, there are only 3 inequivalent k points while all other k points are actually related to them due to symmetry. In the entire Brillouin zone, k_1 appears 4 times, k_2 appears 4 times, and k_3 appears 8 times. Therefore we have different weights for different k points and the integral can be written as:

$$\frac{1}{\Omega_{BZ}} \int_{BZ} F(\mathbf{k}) d\mathbf{k} \approx \frac{1}{4} F(\mathbf{k}_1) + \frac{1}{4} F(\mathbf{k}_2) + \frac{1}{2} F(\mathbf{k}_3) \quad (2.49)$$

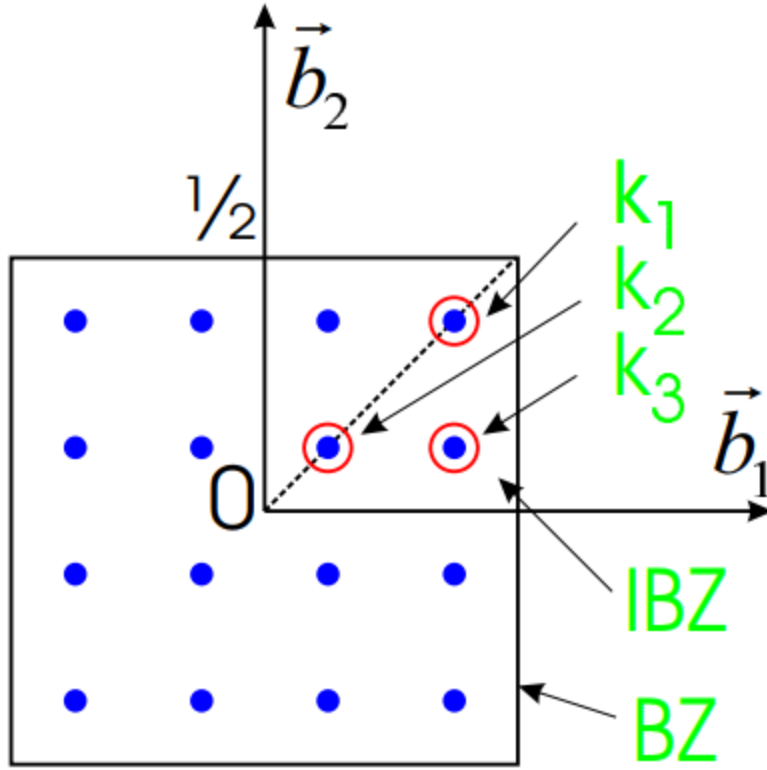


Figure 2.4 An illustration of Monkhorst-Pack Scheme. For two-dimensional lattice, 16 k points can be reduced to 3 inequivalent k points [30,31].

Consider an operator X : The expectation value $\langle X \rangle$ is obtained by integrate the matrix elements over the first Brillouin zone first, and then sum over all occupied bands:

$$\begin{aligned} \langle X \rangle &= \frac{1}{V_G} \sum_n \int d^3 \mathbf{k} X_n(\mathbf{k}) f(\varepsilon_n(\mathbf{k})) \\ &= \frac{1}{V_G} \sum_n \int d^3 \mathbf{k} \langle \Psi_n(\mathbf{k}) | X | \Psi_n(\mathbf{k}) \rangle f(\varepsilon_n(\mathbf{k})), \end{aligned} \quad (2.50)$$

where V_G is the volume of the reciprocal unit cell, and $f(\varepsilon)$ is the occupation number. To compute $f(\varepsilon_n(\mathbf{k}))$, different methods are used to determine the partial occupancy $f(\varepsilon_n(\mathbf{k}))$ for each orbital. Three methods are most widely used: the Gaussian-smearing method, the Methfessel-Paxton order N method [32] and the tetrahedron method. The

Methfessel-Paxton method usually works well for the metal. For semiconductors and insulators, the tetrahedron method is often used [33]. The procedure is to first divide the Brillouin zone into different tetrahedral (Figure 2.5), and then linearly interpolate $X_n(\mathbf{k})$ within each tetrahedron (Figure 2.6), and eventually integrate the interpolated function \widetilde{X}_n by performing the summation with different weights:

$$\langle X \rangle = \sum_{j,n} X_n(\mathbf{k}_j) \omega_{nj} \quad (2.51)$$

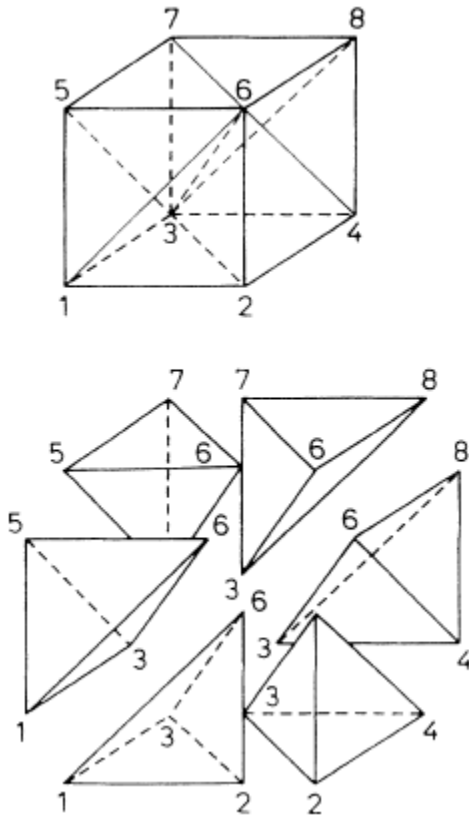


Figure 2.5 Break-up of a submesh cell into six tetrahedra [33].

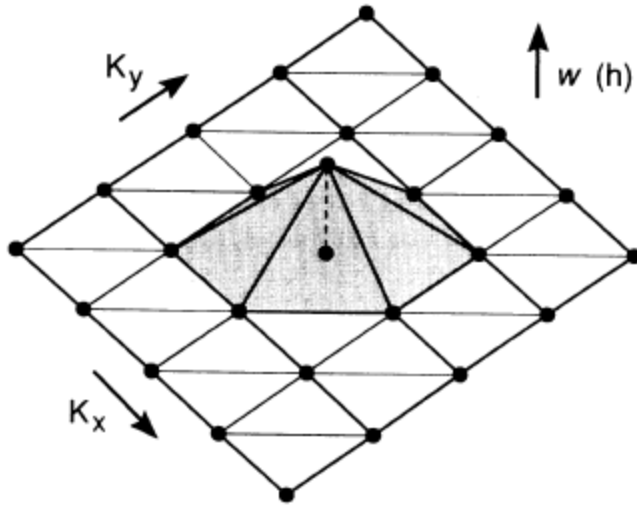


Figure 2.6 Illustration of the linearly-interpolated weight function $\omega_j(\mathbf{k})$ that is used in integration [33].

2.6 REAL SPACE DENSITY FUNCTIONAL METHOD

The plane-wave based DFT method has been widely used. However, for localized systems, such as clusters, nanocrystals and slabs, the plane-wave method is not efficient due to the broken periodicity. We can still use it by taking a large supercell with thick vacuum, but the computational cost is large. Also, for a charged system, the supercell approach would give a divergent value of the total energy. To avoid it, a compensating background charge needs to be provided.

Chelikowsky *et al.* developed a finite-difference method to solve the Kohn-Sham Schrodinger-like equation on a real space grid [34]. On a uniform orthogonal three-dimensional grid with points (x_i, y_j, z_k) , the kinetic energy laplacian operator can be expanded:

$$\frac{\partial^2 \psi}{\partial x^2} = \sum_{n=-N}^N C_n \psi(x_i + nh, y_j, z_k) + O(h^{2N+2}), \quad (2.52)$$

where h is the grid spacing. In a real space finite-difference-method, the grid spacing plays the role of the cutoff energy in a plane-wave calculation, which can be approximated by $\pi^2/2h^2$, if h is in atomic unit [35]. The approximation can be accurate to the order of $O(h^{2N+2})$ and the grid spacing h needs to be refined until the calculation is converged. To describe a localized system with this approach, a confining domain condition is adopted. The domain dimension should be large enough to allow the WF to vanish at the domain boundary. Overall, the Kohn-Sham equation on a real space grid is:

$$\begin{aligned} & -\frac{\hbar^2}{2m} \left[\sum_{n=-N}^N C_n \psi(x_i + nh, y_j, z_k) + \sum_{n=-N}^N C_n \psi(x_i, y_j + nh, z_k) \right. \\ & \left. + \sum_{n=-N}^N C_n \psi(x_i, y_j, z_k + nh) \right] \\ & + [V_{ion}(x_i, y_j, z_k) + V_H(x_i, y_j, z_k) + V_{xc}(x_i, y_j, z_k)] \psi(x_i, y_j, z_k) \\ & = E \psi(x_i, y_j, z_k), \end{aligned} \quad (2.53)$$

where V_{ion} is the nonlocal pseudopotential, V_H is the Hartree potential, and V_{xc} is the exchange-correlation potential. The number of grid points M is proportional to the domain size and inverse to the grid spacing. Accordingly, the Hamiltonian matrix has the size of $M \times M$.

As an example, we use the real-space-pseudopotential code PARSEC to investigate the local work function variation around 3D metallic nanocrystals [34,36,37]. This work has been published as Lingyuan Gao, Jamie Souto-Casares, James R. Chelikowsky, Alexander A. Demkov, *J. Chem. Phys.*, **147**, 214301 (2017). Aluminum nanocrystals are examined. The local work function can be considered as the difference between Fermi level and the local electrostatic potential outside the crystal. For a nanocrystal, the potential can vary from one facet to another. We consider two Al

nanocrystals: a tetrakaidecahedron and a cuboid shown in Figure 2.7(a) and Figure 2.7(b), respectively. The two structures were generated from a bulk supercell and are highly symmetric, which improves the convergence of the calculations. Our tetrakaidecahedron contains 490 atoms and has six (001)-oriented and eight (111)-oriented facets and the cuboid has two (001)-oriented and four (110)-oriented facets and contains 371 atoms, thus all low-index surfaces are considered. Our spherical domain has a radius of 25 Å to avoid any artifacts of the artificial confinement. All structures are fully relaxed. The residual interatomic forces are less than 0.1 eV/Å.

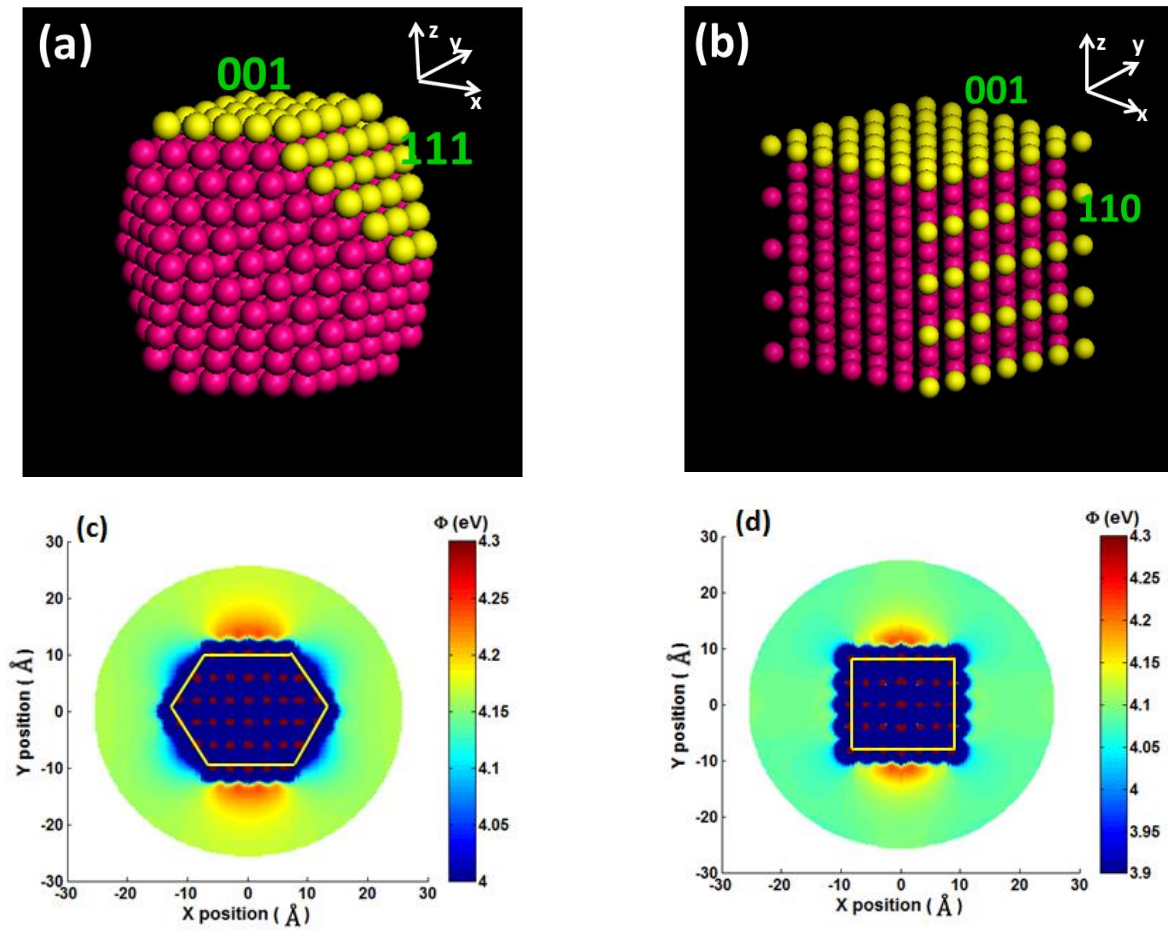


Figure 2.7 (a) A tetrakaidecahedron nanocrystal with the (001) and (111) facets, (b) A cuboid nanocrystal with (001) and (110) facets, (c) The relative potential of a tetrakaidecahedron nanocrystal across the $x + y = 0$ plane, (d) The relative potential of a cuboid nanocrystal across the $x + y = 0$ plane. In (a) and (b), surface atoms are highlighted yellow.

We plot the relative potential across a plane defined by $x + y = 0$. In this manner, we can observe the potential change around different facets. Figure 2.7(c) shows the corresponding cut through the tetrakaidecahedron. Gold lines indicate the geometric edges (the line drawn through the atomic centers) of the nanocrystal. On this hexagonal

cross section, two horizontal edges belong to the (001) surface, while the other four belong to the (111) surface. The value inside the crystal has no physical significance as we reference to the Fermi energy. From Figure 2.7(c), 4 Å above the (001) facet, the potential is 4.2 eV, while at the same height above the (111) facet, it is 100 meV lower. At larger distances, the potential decreases along the (001) direction but increases along (111); at approximately 1 nm above the surface, it merges to a single value of 4.15 eV.

Variation around the crystal implies that there are directions along which it is easier for electron to leave the crystal. In order to escape through the (001) facet, an electron needs to overcome the 4.2 eV potential barrier near that surface. This means 4.2 eV is the local work function for the (001) facet of a tetrakaidecahedron. For the (111) facet, as the potential changes monotonously, the minimum work to free an electron through this facet is 4.15 eV.

Similarly, the anisotropy is also found for the cuboid crystal shown in Figure 2.7(d). The potential reaches the maximum value of 4.2 eV near (001) facet and then drops to 4.09 eV at large distances, while outside (110) facet, potential does not significantly vary and is fixed near 4.09 eV. Thus, the local work function (LWF) of the (001) facet in cuboid is counted as 4.2 eV and the LWF of (110) facet is 4.09 eV.

Alternatively, we generate another type of local electrostatic potential map by plotting the potential *relative to the Fermi level* at planes parallel to each facet slightly “above” the crystal surface. For tetrakaidecahedron, potentials 4 Å above the (001) and (111) facets are shown in Figure 2.8(b) and Figure 2.8(e). As can be seen, the potential is uniform in the central region, which is right above the surface of nanocrystal, as highlighted in Figure 2.8(a) and Figure 2.8(d). For a plane parallel to (001) facet, the potential at the central square is approximately 4.20 eV, or 50~100 meV higher than in other regions on that plane. In contrast, at the center of a plane parallel to the (111) facet,

local work function is only 4.10 eV, and this is the low value for this plane. Thus, a difference of the order of 100~150 meV is observed between the potential values above the (001) and (111) facets of the nanocrystal. Further away from the nanocrystal, the difference diminishes and potential converges to a single value of 4.17 eV approximately 1 nm away from the crystal, as shown in Figure 2.8(c) and Figure 2.8(f).

Results for the cuboid nanocrystal are also shown in Figure 2.8(g) to 2.8(l). The electrostatic potential 4 Å above the (110) facet is 4.10 eV, or 100 meV lower than that for the (001) facet. But at a larger distance, the potential around the nanocrystal converges to 4.09 ± 0.01 eV. Near the (001) facet, a nearly uniform, high potential area is roughly the size of a 6×6 atomic array instead of the entire surface layer. This is different from the case of the tetrakaidecahedron. We note that for the potential 4 Å above the (110) facet (Figure 2.8(k)), the potential extrema are not located in the center, but are along the edge. This feature has been discussed for the work function of two dimensional metallic nanowires and is attributed to the sharp edge feature of the cuboid [38,39].

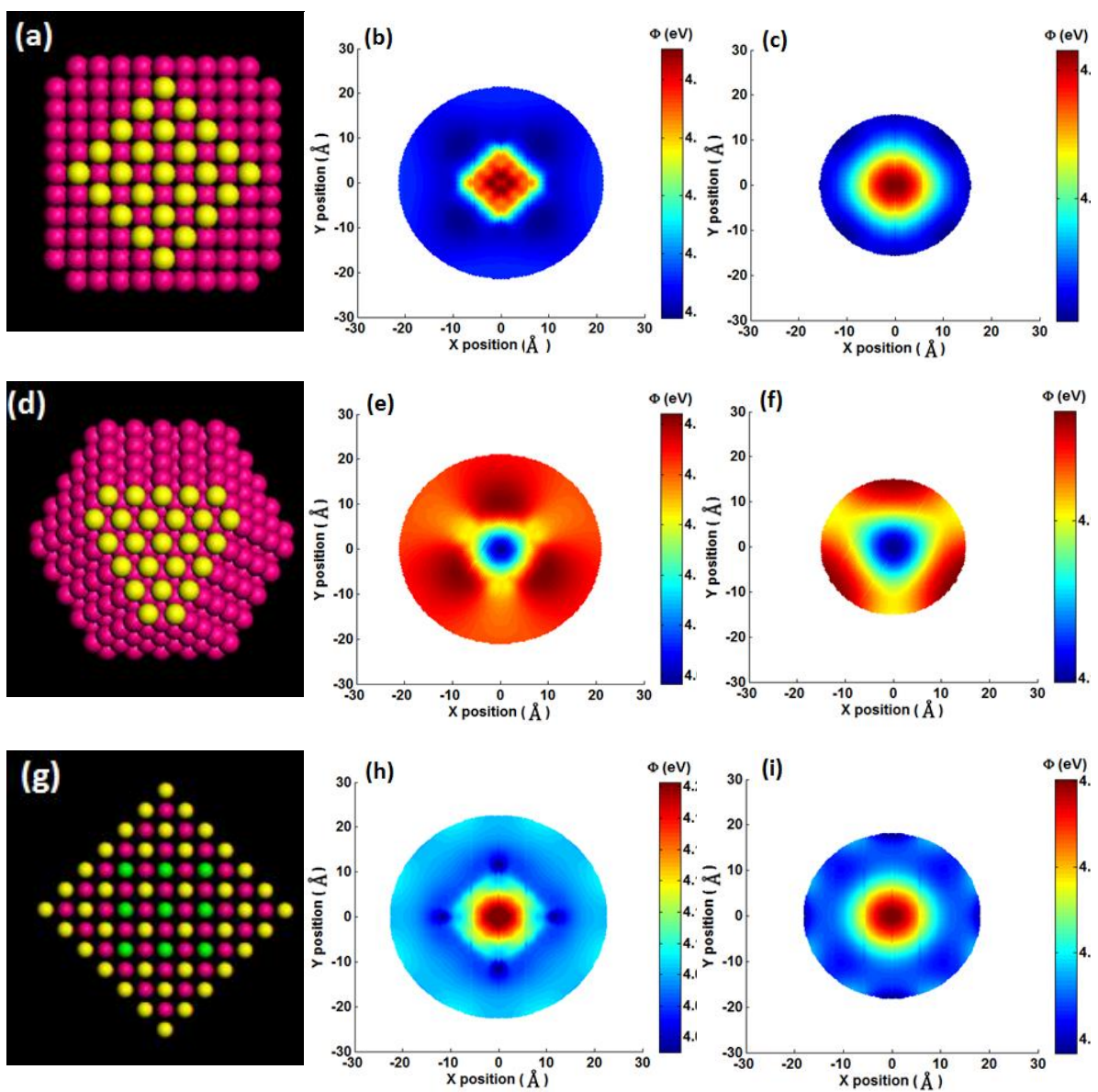


Figure 2.8 (continued on next page)

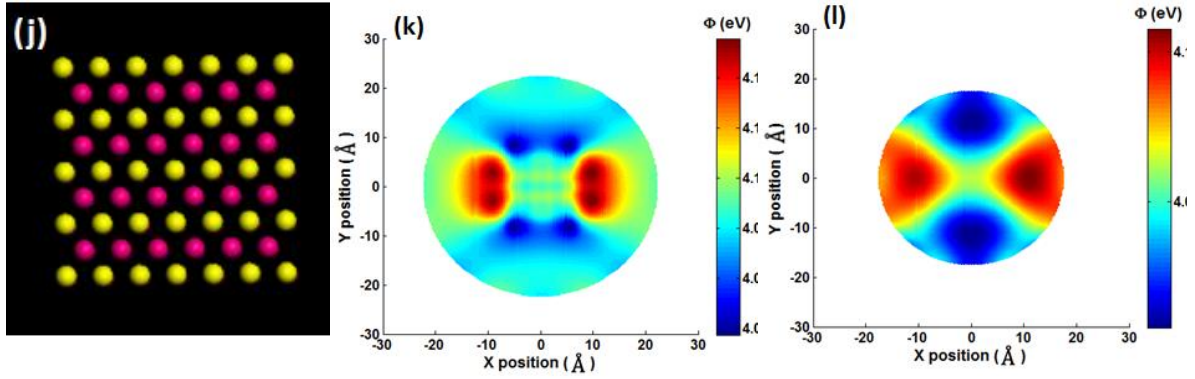


Figure 2.8 The relative electrostatic potential viewed across differently sliced planes: (a) to (f) are for the tetrakaidecahedron and (g) to (l) are for the cuboid. (a) The atomic view of a (001) facet, (b) the potential across the plane placed 4 Å above the (001) facet, (c) same 1 nm above the (001) facet, (d) the atomic view of the (111) facet, (e) the potential across the plane placed 4 Å above the (111) facet, (f) same 1 nm above the (111) facet, (g) The atomic view of a (001) facet, (h) the potential across the plane placed 4 Å above the (001) facet, (i) same 1 nm above the (001) facet, (j) The atomic view of a (110) facet, (k) the potential across the plane placed 4 Å above the (110) facet, (l) same 1 nm above the (110) facet. In (a) and (d), surface atoms are highlighted yellow.

In addition, we calculate the ionization potential (IP) for five cuboid clusters of different sizes. IP is defined as the energy needed to remove an electron from the system. Ideally, in the bulk limit, IP is equal to the work function. However, for nano-sized clusters, two values become different as this will be discussed in the following. Owing to the confined boundary conditions employed in PARSEC, calculations of a charged system are readily done. We calculate IPs by subtracting the total energies of the N - and $N - 1$ -electron systems. Sizes of these cuboids are $7 \times 7 \times 5$, $6 \times 6 \times 5$, $5 \times 5 \times 5$, $4 \times 4 \times 4$ and $3 \times 3 \times 3$ and the corresponding numbers of atoms, n , are 389, 280, 189, 91 and 35, respectively. It has been suggested that the size-dependent ionization potential can be calculated using the following equation [40–42]:

$$I_n = W + \frac{3e^2}{8R_n} = W + \frac{3e^2}{8r_0} n^{-1/3}, \quad (2.54)$$

where R_n is the cluster radius and r_0 is the atomic radius. The first term W corresponds to the bulk work function value. The second term arises from a classical electrostatic effect: the electronic level of a charged cluster is shifted relative to a neutral cluster upon ionization. This has two contributions: The image potential at the surface of a metallic sphere is $\frac{5}{8} \frac{e^2}{r_0} n^{-1/3}$ larger than that near a neutral metallic slab, which leads to a decrease of bulk work function. On the other hand, once the electron is liberated by photons, there will be an additional attraction between the electron and a remaining positive charge $+e$ on the isolated sphere, which gives rise to an additional energy $\frac{e^2}{r_0} n^{-1/3}$. As a result, the work function will increase by $\frac{3}{8} \frac{e^2}{r_0} n^{-1/3}$. This is the so-called conducting sphere droplet (CSD) model. The results are shown in Figure 2.9 along with a fitting line. The IP has a linear dependence on $n^{-1/3}$, in good agreement with theory. Also, the bulk work function value of 3.88 eV extrapolated from the data is close to 4.11 eV of a (110)-orientation plane from a slab calculation. Also, from this line, we see change of IP can be as much as 1.5 eV when cluster size is varied, which is on the same scale as IP of gold clusters [43]. We note that the disparity between the IP and the work function is significant when the cluster size is small, and this can be attributed to the electronic level shift of a finite system as discussed above. Due to this effect, the IP is larger than the work function for clusters of a finite size. In our tetrakaidecahedron and cuboid, the calculated IP is about 0.4 eV higher than the work function. When the cluster size gradually increases, the IP approaches the work function.

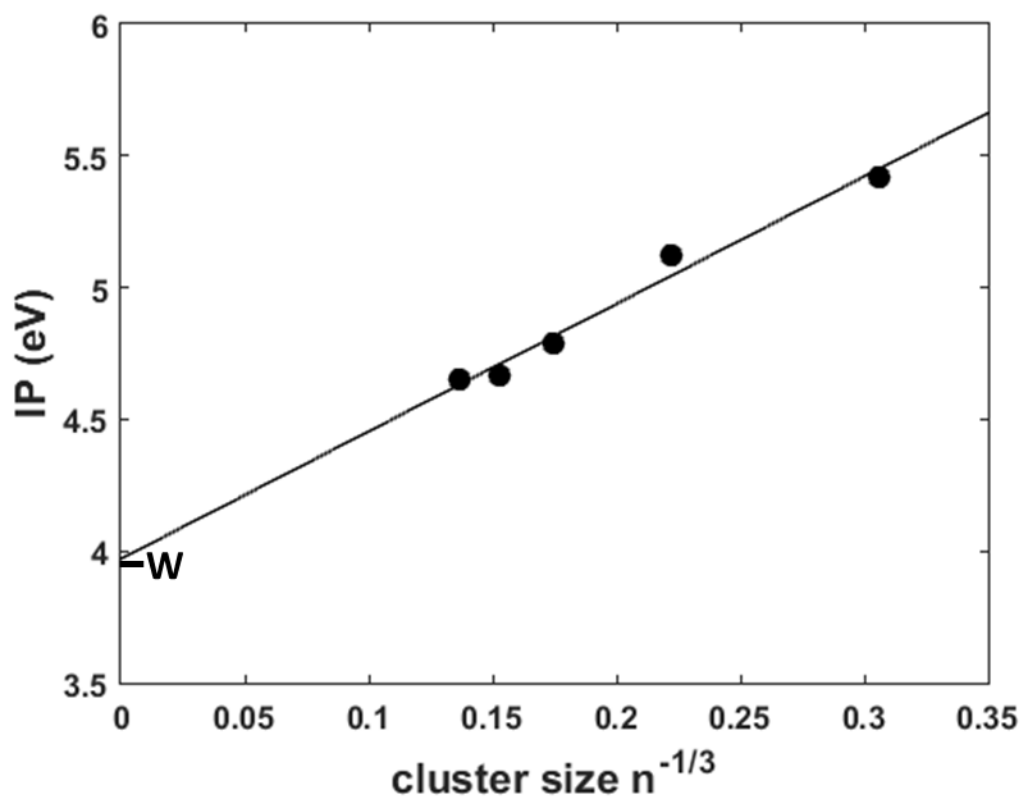


Figure 2.9 The calculated ionization potentials for five cuboids of different sizes. A fitting line is also plotted to show the linear relationship between atom number $n^{-1/3}$ and ionization potential (IP). Intercept of the fitting line is noted as the bulk work function W .

Chapter 3 Effect of oxygen vacancies and strain on the phonon spectrum of HfO₂ thin films

In this chapter, the effect of strain and oxygen deficiency on the Raman spectrum of monoclinic HfO₂ is investigated theoretically using first-principle calculations. 1% in-plane compressive strain applied to *a* and *c* axes is found to blue shift the phonon frequencies, while 1% tensile strain does the opposite. The simulations are compared to and good agreement is found with experimental results of Raman frequencies greater than 110 cm⁻¹ on 50 nm HfO₂ thin films. Several Raman modes measured below 110 cm⁻¹ and previously assigned to HfO₂ are found to be rotational modes of gases present in air ambient (nitrogen and oxygen). However, localized vibrational modes introduced by threefold-coordinated oxygen (O₃) vacancies are identified at 96.4 cm⁻¹ computationally. These results are important for a deeper understanding of vibrational modes in HfO₂, which has technological applications in transistors, and particularly in resistive random-access memory (RRAM) whose operation relies on oxygen-deficient HfO_x.

Results have been published as: Lingyuan Gao, Eilam Yalon, Annabel R. Chew, Sanchit Deshmukh, Alberto Salleo, Eric Pop, and Alexander A. Demkov, J. Appl. Phys. 121, 224101 (2017). For the experimental work, E.Y. measured the Raman spectra. A.R.C. performed X-ray diffraction measurements.

3.1 INTRODUCTION

Hafnium dioxide (HfO₂) or hafnia is an important transition metal oxide that finds applications in information technology as a gate dielectric in field effect transistors [44–46], as a resistive switching material in memory devices [47], and in optical coatings [48]. As such, it has been studied extensively both theoretically and experimentally [49–62]. In particular, fundamental Raman frequencies of the HfO₂

monoclinic phase have been previously reported [50–54,56,57,60,63]. However, in electronic applications, thin films of HfO_2 are typically sputtered or grown by atomic layer deposition (ALD) and are often subject to stoichiometric deviations and strain [49,64–66]. Strain, induced by either thermal or lattice mismatch, may shift or even split Raman peaks [67–70]. In bulk ceria, for example, lattice expansion causes a substantial softening of the B_{1u} mode [71]. In Li_2O , when the volume is increased around the superionic transition point, the zone boundary transverse acoustic mode along [110] at the X point is found to be softened [72,73]. On the other hand, oxygen vacancies, as one of the most common defects in the sample [74,75], can also lead to shifts in phonon frequencies or even to the appearance of normally symmetry-forbidden first-order Raman peaks [56,76,77]. In addition, Raman spectroscopy has been previously used to characterize impurities and phase in hafnia films under different annealing conditions [78–81]. Thus, it is of fundamental interest to investigate the effects of strain and oxygen vacancies on the phonon spectrum of hafnia. Furthermore, low wavenumber peaks in the range below 110 cm^{-1} were previously reported experimentally [52–54], but were not found computationally in stoichiometric unstrained monoclinic HfO_2 [50,56–58].

In this chapter we carry out first principles calculations and analysis of Raman spectra of hafnia under compressive and tensile strain, and in the presence of oxygen vacancies. In the case of strain we compare the results of calculations with experimental data obtained for HfO_2 films deposited by sputtering on thin (50 nm) Au and Pt films on sapphire substrates. The low wavenumber peaks (below 110 cm^{-1}) are carefully examined. The chapter is organized as follows. The calculation and experimental methods are described in Section 3.2. The phonon spectrum of bulk monoclinic hafnia is discussed in Section 3.3. The influence of strain on the zone-center frequencies is

discussed in Section 3.4. We discuss the effect of oxygen vacancies in Section 3.5 and summarize our findings in Section 3.6.

3.2 COMPUTATIONAL AND EXPERIMENTAL METHOD

All calculations are carried out using the Vienna *ab initio* simulation package (VASP) [30,31]. The exchange-correlation functional is approximated within the local density approximation (LDA) and projector-augmented-wave (PAW) pseudopotentials are used. The electronic configuration for Hf is $5d^2 6s^2$ and $2s^2 2p^4$ for O. The use of PAW pseudopotentials allows one to achieve a total energy convergence of 10^{-8} eV/atom with a cutoff energy of 600 eV. An $8 \times 8 \times 8$ Monkhorst k -point mesh is used for the Brillouin zone (BZ) integration for the monoclinic simulation cell. Full structural relaxation is performed until the Hellman-Feynman forces are less than 10^{-4} eV/Å.

We calculate the phonon dispersion within the harmonic approximation by using the “frozen phonon method.” Force constants in a $2 \times 2 \times 2$ supercell are calculated with the Phonopy code [82]. The phonopy code generates the structure according to crystal symmetry, which reduces the computational load significantly. The dynamical matrix is computed *via* the lattice Fourier transformation and frequencies across the BZ are obtained from the eigenvalues of the dynamical matrix.

A neutral oxygen vacancy is simulated by removing one oxygen atom from the supercell and in our case, this corresponds to a vacancy concentration of 1.56%. Owing to the large size of the supercell, for the defect case, only the Γ -point frequencies are computed as this is sufficient to account for the Raman-active modes.

Because the measured Raman signal of thin HfO₂ films is very weak and often only the Raman spectrum of the substrate is detected, we used here a thin metal film to

block the substrate signal. In addition, this structure is technologically relevant for resistive random-access memory (RRAM) devices, where thin HfO₂ is deposited on a metal electrode. HfO₂ films were deposited by room temperature reactive sputtering from an Hf target in an Ar:O₂ (7:3) plasma at 4 mT, with a forward RF power of 150 W, on thin (50 nm) Au and Pt films on sapphire substrates. The as-deposited 50 nm thick amorphous HfO₂ film did not show any clear Raman features. After annealing at 600 °C for 30 minutes in air the HfO₂ partially crystallized to the monoclinic phase, which is confirmed by X-ray diffraction (XRD), and Raman features were observed. Measurements were obtained using a Horiba LabRAM HR with 532 nm and 633 nm lasers operated at 2.5 mW and 2 mW, respectively, at room temperature. Structural characterization was carried out using a PANalytical X'Pert PRO X-ray diffractometer equipped with a copper K_α source. The XRD measurement was carried out at a small grazing incidence (1°) to increase the path length of the probing X-ray beam, as well as to minimize diffraction from the underlying substrate.

3.3 PHONON SPECTRUM OF MONOCLINIC HAFNIA

Bulk crystalline hafnia has three phases: the cubic structure at high temperature (space group $Fm\bar{3}m$), the tetragonal structure (space group $P4_2/nmc$) and the monoclinic structure at low temperature (space group $P2_1/c$). In this work we only consider the monoclinic structure. We list the optimized structural parameters of hafnia compared with experimental data in Table 3.1. Also, Hf cation is at the Wyckoff position $4e$ (0.277, 0.042, 0.208), while threefold-coordinated O₃ anion and fourfold-coordinated O₄ anion are at $4e$ (0.073, 0.341, 0.337) and $4e$ (0.446, 0.759, 0.483), respectively. This agrees well with data reported previously [50]. The theoretical volume is a little

smaller than the experimental value, as the LDA tends to overbind, resulting in a smaller lattice constant. Also, the calculation corresponds to zero temperature while experiment is done at room temperature. Note, however, that the generalized gradient approximation (GGA) often matches better with experimental lattice constants than LDA, but LDA gives a better description of phonons in hafnia [50].

Table 3.1. Structural parameters of monoclinic HfO₂. Th. = theoretical, Exp. = experimental.

a (Å)	b (Å)	c (Å)	β (deg)	From
5.029	5.132	5.183	99.48	Th. [57]
5.106	5.165	5.281	99.35	Th. [50]
5.116	5.172	5.295	99.18	Exp. [43]
5.119	5.169	5.29	99.25	Exp. [44]
5.117	5.172	5.284	99.37	Exp. [45]
5.025	5.118	5.192	99.52	Present Theory

In Figure 3.1(a) we show the phonon spectrum of monoclinic hafnia computed including only the short range contribution to the dynamical matrix (blue line). It has been shown that the long range influence on phonon spectra is not large so we only consider the short range [57]. The BZ path of the calculation starts and ends at the $\Gamma(0, 0, 0)$ point, going through B(0, 0, 0.5), A(0.5, 0, 0.5), E(0.5, 0.5, 0.5) and Y(0.5, 0, 0) high symmetry points of the BZ. From group theoretical analysis, the zone-center modes can be decomposed as:

$$\Gamma = \underbrace{9A_g + 9B_g}_{\text{Raman}} + \underbrace{8A_u + 7B_u}_{\text{IR}} + \underbrace{A_u + 2B_u}_{\text{Acoustic}} \quad (7.1)$$

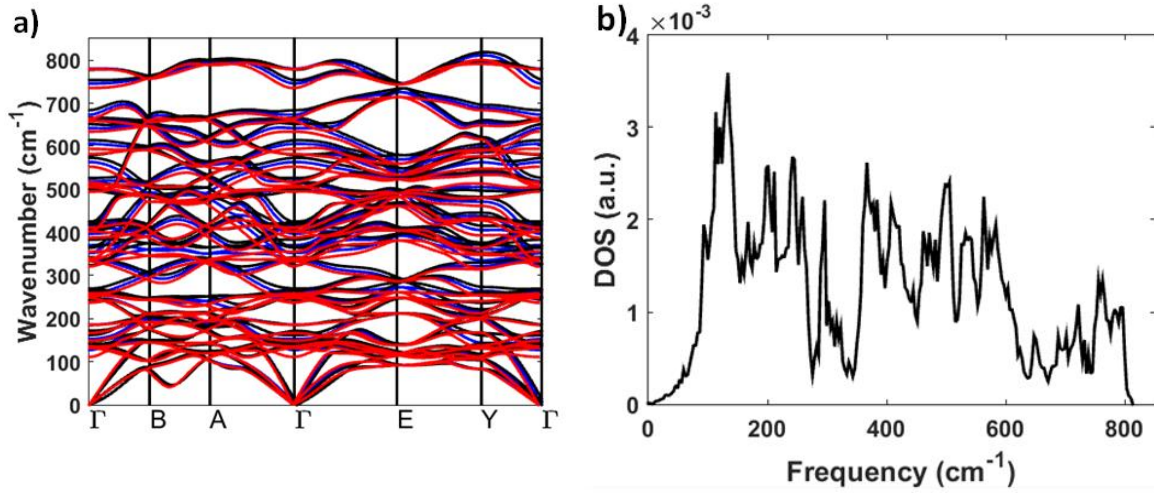


Figure 3.1 (a) Calculated phonon dispersion of monoclinic hafnia. Blue, black and red lines represent no strain, 1% compressive and tensile strain applied to a and c axes case, respectively. (b) Phonon density of states for no strain case.

The phonon density of states is plotted as Figure 3.1(b). We can see a quasi-gap around 350 cm^{-1} which divides the spectrum into low frequency part and high frequency part. As pointed out in Ref. [57], low frequency modes involve predominantly metal atoms while high frequency modes are associated with movement of oxygen atoms. Among these low frequency modes, however, some are still anomalous, as along with hafnium, oxygen ions also exhibit large displacements. We illustrate the eigenvector corresponding to the lowest frequency Raman-active mode at 127 cm^{-1} in Figure 3.2. In this mode the threefold-coordinated oxygen atoms (marked by red) show the most significant displacement, while displacements of hafnium atoms are only half of that. The fourfold-coordinated oxygen atoms (magenta colored) practically do not move.

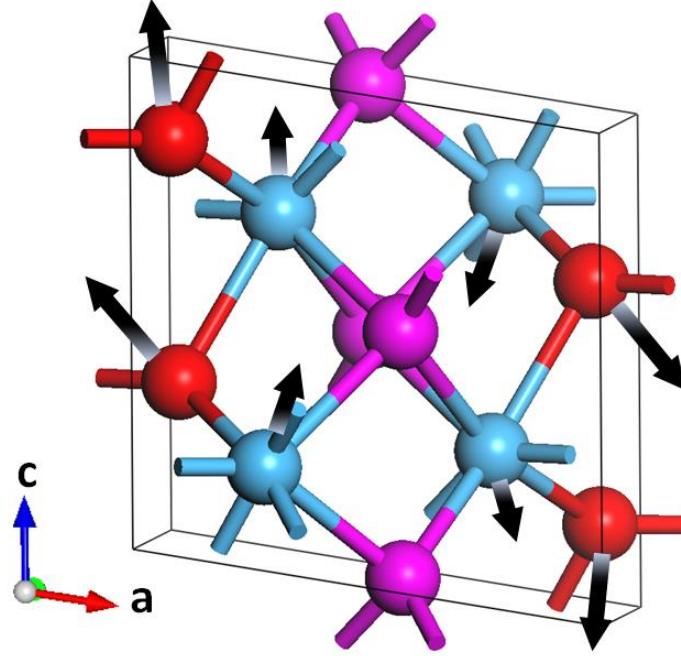


Figure 3.2 Relative atomic displacements of the lowest Raman mode. Arrows denote the direction of the movement at each atom and the length is proportional to displacement amplitude. Monoclinic angle is between a and c axes. Bonds are also plotted to show different coordinations of O atom. 3-folded O atoms are marked by red and 4-folded O atoms are marked by magenta.

In Table 3.2, we list the frequencies of the Raman-active modes obtained in our calculation along with two sets of previous experimental results. Agreement between the calculation and experiments is very good.

Table 3.2. Calculated Raman frequencies (in cm^{-1}) for monoclinic HfO_2 and available experimental data. Th. = theoretical, Exp. = experimental.

A_g	Th. [57]	Th. [50]	Exp. [51]	Exp. [60]	Present Work	B_g	Th. [57]	Th. [50]	Exp. [51]	Exp. [60]	Present Theory
1	133	128	112	113	127	1	136	131	133	133	135
2	140	142	135	133	138	2	171	175	167	164	169
3	153	152	150	149	153	3	246	250	243	242	250
4	257	261	257	256	260	4	339	380	335	336	339
5	361	326	322	323	352	5	421	424	397	398	414

Table 3.2 continued

6	410	423	381	382	397	6	537	533	522	520	516
7	512	514	498	498	498	7	578	570	550	551	564
8	601	608	581	577	581	8	663	667	642	640	642
9	696	738	674	672	663	9	785	821	776	872	780

3.4 INFLUENCE OF STRAIN

In the monoclinic phase of hafnia, the three crystallographic axes are not orthogonal to each other. Here, we model the case when the out-of-plane direction of the film is along the \mathbf{b} axis, and in-plane biaxial strain is applied to \mathbf{a} and \mathbf{c} axes. Strain is fixed to be 1% and both the tensile and compressive strains are considered. The lattice constants in the \mathbf{ac} plane are changed by 1% of original value, while the monoclinic angle is fixed. We optimize the \mathbf{b} lattice constant, letting the ions move freely until the ionic forces are less than 10^{-4} eV/Å. The corresponding change of \mathbf{b} lattice constant is $0.75 \pm 0.01\%$, which means the Poisson ratio is 0.75. From the elastic energy theory, with a biaxial strain applied to \mathbf{a} and \mathbf{c} axes, Poisson ratio $\nu = -\frac{\varepsilon_b}{\varepsilon_a}$ could be expressed as $\frac{C_{12}+C_{23}}{C_{22}}$, where C stands for elastic constants. From our calculation, C_{12} , C_{23} and C_{22} are 489 GPa, 180 GPa and 201 GPa, respectively. Following this, Poisson ratio ν is calculated as 0.78, very close to what we get from relaxation. For comparison, by taking elastic constants from [86,87], the Poisson ratio ν is calculated to be 0.82 and 0.88, respectively. The phonon spectrum is then calculated as previously described.

The effect of strain on the phonon spectrum is shown in Figure 3.1(a). The average of frequencies of three acoustic modes at the Γ point is 0.06 cm^{-1} , we use this as an error estimate of the calculation. The main conclusion is that 1% strain applied to \mathbf{a} and \mathbf{c} axes does not significantly change the phonon spectrum. Compressive strain shifts all modes up in frequency while tensile strain does exactly the opposite. This is an

expected result considering the overall shape of interatomic potentials. We list the frequencies of the main Raman active modes in Table 3.3.

Table 3.3. Calculated Raman frequencies of monoclinic hafnia (in cm⁻¹) in four different cases: without strain, with 1% in-plane biaxial compressive and tensile strain applied to *a* and *c* axes, and strain applied on sample (sample strain). Calculation results are compared with eleven identified Raman peaks in experiment.

mode	no strain	compressive strain	tensile strain	sample strain	measured	% Error
A _g 1	127	137	111	137		
A _g 2	138	147	136	144		
A _g 3	153	162	148	158	150	5.6
A _g 4	260	268	257	267	258	3.4
A _g 5	352	364	337	363		
A _g 6	397	405	388	405	383	5.4
A _g 7	498	499	495	500	498	0.4
A _g 8	581	580	582	588	578	1.9
A _g 9	663	666	659	668	667	0.1
B _g 1	135	138	132	139	135	2.9
B _g 2	169	172	167	171		
B _g 3	250	251	248	251	240	4.4
B _g 4	339	343	333	344	326	5.2
B _g 5	414	419	402	419	399	4.8
B _g 6	516	514	509	515		
B _g 7	564	574	553	575		
B _g 8	642	652	634	655	638	2.6
B _g 9	780	778	779	783		

Experimentally, the film is crystallized at 600 °C first and then cooled down to room temperature. XRD determines the HfO₂ thin film strain based on the known crystal structure. Since the metallic substrate diffracts at larger 2θ, we focus on the diffraction peaks at lower angles, which can be unambiguously attributed to HfO₂. The multiple peaks observed from the out-of-plane XRD data (Figure 3.3), correspond well to the known monoclinic phase of HfO₂. No texture is observed as the relative intensities of the

peaks observed in the measurement correspond well to the powder diffraction [88], demonstrating that the film is polycrystalline in nature. The calculated lattice constants a , b and c for HfO₂ deposited on Pt are measured to be 5.1 ± 0.1 Å, 5.19 ± 0.06 Å and 5.22 ± 0.05 Å respectively, with a tilt angle β of $99.0^\circ \pm 0.2^\circ$. Compared with the experimental bulk values in Table 3.1, a and c axes are under compressive strain while the b axis is strained slightly. This is not unexpected as the material is deposited amorphous and becomes polycrystalline upon annealing.

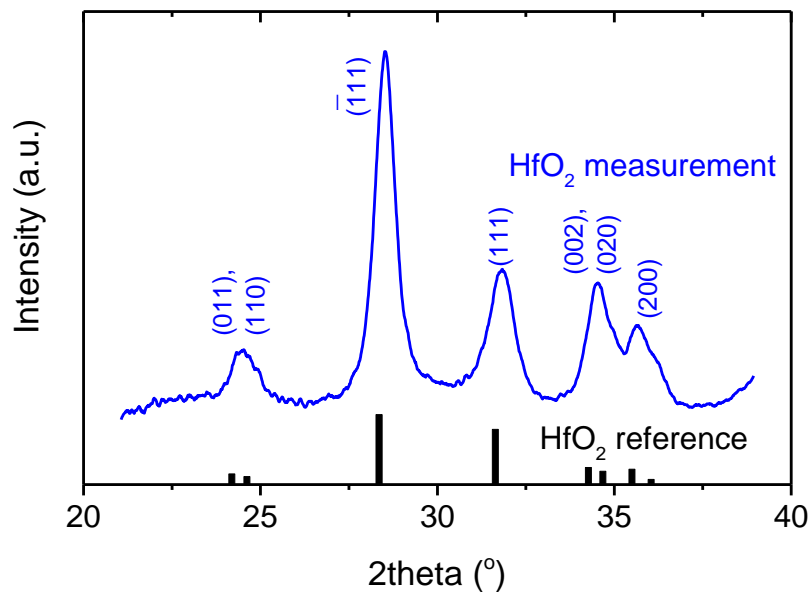


Figure 3.3 X-ray diffraction scan of sputtered hafnia on a platinum substrate, measured at a grazing incidence (1°). The scan demonstrates that polycrystalline monoclinic hafnia is formed after annealing.

Figure 3.4(a) displays the Raman spectra of the HfO₂ deposited on Pt, measured using a 532 nm laser. The Lorentzian fit to the HfO₂ on Pt spectrum is also shown in Figure 3.4(a), offset vertically for clarity. Measurements using 633 nm laser were showing the same spectra. In order to have a fair comparison, we strain the simulation

cell the same way as is measured experimentally, and compute Raman frequencies, which are listed in Table 3.3. The result is very similar to that obtained for the compressively strained material. This is expected, as both a and c axes are under compressive strain. Eleven out of the eighteen calculated Raman modes are identified in the measured spectrum. Fitted peak positions are summarized in Table 3.3 and compared against the calculated peaks for the case of a cell having the strain measured experimentally. We note that calculations were carried out at zero temperature, whereas the measurement was done at room temperature. No measureable peak shifts were observed following an additional annealing step in Ar ambient at 600 °C for 2 hours, suggesting that the main Raman modes in HfO₂ are insensitive to minor changes in the film stoichiometry, unlike TaO_x [89] and SrTiO₃ [76]. Previous studies have shown that annealing SrTiO₃ in reducing ambient results in the appearance of forbidden first order Raman peaks and features associated with oxygen vacancies [33]. Similarly, the Raman spectra of sputtered TaO_x films were showing clear dependence on x by varying the oxygen pressure during the sputtering process [89].

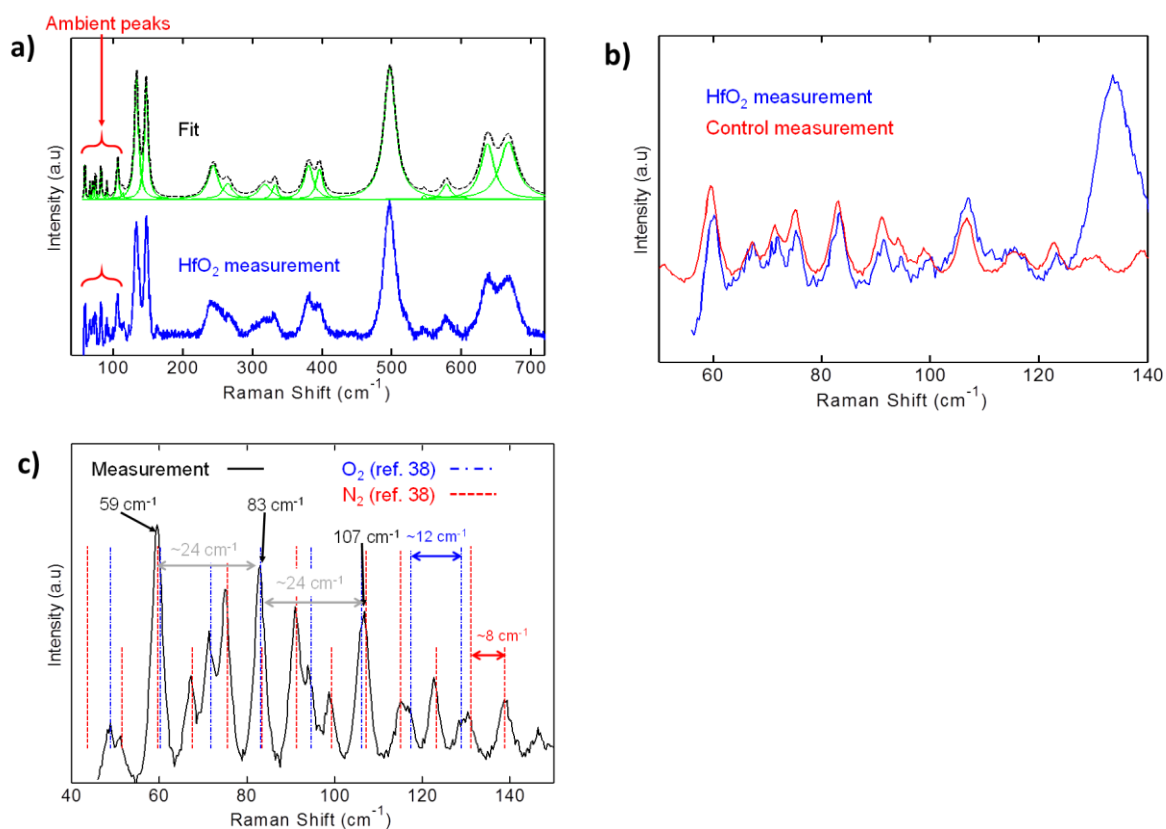


Figure 3.4 Experimental Raman spectra of HfO₂. (a) Bottom: measured Raman spectra of 50 nm HfO₂ on Pt using 532 nm laser (blue) and top: Lorentzian fit (green – for each peak, black – sum over all Lorentzians). Spectra are vertically offset for clarity. The HfO₂ was heated to 600 °C, then cooled to room temperature, forming a polycrystalline monoclinic phase. (See Figure 3.3) (b) Low wavenumber range: measured HfO₂ (blue, same as in a) vs. control experiment without sample and without objective in the laser path (red) showing similar features below 120 cm⁻¹. (c) Control measurement of the low wavenumber Raman spectrum (same as red curve in (b), measured data in black solid line) compared with rotational Raman modes of N₂ (red dashed) and O₂ (blue dash-dot). The low wavenumber modes at 59, 83, and 107 cm⁻¹ are clearly observed in the Raman spectra of the thin HfO₂ sample (marked “ambient peaks” in (a)) and are of comparable intensity due to the weak Raman response of the HfO₂ and the enhanced Raman signal of the rotational modes, where N₂ and O₂ modes overlap.

Interestingly, some features appear in the measured Raman spectra of our HfO₂ films below 110 cm⁻¹. In particular, Raman modes at ~59 cm⁻¹ ~83 cm⁻¹ and ~107 cm⁻¹ consistently appear across different measurements on different substrates. The ~82 cm⁻¹ Raman line was also reported by Quintard *et al.* [52] who interpreted this line as fundamental, even though bulk unstrained HfO₂ does not have any modes at that low a wavenumber. Low wavenumber peak in the range 105-108 cm⁻¹ was also reported by Refs. [17–19].

According to our theoretical results, the strain found in our sample is not capable of causing a frequency downshift of that magnitude. We further investigated experimentally the weak Raman lines below 110 cm⁻¹ as shown in Figure 3.4(b,c). We carried out a control experiment at high laser power (20 mW) and long accumulation (15 min.) without sample and objective in the laser path. We found the same low wavenumber peaks, namely at ~59, 83 and 107 cm⁻¹ and few other smaller features [Figure 3.4(b)]. We attribute these low wavenumber modes to rotational Raman modes of the oxygen and nitrogen molecules present in air ambient as discussed below. We note that the presence of these “ambient peaks” does not exclude the possibility of having fundamental HfO₂ modes in that range (as reported in [17,18]), however measurements carried out in air ambient cannot detect such modes.

Figure 3.4(c) shows very good agreement between the low wavenumber features found in our control measurement and reported rotational Raman modes of N₂ and O₂ from literature [38,39]. In particular, the modes at ~59 cm⁻¹ ~83 cm⁻¹ and ~107 cm⁻¹ are enhanced due to overlap between the O₂ and N₂ modes. It is evident from Figure 3.4(a) that the same peaks (marked as “ambient peaks”) are of comparable intensity to the fundamental HfO₂ peaks. This is an important note to any Raman measurement carried out in air of a material having low absorption and crystallinity, such that the Raman

signal of the ambient may become comparable to the signal of the sample. Here, the periodic features at low wavenumbers ($\Delta\omega \approx 24 \text{ cm}^{-1}$ for the 3 peaks outlined above) are a hallmark of *rotational* Raman modes. The vibrational Raman modes of these gases present in air are located at much higher wavenumbers, but their rotational modes are spectrally located at the low wavenumber range measured here. Figure 3.4(c) shows that the specific modes which are comparable to the HfO_2 signal correspond to overlap between N_2 and O_2 modes, where the N_2 modes have a periodicity of $\sim 8 \text{ cm}^{-1}$ and the O_2 have a periodicity of $\sim 12 \text{ cm}^{-1}$ resulting in the enhanced Raman features with a periodicity of $\sim 24 \text{ cm}^{-1}$.

3.5 THE ROLE OF OXYGEN VACANCIES

Thin HfO_2 films are often non-stoichiometric, and the most prevalent defect is oxygen vacancies. In monoclinic hafnia, there are two non-equivalent oxygen sites: (i) threefold-coordinated oxygen O_3 , bonded with the nearest-neighbor Hf atoms in an almost planar configuration; and (ii) fourfold-coordinated oxygen O_4 , bonded with its Hf neighbors in a distorted tetrahedral configuration. This means that one can have two different types of oxygen vacancies [40,41]. Also, since the formation energies for neutral O_3 and O_4 vacancies are very close (9.36 eV and 9.34 eV, respectively [40]), it is worth investigating the effect of both vacancy types on the phonon spectrum. For ease of comparison, we also compute zone-center frequencies in pure hafnia, in the same $2 \times 2 \times 2$ supercell. For pure hafnia, there are 288 modes in a 96 atom cell. However, all Γ -point frequencies are related to those computed for the primitive cell by a corresponding reciprocal lattice vector. As we double the lattice parameters, the new BZ becomes twice as small and the high symmetry points of the primitive are translated back to the Γ -point [Figure 3.5(a)]. Therefore, the zone-center frequencies of this calculation

are the frequencies from the eight high symmetry points of the primitive cell: $(0, 0, 0)$, $(0.5, 0, 0)$, $(0, 0.5, 0)$, $(0, 0, 0.5)$, $(0.5, 0.5, 0)$, $(0, 0.5, 0.5)$, $(0.5, 0, 0.5)$, $(0.5, 0.5, 0.5)$. We illustrate how the hafnia phonon spectrum “folds” along the direction from the high symmetry point Γ to E in Figure 3.5(b) (up to 200 cm^{-1}). Blue and red lines represent the phonon spectrum in the primitive cell and in the supercell, respectively. The green arrows show how the original spectrum is translated back to the new first BZ.

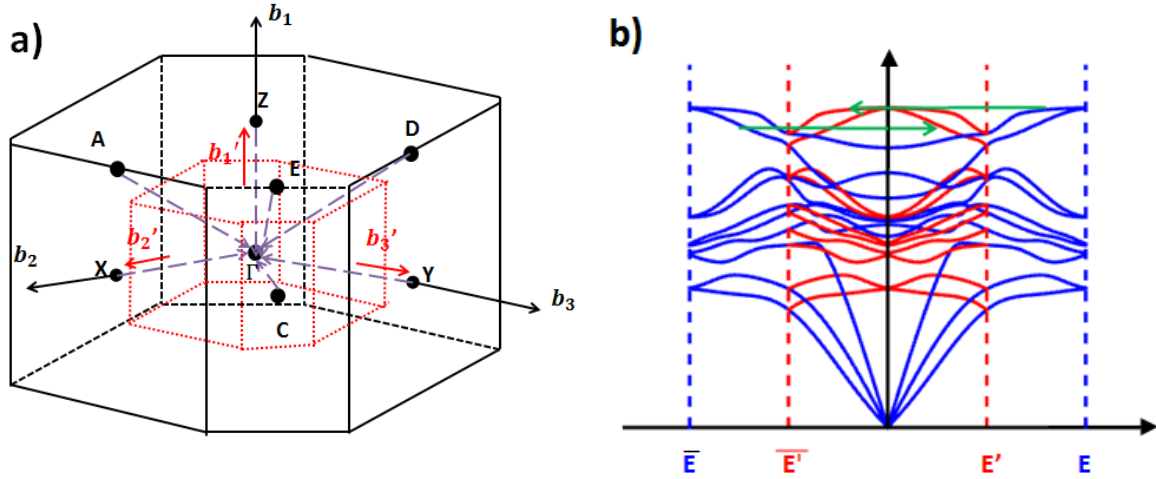


Figure 3.5 (a) The first Brillouin zone (FBZ) of the conventional monoclinic (MCL) lattice. Under this convention, $(0.5, 0, 0)$, $(0, 0.5, 0)$, $(0, 0, 0.5)$, $(0.5, 0.5, 0)$, $(0, 0.5, 0.5)$, $(0.5, 0, 0.5)$, $(0.5, 0.5, 0.5)$ are the Z, X, Y, A, C, D, E points in the figure. Black lines represent the FBZ of the primitive cell while the red lines denote the FBZ of the doubled supercell. The primitive cell and supercell reciprocal lattice vectors \mathbf{b}_i and \mathbf{b}'_i are also shown with black and red arrows, respectively, and $\mathbf{b}'_i = \frac{1}{2}\mathbf{b}_i$. We can see the high symmetry points in the primitive FBZ can be translated back to the Gamma point by purple vectors, which is the combination of \mathbf{b}'_i . (b) The phonon spectrum folding along the direction from Γ to E .

To establish whether or not a mode is introduced by a vacancy, we compare frequencies computed for both the vacancy-containing and defect-free cells. For a specific frequency in the spectrum of a cell with a vacancy, if the corresponding mode

with a similar frequency ($\pm 2 \text{ cm}^{-1}$) can be found in the vacancy-free spectrum, then this mode is thought to be a bulk mode and the small shift in frequency is the result of perturbation introduced by the vacancy. However, if no related bulk modes are found and there is a large gap (10 cm^{-1} or larger) between the frequencies of two cells, then the mode is directly related to the vacancy. We focus on the low frequency modes first (which are metal-dominated). All frequencies below 127 cm^{-1} (the first Raman mode of the primitive cell) for O_3 and O_4 vacancy cells are listed in Table 3.4. The defect-free calculation results are also included for comparison. We can see that in most cases, the differences between the frequencies calculated for these cells are very small ($\pm 2 \text{ cm}^{-1}$). The majority of the modes are only slightly perturbed by the defect. However, for the cell with an O_3 vacancy, a very low frequency mode (see Table 3.4) is found at 96.4 cm^{-1} . It is clearly distinct from the nearby bulk modes at 93.8 cm^{-1} and 103.2 cm^{-1} . Note that only the short range effects are captured, as we do not include the long range correction to the dynamical matrix. This however, is not very rigorous and to obtain the quantitative description and we use the following approach.

Table 3.4. Zone-centered frequencies (in cm^{-1}) below 127 cm^{-1} for pure hafnia supercell case, O_3 and O_4 vacancy cases. The corresponding k-points in the primitive cell are also listed.

k-points in primitive cell	defect-free supercell case	O_3 oxygen vacancy	O_4 oxygen vacancy	k-points in primitive cell	defect-free supercell case	O_3 oxygen vacancy	O_4 oxygen vacancy
(0.5,0,0)	83.0	81.3	82.6	(0.5,0,0.5)	107.1	106.3	106.3
(0,0,0.5)	84.5	83.2	82.9	(0.5,0,0.5)	107.1	108.2	106.8
(0,0,0.5)	84.5	83.9	84.1	(0,0.5,0)	111.2	110.4	109.2
(0.5,0.5,0.5)	92.3	90.2	90.2	(0,0.5,0)	111.2	112.4	110.9
(0.5,0.5,0.5)	92.3	91.5	90.6	(0.5,0,0)	112.9	112.7	111.3
(0.5,0.5,0)	93.5	92.4	92.3	(0.5,0.5,0)	113.8	113.3	112.6

Table 3.4 continued

(0.5,0.5,0)	93.5	92.8	92.9	(0.5,0.5,0)	113.8	114.3	113.1
(0,0.5,0)	93.8	93.1	93.3	(0.5,0,0)	114.7	114.8	114.0
(0,0.5,0)	93.8	93.6	93.8	(0.5,0.5,0. 5)	115.8	115.3	115.1
(0,0,0.5)	103.2	101.2	101.7	(0.5,0.5,0. 5)	115.8	117.1	115.7
(0,0,0.5)	103.2	102.9	103.1	(0.5,0.5,0. 5)	120.8	119.7	119.3
(0.5,0,0)	105.7	105.2	104.3	(0.5,0.5,0. 5)	120.8	120.9	120.5
(0,0.5,0.5)	106.3	105.9	105.0	(0.5,0,0.5)	122.5	121.5	121.1
(0,0.5,0.5)	106.3	106.3	105.4	(0.5,0,0.5)	122.5	123.5	122.0
(0.5,0,0)	83.0	81.3	82.6	(0.5,0,0.5)	107.1	106.3	106.3

A more accurate way to identify the vacancy-related modes is by calculating the inner product between the eigenvectors of a vacancy-containing cell with those of a defect-free cell. We use $\Phi_\alpha(q)$, where $\alpha = 1, 2 \dots 288$ to represent 288 phonon modes at the Γ point of a 96-atom, defect-free cell. Every eigenvector has 288 components $u_\alpha^i(q)$ corresponding to $3 \times N$ degrees of freedom. Similarly, in a vacancy cell, 285 phonon modes at the Γ point are recorded as $\Phi'_\alpha(q)$, where $\alpha = 1, 2 \dots 285$ and they have 285 components $u_\alpha^i(q)$. Since the eigenvector of a vacancy cell has 3 fewer components, we set them to zero. We calculate the inner product between $\Phi'_\alpha(q)$ and $\Phi_\beta(q)$ and define a distribution function $f_\alpha(\beta) = \langle \Phi'_\alpha(q) | \Phi_\beta(q) \rangle^2$ for $\Phi'_\alpha(q)$. If the distribution is close to a delta function $\delta_{\alpha\beta}$, that indicates $\Phi'_\alpha(q)$ is similar to a bulk-like mode. If, on the other hand, the distribution is broad, that manifests the mode could not be simply represented by a single, bulk-like mode but is related to a vacancy. Overall $\sum_{\beta=1}^{288} f_\alpha(\beta) = 1$. In Figure 3.6(a) and Figure 3.6(b), we use 3D plots to show $f_\alpha(\beta)$ for O_3 and O_4 vacancy cells, respectively. We find that for the O_4 -based vacancy case, most of vacancy-related modes appear in the high frequency region of the spectrum, while for the O_3 -based vacancy case, the modes are distributed more evenly. We

calculate $g_\alpha = \max_\beta (f_\alpha(\beta)^{-1})$ for all $\Phi_\alpha'(q)$ in both O₃ and O₄ vacancy cells as shown in Figure 3.6(c) and 6(d). A large g_α corresponds to a broad distribution while a small $g_\alpha(\sim 1)$ corresponds to a narrow distribution. We use 4 as a cutoff value for g_α . Combing these two methods, all vacancy-related frequencies are listed in Table V and Table VI for O₃ and O₄ vacancies, respectively.

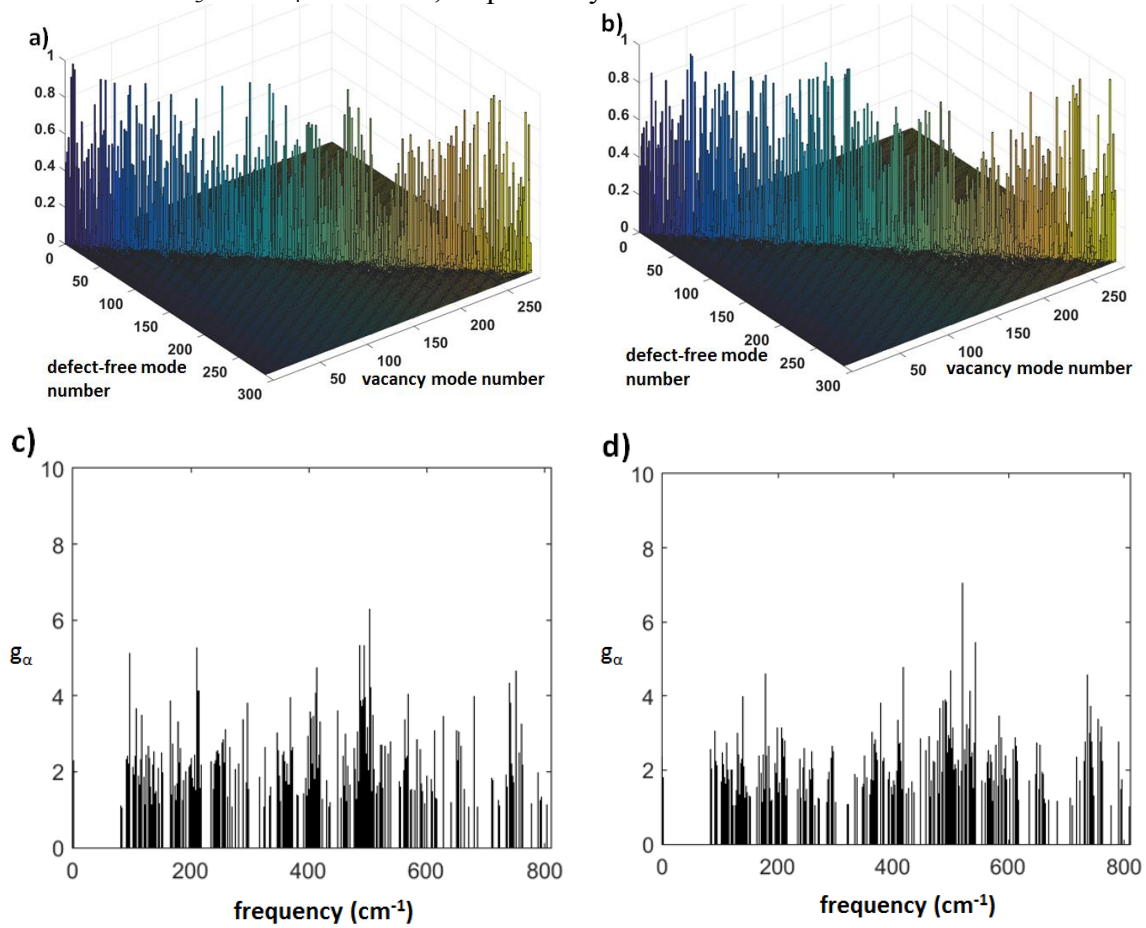


Figure 3.6 (a) Distribution of square of the inner product $f_\alpha(\beta)$ in O₃ vacancy cell. (b) Distribution of square of the inner product $f_\alpha(\beta)$ in O₄ vacancy cell. (c) g_α for vacancy-related modes in O₃ vacancy cell. (d) g_α for vacancy-related modes in O₄ vacancy cell.

To characterize the degree of localization of the vacancy-related modes quantitatively, we calculate the inverse participation ratio (IPR) for all the modes listed in Table 3.5 and Table 3.6. The IPR is defined as $P_k^{-1} = \sum_N (\sum_{\alpha=1}^3 u_{i\alpha,k}^2)^2$ (note that the eigenvector is normalized), where N is the total number of atoms and α refers to three spatial directions [42]. For the phonon mode where all atoms contribute equally (have the same amplitude), IPR is $1/N$, and in our case it is around 0.01. If there are only m atoms that vibrate in the mode, then IPR is $1/m$. For comparison, we compute IPR values for all Γ -point modes in a defect-free cell. For most of them the IPR is less than 0.03 and the maximum value is less than 0.05. We use this value as a cutoff for identifying localized modes. From Table 3.5 and Table 3.6, we find that modes at 96.4 cm^{-1} , 411.6 cm^{-1} , 680.4 cm^{-1} , 751.2 cm^{-1} and 788.2 cm^{-1} in the O_3 vacancy cell and 476.3 cm^{-1} , 755.6 cm^{-1} in the O_4 vacancy cell have large IPR values, which indicates that a significant vibration is only around a few atoms for these modes.

Table 3.6. Frequencies (in cm^{-1}) of vacancy-related modes in O_4 vacancy cell and corresponding inverse participation ratio (IPR) values. Modes with large IPR values are highlighted.

frequency	IPR	frequency	IPR
178.2	0.038	647.2	0.027
377.6	0.042	647.8	0.024
417.3	0.032	684.6	0.022
476.3	0.06	706.4	0.036
499.2	0.029	731.3	0.031
519.8	0.031	733.0	0.036
533.0	0.028	737.0	0.043
542.4	0.032	755.6	0.051
553.9	0.029	758.8	0.044
634.6	0.033	790.2	0.045

We carefully checked atomic movements of each vacancy-related, high-IPR-value mode and concluded that the 96.4 cm^{-1} mode in the O_3 vacancy cell and 755.6 cm^{-1} mode in the O_4 vacancy cell are localized defect modes, with atomic displacements localized around the defect site. In Figure 3.7(a) and (b), using bar plots we show relative displacement amplitudes in real space for each atom in these two modes ($\frac{1}{\sqrt{m_i}} \sqrt{u_{i,x}^2 + u_{i,y}^2 + u_{i,z}^2}$ where m_i is the atomic mass and u_i is the entry in the eigenvector corresponding to the i -th atom of the basis, with the eigenvector normalized to unity). For the 96.4 cm^{-1} mode, one Hf atom and one O atom move more significantly than others, and we mark these two as black in Figure 3.7(c). We note that the Hf atom is directly bonded to the missing 3-fold oxygen and the other O atom is also very close to a vacancy (2.8 \AA). For the 755.6 cm^{-1} mode, as this is a high frequency mode, all 5 atoms that move most significantly are oxygens. In Figure 3.7(d), except for the blue O atom, which is 4.5 \AA from the vacancy site, all of other 4 black O atoms are close to the vacancy site (distances to vacancy are 2.5 \AA , 2.9 \AA , 2.9 \AA and 3.2 \AA).

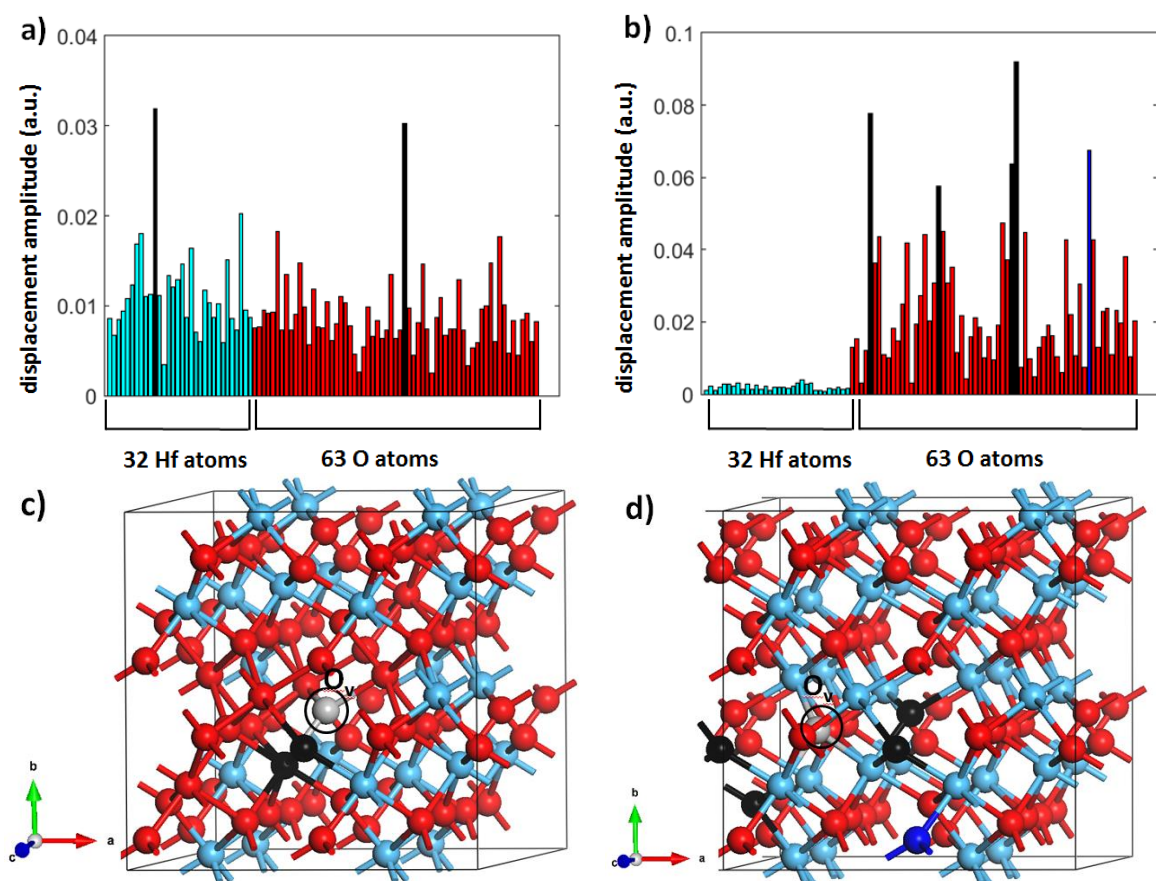


Figure 3.7 (a) Bar plot of the mode. The X axis represents atomic number in the cell and first 32 atoms are Hf atoms, while other 63 atoms are O atoms. Colors of different atoms are selected according to Figure 3.7(c). (b) Bar plot of the mode. Colors of different atoms are selected according to Figure 3.7(d). (c) The simulation cell containing an O3 vacancy. Red balls represent oxygen atoms and cyan balls represent Hf atoms. The O3 vacancy is created by removing the grey atom. Atoms that have significant displacements in 96.4 cm^{-1} mode are highlighted with black. (d) The simulation cell containing an O4 vacancy. The O4 vacancy is created by removing the grey atom. Atoms that have significant displacements in 755.6 cm^{-1} mode are highlighted.

3.6 CONCLUSION

Using density functional theory, we investigated the phonon spectra of HfO_2 in the presence of oxygen vacancies and strain, comparing it against experimental Raman

measurements of thin HfO₂ films. The measured Raman spectra show low wavenumbers features (below 110 cm⁻¹) which we assign to rotational Raman modes of the gases present in air ambient rather than the HfO₂ film. It is found that a 1% in-plane tensile strain to *a* and *c* axes can result in down-shift while a 1% compressive strain can cause the up-shift of the Raman active modes. For the threefold-coordinated oxygen vacancy case, a low frequency metal-dominated 96.4 cm⁻¹ mode, which is 30 cm⁻¹ lower than the first Raman active mode of stoichiometric hafnia, is predicted. For the four-coordinated oxygen vacancy case, a high frequency, oxygen-dominated mode at 755.6 cm⁻¹ is predicted. We reveal these two modes to be highly localized by calculating the inverse participation ratio (IPR) and by analyzing atomic displacements in real space, verifying that they could be introduced by oxygen vacancies.

Chapter 4 *Ab-initio* study of spin-polarized two-dimensional t_{2g} electron gas at EuO/ SrTiO_{3- δ} interface

In this chapter, using first-principles calculations we predict the existence of a spin-polarized two-dimensional electron gas at the interface of a ferromagnetic insulator EuO and oxygen-deficient SrTiO₃. The carriers are generated by oxygen vacancies in SrTiO₃ near the interface and have predominantly Ti- t_{2g} orbital character. At the interface, the split-off d_{xy} -derived conduction band of SrTiO₃ is fully spin-polarized and the in-gap vacancy-induced state, found below the conduction band edge, is aligned ferromagnetically with EuO. The calculations suggest a possible mechanism for generating spin-polarized 2DEG for spintronic applications. Results have been published as Lingyuan Gao, Alexander A. Demkov, Phys. Rev. B. **97**, 125305 (2018).

4.1 INTRODUCTION

With a rapidly growing interest in transition metal oxides, perovskite SrTiO₃ (STO) stands out as a substrate of choice in oxide epitaxy, and for the important role it plays among the oxide heterojunctions and interfaces. The best known example is arguably the LaAlO₃/SrTiO₃ interface. Though comprised of two wide-band-gap insulators it shows a two-dimensional electron gas (2DEG) [92,93] that exhibits a host of intriguing phenomena, including magnetism [94] and superconductivity [95], as well as their coexistence [96,97]. After a decade-long research effort, the mechanism behind the 2DEG formation at this interface is still under debate. The “intrinsic” one (the so-called “polar catastrophe” [98]) refers to electron transfer from the polar oxide (LaAlO₃) surface to the interface. While the “extrinsic” mechanism points to oxygen vacancies [99,100] that are one of the most common doping defects during the film growth in ultra-high vacuum and to interface cation exchange [101–103]. The purely

vacancy-related 2DEG has been observed at the interface of STO and γ -Al₂O₃ [104,105]. And 2DEG is also observed at the bare STO (001) surface, where it is attributed to oxygen vacancies [106,107]. Interestingly, in this case, along with the 2DEG, an in-gap state is observed 1.3 eV below the Fermi level by an angle-integrated photoemission measurement [107]. On the other hand, an in-gap level 2.7 eV above the valence band edge is observed for the SrO-terminated surface with scanning tunneling spectroscopy [108]. The controversial role of oxygen vacancies in STO has drawn much attention and has been investigated using density functional theory (DFT) [109–114]. Recently, the Anderson impurity model [115] and DFT plus dynamical-mean field theory (DMFT) [116] applied to an O_v reached qualitative agreement with each other and experiment, suggesting that itinerant t_{2g} -derived states do coexist with a localized in-gap e_g -derived state in bulk oxygen-deficient SrTiO₃.

EuO is a ferromagnetic semiconductor with the Curie temperature T_c of 69 K [117]. The large magnetic moment of 7 μ_B on Eu ions originates from the half-filled $4f$ states and causes a large spin-split of the conduction $5d$ band of 0.6 eV [118]. Spin-polarized 2DEG in the Eu $5d$ band has been predicted at the LaAlO₃/EuO interface [119,120]. Due to this spin polarization, EuO has potential applications in spin-filter tunneling junctions [121,122]. Theoretically, EuO has been proposed to induce ferromagnetic ordering in graphene and transition-metal dichalcogenide monolayers by the proximity effect that could open a 36 meV exchange-splitting gap in graphene, and lift the valley degeneracy and create a giant valley splitting (over 300 meV) in MoTe₂ [123,124]. Recent reports discuss successful growth of graphene on EuO [125,126], making this an intriguing possibility.

Posadas *et al.*, have discussed the ability of many metals to scavenge oxygen from STO at high temperatures [127]. Eu has been demonstrated to form epitaxial EuO layers

on STO when deposited in UHV at 300°C, leaving an oxygen deficient layer of STO below the interface. This opens an intriguing possibility. In this chapter, using first-principles theory at the DFT+U level, we propose an alternative approach to creating spin-polarized 2DEG at the interface of oxygen-deficient STO and EuO. The carriers are generated by the oxygen vacancies on the STO side, similar to what is found at the $\text{Al}_2\text{O}_3/\text{STO}$ interface [104,105] rather than by the polar field in the case of LaAlO_3 [23]. Also, unlike the previous work, here the carriers would reside not in the Eu $5d$ states but mostly in Ti-derived t_{2g} states of STO, and polarization is induced via a proximity effect due to EuO. An e_g in-gap O_v -induced state found below the conduction band edge is singly occupied and aligned ferromagnetically with Eu.

4.2 COMPUTATIONAL METHOD

We perform DFT calculations within the generalized gradient approximation (GGA) [22] and projected augmented wave pseudopotentials [28], using Vienna Ab-Initio Simulation Package [31]. For Sr, Ti, Eu and O, $4s^24p^65s^2$, $3s^23p^64s^23d^2$, $5s^25p^64f^76s^2$ and $2s^22p^4$ are included, respectively. To properly describe the Eu $4f$ orbitals, the GGA+U approach [23,24] is employed with an empirical value of $U_f = 5.0$ eV. We use a 17-electron configuration for Eu ($4f$ orbitals are not frozen in the core). The calculated EuO lattice constant of 5.164 Å agrees well with the experimental value of 5.144 Å. To include electron correlation in $\text{SrTiO}_{3-\delta}$, a combination of $U_d = 5.0$ eV and $J_d = 0.64$ eV is used for the Ti $3d$ orbitals [128]. The calculated bulk lattice constant of STO is 3.948 Å. This overestimates slightly the experiment value of 3.905 Å as typical for GGA. The calculated 2.4 eV band gap is still smaller than the experimental value of 3.2 eV; nevertheless, these parameters provide a reasonable description of an oxygen vacancy in

STO [109–111,129,130]. As will be discussed later, the U value for Eu does not affect the present results significantly, while that for Ti indeed requires a careful consideration. To model the epitaxial SrTiO_{3- δ} /EuO (001) structure, we employ periodically repeated symmetric slabs (EuO)₃/TiO₂-(SrO-TiO₂)₆/(EuO)₃ separated by a thick vacuum region (in excess of 20Å). As for the in-plane geometry, the rock salt EuO cell is rotated by 45° to match the perovskite that is understood as being a substrate. This results in an 8.5% tensile strain in EuO. In previous reports, it has been suggested that a tensile strain may induce an in-plane ferroelectricity in EuO [131,132]. We note 8.5% tensile strain of the EuO thin film is quite large. However, we have some experimental evidence showing that despite high strain, the EuO/STO heterostructure is stable. As shown in the high-angle annular-dark-field image in Figure 4.1, the bottom part of the image is STO and the top is rock salt EuO. The film is epitaxial at least for a few layers. EELS mapping (Ti L-edge analysis) reveals oxygen defects (vacancies) in a few STO layers close to the interface. We just want to assure the reviewer that this is not an entirely frivolous calculation. The reader interested in the effects of strain in oxide epitaxy is referred to an excellent review by Schlom *et al.* [133]. However, as it is beyond the intended scope of this work, we preserve the in-plane symmetry and only allow oxygen relaxation along the z direction, normal to the interface. To consider the role of oxygen vacancies in STO, we employ a 2×2 STO supercell (Figure 4.2(b)), where a single vacancy is created. We use 600 eV as the plane-wave cutoff energy and sample the Brillouin zone with $4 \times 4 \times 1$ Monkhorst-Pack k -point grids [29]. The entire structure is relaxed until the residual force is smaller than 0.02 eV/Å.

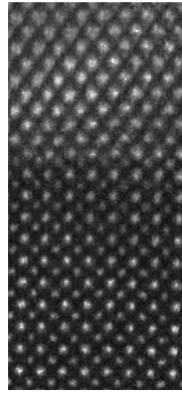


Figure 4.1 High-angle annular dark-field scanning transmission electron microscopy [100] projection image of the EuO/STO interface.

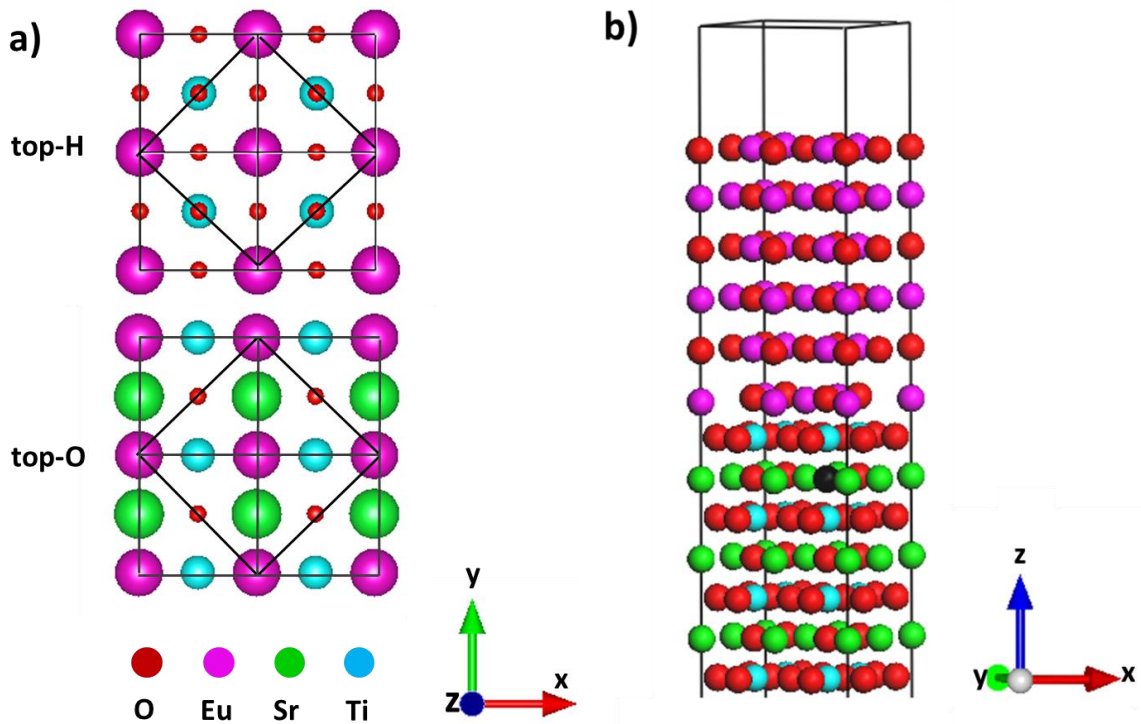


Figure 4.2 The simulation cell of $(\text{EuO})_3/\text{TiO}_2-(\text{SrO-TiO}_2)_6/(\text{EuO})_3$ heterostructure. (a) Top view of two different types of interfaces: Eu on top of a hollow site in a TiO_2 plane (top-H) and on top of an oxygen in a TiO_2 plane (top-O); (b) 2×2 supercell with a single vacancy at the sub-interface SrO plane. Only half of the cell is presented due to mirror symmetry. The oxygen vacancy site is marked in black.

As shown in Figure 4.2(a), there are two obvious possible epitaxial interfaces between EuO and SrTiO₃: (1) Eu is above a hollow site in the TiO₂ plane as a continuation of the Sr sub-lattice (top-H) and (2) Eu is above oxygen in the TiO₂ plane to maintain the Eu-O chain (top-O). As the number of atoms needed to model these interfaces is the same for both types, we can simply compare their total energies in order to decide, which one is more stable. We find the top-H interface to be more stable by 4886 mJ/m², and in the rest of the paper we focus on this structure. An oxygen vacancy can be created in the sub-interface SrO plane as shown in Figure 4.2(b). The vacancy formation energy is estimated to be 5.63 eV, close to 5.66 eV calculated for a stand-alone 2 × 2 × 4 SrTiO₃ supercell. If a vacancy is created in the interfacial TiO₂ plane, the formation energy is 6.37 eV. This suggests that EuO layers have a small influence on the formation of an oxygen vacancy in SrTiO₃. However, the presence of metallic Eu layer would lower the formation energy of a vacancy [127,134].

4.3 ELECTRONIC STRUCTURE AND DISCUSSION

We start our discussion with the (EuO)₃/TiO₂-(SrO-TiO₂)₆/(EuO)₃ heterostructure (top-H) without a vacancy. Figures 4.3(a) and (b) show the density of states (DOS) projected on specific atoms for each layer of this heterostructure. Owing to a mirror-symmetry of the cell, the results for one half of the simulation cell are presented. The system is insulating as expected, since no carriers are introduced. In the EuO layers, the majority-spin Eu *4f* states seen right below the Fermi level (there is a weak hybridization with the oxygen *p* states). This band becomes evanescent in the STO region across the interface. It decays into the STO band gap and disappears at the second TiO₂ layer, 6 Å away from the interface. Also, a EuO surface state right above the top of the oxygen-

derived valence band is clearly seen for both spin channels. This state decays slowly and is even recognized at the interfacial layer due to a modest thickness of the EuO region in our simulation. The minority spin empty Eu $4f$ states are much higher in energy, beyond the energy window in Figure 4.3. On the other hand, the EuO conduction band edge is composed mainly of the spin-up Eu $5d$ states, and demonstrates the spin-splitting of about 0.6 eV, similar to that in bulk ferromagnetic EuO [119]. In STO, the valence band top is oxygen-dominated and is 1.7 eV below the Fermi level (this suggests a 1.7 eV valence band offset between the two oxides). The STO conduction band bottom is 0.6 eV above the *Fermi level*. The corresponding theoretical band gaps of STO and EuO are 2.3 eV and 0.6 eV, respectively.

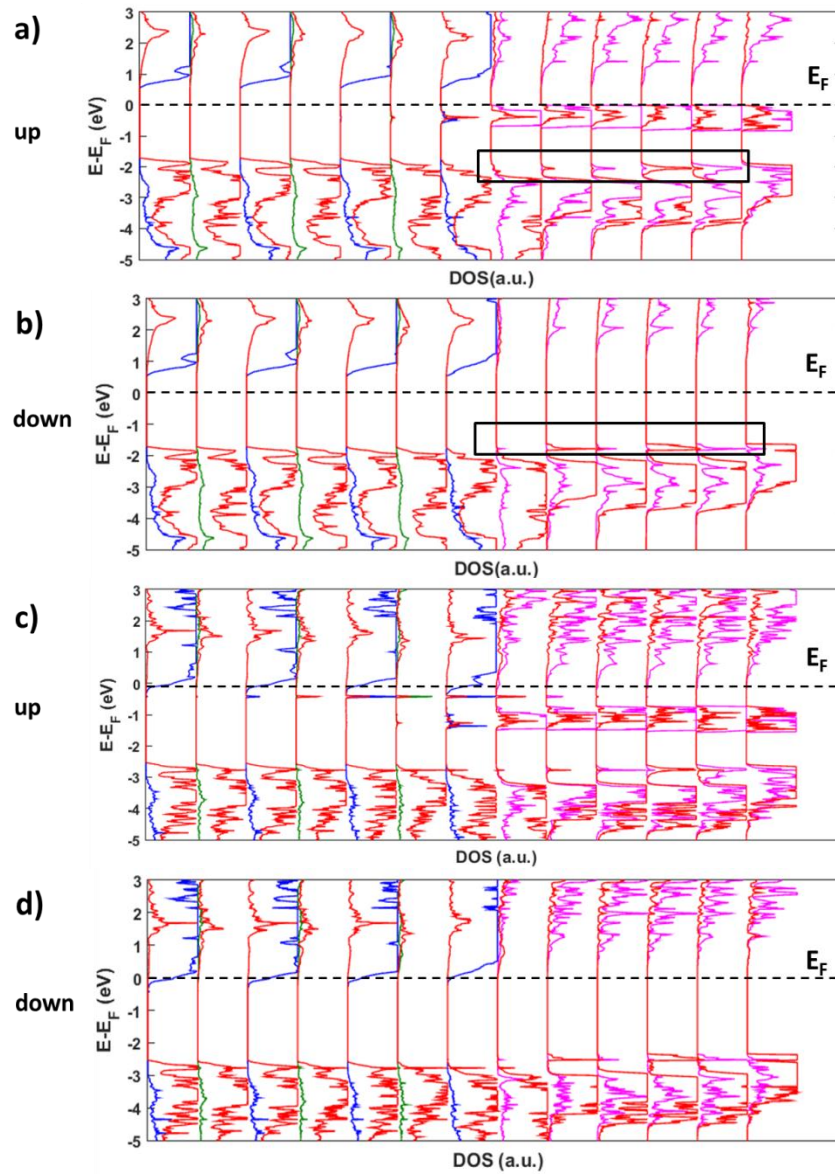


Figure 4.3 Density of states (DOS) projected on a specific atom for each layer in top-H heterostructure without and with a vacancy. Only the results for the upper half cell are shown due to symmetry. Eu, O, Ti, Sr states are marked by magenta, red, dark blue and green, respectively. EuO surface states are indicated with the square. (a) and (c) panels correspond to the spin-up while (b) and (d) correspond to spin-down components, respectively.

We now introduce an oxygen vacancy in the sub-interface SrO plane, as shown in Figures 4.3(c) and (d), and the system becomes metallic. In EuO, the valence band top is shifted down to -0.7 eV relative to the *Fermi level* and the conduction band bottom is also 0.1 eV below the *Fermi level*. In STO, the valence band top is shifted down in energy to -2.5 eV. At the interface, the Ti-derived conduction band bottom is at -0.3 eV while in the other three Ti layers, the conduction band edge is at -0.2 eV (all energies are with respect to the *Fermi level*). We also find that a localized in-gap state is created at the vacancy position in the sub-interface SrO layer. It resides on Ti atoms adjacent to the vacancy site (the interface TiO₂ layer and TiO₂ layer right below the vacancy). One electron is trapped in this in-gap state. As has been discussed by Lin and Demkov, in bulk STO, the vacancy-induced localized state can trap at most one electron, while the second electron occupies the conduction band due to electron-electron repulsion [115]. Also, Hou *et al.* discussed a similar scenario [111]. The result has also been reproduced by Jeschke *et al.* using DFT+U [130], however their calculation was restricted to a nonmagnetic case and required multiple vacancies to be arranged in a specific way. Interestingly, in our case, the in-gap state appears only in the spin-up channel, and is aligned ferromagnetically with the Eu ions above the interface. This in-gap state decays quickly into both the STO and EuO regions on both sides of the interface. In EuO, the evanescent states can be seen two layers away from interface. The decay length is estimated as 7.8 Å and 9.3 Å for SrTiO₃ and EuO, respectively.

The orbital decomposition of the Ti *d* states for each STO layer is shown in Figure 4.4(a). The in-gap vacancy state has mainly a $d_{3z^2-r^2}$ orbital character, mixed with the Ti $4p_z$ and *s* orbitals due to lifting of the local cubic symmetry caused by the vacancy [135]. This increases the spatial extent of Ti orbitals sufficiently far to introduce coupling between the Ti ions adjacent to the vacancy in layers 3 and 4 (interface). At the

interface, the d_{xy} state is shifted down in energy from the other t_{2g} states (d_{xz}/d_{yz}) and is the only one occupied, while in the bulk-like STO region (layer 1), the d_{xz}/d_{yz} states tend to be occupied similarly to d_{xy} . This is similar to the $\text{LaAlO}_3/\text{SrTiO}_3$ system and has been attributed to the symmetry lowering and orbital reconstruction at the interface [136–139]. In addition, for all 4 Ti ions at the interface, the d_{xy} state has a spin-splitting of about 0.3 eV and only the spin-up channel (same spin as Eu and a vacancy level) is occupied resulting in a spin polarized interface channel.

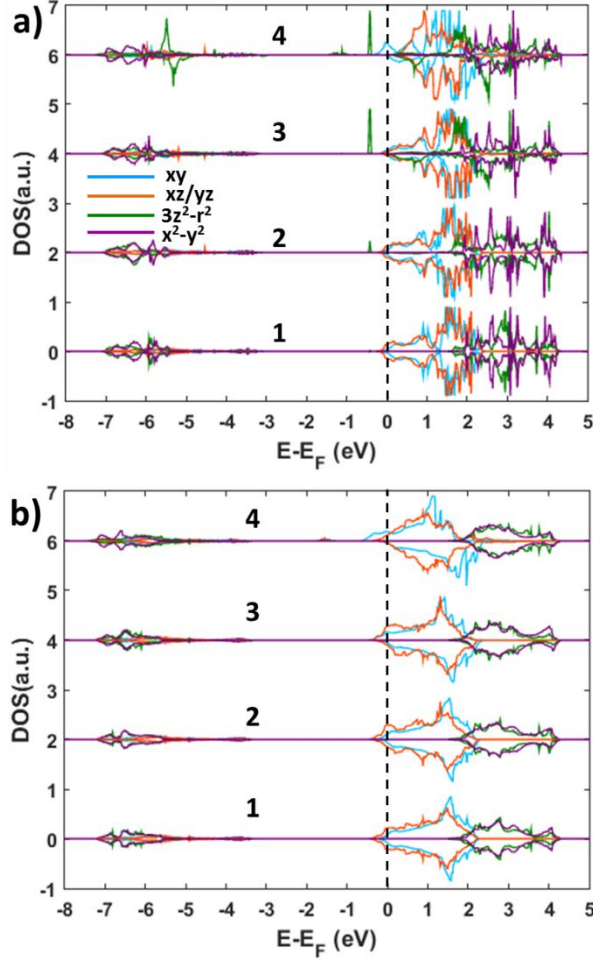


Figure 4.4 DOS projected on the Ti d states in each layer. Layer 1 represents the central “bulk” part of SrTiO₃, while layer 4 represents the interfacial layer. (a) DOS of top-H heterostructure with a vacancy; (b) DOS of top-H heterostructure without vacancies but artificially doped with two extra electrons.

We compute the total number of itinerant carriers (excluding the e_g vacancy state) $n = n^\uparrow + n^\downarrow$ and spin polarization $p = \frac{n^\uparrow - n^\downarrow}{n^\uparrow + n^\downarrow}$ for each layer. Thus computed number of carriers n (per 2x2 STO area) and corresponding spin polarization p from layer 1 to layer 4 are $0.22 e^-$, $0.2 e^-$, $0.13 e^-$, $0.19 e^-$, and 0% , 8.7% , 30.7% and 100% , respectively. We note the way we calculate the number of carriers in each layer is we do the integral for each atomic orbital-projected DOS from the conduction band edge to the Fermi level, and

then we take a sum for all orbitals and all atoms for that layer. Since there are spaces between atoms (spheres used for the projection), after the projection a small fraction of electron is lost (here is about 0.26). On the other hand, if we do the integral using the total DOS (no layer projection), the number is indeed 1. The number of carriers in different layers doesn't change much, while the spin polarization increases significantly when approaching the interface. Note, that the Ti d_{xy} state could carry more electrons compared with the spin-split Eu $5d$ band, the DOS of which is rather low. Therefore, the current regime may have an advantage for generating spin-polarized 2DEG over previously suggested schemes, where doping occurs in the EuO layers [28, 29]. To better understand the origin of the spin-split of the interfacial d_{xy} state, we perform the following computational experiment. We consider the same $(\text{EuO})_3/\text{TiO}_2\text{-(SrO-TiO}_2)_6/(\text{EuO})_3$ heterostructure (top-H) but without vacancies and artificially introduce two extra electrons (a homogeneous compensating background charge is added to maintain the neutrality). The resulting partial DOS projected on the Ti ions is shown in Figure 4.4(b). There are no vacancy-related in-gap states, but we still see spin polarization in the d_{xy} band at the interface. This suggests that interfacial states are influenced by the $7 \mu_B$ magnetization of the neighbouring Eu ions and the spin-polarization of 2DEG is caused by the proximity effect (superexchange).

4.4 THE EFFECT OF ON-SITE COULOMB REPULSION U

As we use the on-site Coulomb repulsion U on both Eu $4f$ states and Ti $3d$ states, the theory is not completely ab-initio. And it is important to understand the influence of these semi-empirical parameters on the results of the calculations. Within the DFT+ U formalism, the orbital energy ε_i' could be written as $\varepsilon_i' = \varepsilon_i + U(\frac{1}{2} - n_i)$, where ε_i is

the orbital energy of the regular LDA/GGA functional, U is the Coulomb repulsion and n_i is the orbital occupation [24]. Since the spin-up Eu $4f$ states form the valence band, increasing the Eu U value would shift the occupied spin-up $4f$ states down and the $f-d$ band gap would increase accordingly. This agrees well with the calculation; for a Eu U value of 5.0 eV, the band gap is 0.6 eV, and the valence band offset between the Eu $4f$ states and O p states of STO is 1.7 eV. While with a Eu U value of 8.0 eV, the band gap of EuO is 1.2 eV and the valence band offset decreases to 1.1 eV. Apart from that, the band structure doesn't change significantly, including the EuO conduction band edge comprised of Eu $5d$ states.

However, when we vary the Ti U value, the effect is quite different: Figure 4.5 shows the DOS projected onto each atomic layer in top-H heterostructure with vacancy while using Ti $U = 8$ eV. The in-gap state now is completely filled by two electrons from the vacancy and there are no itinerant electrons. Also, instead of being ferromagnetic as in the case of $U = 5$ eV, the spins on two Ti ions adjacent to the vacancy prefer the antiferromagnetic arrangement. For Ti ion close to the interface, the spin is aligned ferromagnetically with the Eu ion.

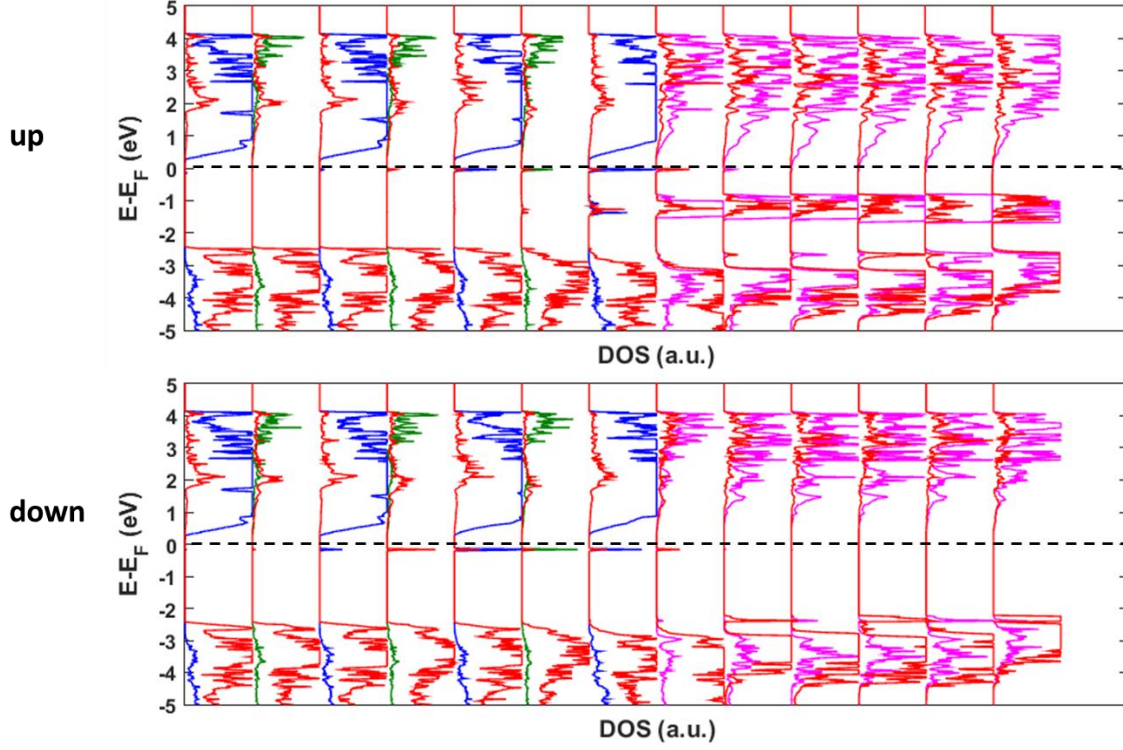


Figure 4.5 Similar to Figure 4.2, the atom-projected DOS for each layer in the heterostructure containing a vacancy with $U_{\text{Ti-d}} = 8$ eV.

To explain this result, we use a three-orbital model following Lin *et al.*'s [115]:

$$\begin{aligned}
 H = \varepsilon_1 \sum_{\sigma=\uparrow,\downarrow} (n_{1\sigma} + n_{2\sigma}) - g\mu_B H \sum_{i=1,2} (n_{i\uparrow} - n_{i\downarrow}) - t \sum_{\sigma=\uparrow,\downarrow} c_{1\sigma}^+ c_{2\sigma} - t \sum_{\sigma=\uparrow,\downarrow} c_{1\sigma} c_{2\sigma}^+ \\
 + U \sum_{i=1,2} n_{i\uparrow} n_{i\downarrow} + \varepsilon_0 \sum_{\sigma=\uparrow,\downarrow} n_{0\sigma} - g\mu_B H (n_{0\uparrow} - n_{0\downarrow}). \quad (4.1)
 \end{aligned}$$

Here, 0 represents the uncorrelated bath orbital with energy ε_0 (for convenience we set ε_0 to 0). Indices 1 and 2 refer to two Ti $d_{3z^2-r^2}$ -based localized orbitals with energy ε_1 , which are adjacent to vacancy. The hopping parameter t describes the coupling between them and the on-site repulsion U is applied to both orbitals. Furthermore, g is the g factor, μ_B is the Bohr magneton and H is the “external” magnetic field coming from Eu ions. As one vacancy provides two electrons, we need to determine two-electron ground state of this Hamiltonian. There are three possibilities for the

ground state: (I) both electrons occupy the itinerant orbital; (II) one electron occupies localized orbital, and the other occupies itinerant orbital; (III) two electrons occupy two localized orbitals. For phase (I), the lowest energy E_I is 0. For phase (II), the lowest energy E_{II} is $\varepsilon_1 - 2g\mu_B H - t$. In the lowest energy configuration, spins of both electrons are aligned along the magnetic field. For phase (III), there are two different lowest energies:

$$E_{III} = 2\varepsilon_1 - g\mu_B H, \quad E'_{III} = 2\varepsilon_1 + \frac{1}{2}\left(U - \sqrt{U^2 + 16t^2}\right), \quad (4.2)$$

E_{III} corresponds to a configuration where each electron occupies one localized orbital and spins are ferromagnetically aligned, parallel to the magnetic field. E'_{III} corresponds to a configuration where the spins of two electrons are antiferromagnetically aligned, which is the singlet for a two-site Hubbard model [140]. In terms of our DFT calculation, “0” represents the itinerant d_{xy} band while “1” and “2” refer to the localized impurity state. Since ε_1 is larger than ε_0 (which is equal to 0), $E_{II} < E_{III}$. Also, as approximated in [115], $\varepsilon_1 - t$ is smaller than 0, hence $E_{II} < 0 = E_I$. Thus we shall only focus on configurations related to E_{II} and E'_{III} . Phenomenologically, the DFT result with Ti $U = 5.0$ eV corresponds to E_{II} configuration while $U = 8.0$ eV corresponds to E'_{III} configuration. This shows that for $U = 5$ eV, E_{II} is lower than E'_{III} . In the large U limit, E'_{III} can be approximated as $2\varepsilon_1 - \frac{4t^2}{U}$ and if we increase U , E'_{III} would increase while E_{II} remains the same, provided that other parameters are fixed. This suggests that for a larger U , the ground state should remain in phase II, which is contrary to what we find from the DFT calculation. An alternative possibility is that ε_1 shifts down with the increasing U . This could make E'_{III} lower than E_{II} and then the ground state configuration corresponds to E'_{III} . To clarify this, we plot the DOS for the Ti-derived t_{2g} and e_g bands in bulk SrTiO₃ for $U = 5.0$ eV and $U = 8.0$ eV in Figure

4.6. For $U = 8.0$ eV, the $t_{2g}-e_g$ splitting indeed becomes smaller by 0.2 eV compared to that obtained using $U = 5.0$ eV. This will cause ε_1 to be even lower and Ti $d_{3z^2-r^2}$ -based localized orbital to shift further down in energy relative to d_{xy} orbital. We note this shift only occurs in DFT and we conclude the ground state should be phase (II). According to Lin *et al.* [50], the two-peak structure of the Ti $3d_{3z^2-r^2}$ density of states (DOS) corresponds to the bonding and antibonding combinations of Ti-Ti $3d_{3z^2-r^2}$ -based orbitals and the separation between the peaks is twice the hopping parameter $2t$. When we compare the partial density of states projected on the Ti ion adjacent to a vacancy in a $2 \times 2 \times 4$ SrTiO₃ supercell for $U = 5$ eV and $U = 8$ eV, the separation is approximately 2.2 eV in both cases. This suggests that t has a fairly weak dependence on U .

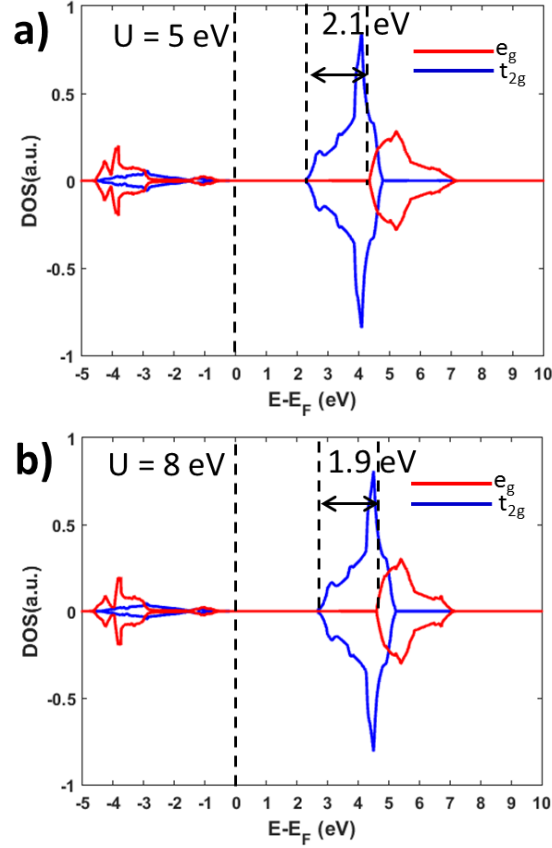


Figure 4.6 (a) The e_g - t_{2g} splitting in bulk SrTiO₃ for $U_{\text{Ti-d}} = 5$ eV and (b) $U_{\text{Ti-d}} = 8$ eV.

To estimate the magnitude of the EuO-generated magnetic field H , we compare the electronic structure of the oxygen-deficient SrTiO₃ with and without EuO layers present. For a magnetic system, with an external magnetic field, the majority band is shifted down and minority band is shifted up. The properties related to energy will change as: $f^\uparrow(\varepsilon) \rightarrow f^\uparrow(\varepsilon + \frac{1}{2}g\mu_B H)$, $f^\downarrow(\varepsilon) \rightarrow f^\downarrow(\varepsilon - \frac{1}{2}g\mu_B H)$, where g and μ_B are the g factor and Bohr magneton. This means once we apply an external magnetic field, two bands will have a relative shift of $g\mu_B H$. For a vacancy in a $2 \times 2 \times 4$ SrTiO₃ supercell, $d_{xy\uparrow}$ is aligned with $d_{xy\downarrow}$. In Figure 4.4(a), under the influence of EuO layers, the splitting between $d_{xy\uparrow}$ and $d_{xy\downarrow}$ is about 0.3 eV. This gives a rough estimate of about 0.3 eV for $g\mu_B H$.

4.5 CONCLUSION

In summary, using first-principles calculations we predict a spin-polarized 2DEG at the TiO_2/EuO interface of EuO and an oxygen-deficient SrTiO_3 . Carriers are residing mostly at the SrTiO_3 side of the interface and the strong spin polarization is induced by a proximity effect from the ferromagnetic insulator EuO. In addition, a vacancy-induced localized state appears within the band gap of STO just below the conduction band edge. This system provides a robust mechanism for generating spin-polarized 2DEG, which can possibly be used in spintronic applications, and it may have an advantage as unlike the conduction band of EuO that of STO can host a large number of carriers due to a higher density of states.

Chapter 5 Large Positive Linear Magnetoresistance in the two-dimensional t_{2g} electron gas at EuO/SrTiO_{3- δ} Interface

Inspired by the theoretical prediction of Chapter 4, my colleague Kristy J. Kormondy grew the highly spin-split ferromagnetic semiconductor EuO onto perovskite SrTiO₃ (001) with the molecular beam epitaxy. As been suggested by Posadas *et al.* [127], Eu has been demonstrated that it can scavenge oxygen from STO at high temperatures to form epitaxial EuO layers on STO, leaving an oxygen deficient layer of STO below the interface. This in turn leaves a highly conductive interfacial layer below via the generation of oxygen vacancies. This is similar to the scenario discussed in the previous section. Below the Curie temperature of EuO 70 K, this spin-polarized two-dimensional t_{2g} electron gas at the EuO/SrTiO_{3- δ} interface displays very large positive linear magnetoresistance (MR). By using Soft-x-ray angle-resolved photoemission spectroscopy (SX-ARPES) technique, t_{2g} nature of the carriers is recognized. In this chapter, using the first principles calculations results presented in Chapter 4, we use conventional Boltzmann transport theory to calculate the conductivity and magnetoresistance of the spin-polarized two-dimensional t_{2g} electron gas at the EuO/SrTiO_{3- δ} interface. Results suggest Zeeman splitting caused by proximity effect of magnetic insulator EuO is responsible for the MR. This provides an alternative approach to developing novel spintronic devices with transition metal oxides.

Results have been published as Kristy J. Kormondy, Lingyuan Gao, Xiang Li, Sirong Lu, Agham B. Posadas, Shida Shen, Maxim Tsoi, Martha R. McCartney, David J. Smith, Jianshi Zhou, Leonid L. Lev, Marius-Adrian Husanu, Vladimir N. Strocov, and Alexander A. Demkov, Sci Rep. 8 , 7721 (2018). For the experimental part, K. J. Kormondy and A. B. P. performed sample growth, XRD, XPS, and SQUID experiments, and analyzed the data. X.L., S.S., M.T. and J.S.Z. designed and performed the electrical

measurements. L.L.L., M.-A.H., and V.N.S designed and performed ARPES experiments and analyzed the ARPES data. M.R.M., S.L. and D.J.S. performed the STEM and EELS experiments and analyzed the data.

5.1 EXPERIMENTAL RESULT

5.1.1 Epitaxial Growth

EuO is highly sensitive to oxygen pressure and tends to form paramagnetic Eu_2O_3 . Therefore, special care is needed to ensure proper stoichiometry. We grow our EuO films in the thicknesses range of $\sim 5\text{-}10$ nm by molecular beam epitaxy (MBE). Following our previous study by depositing Eu metal onto STO (001) under ultra-high vacuum [127], we demonstrate this is possible to crystallize stoichiometric EuO, where oxygen is provided only by the substrate.

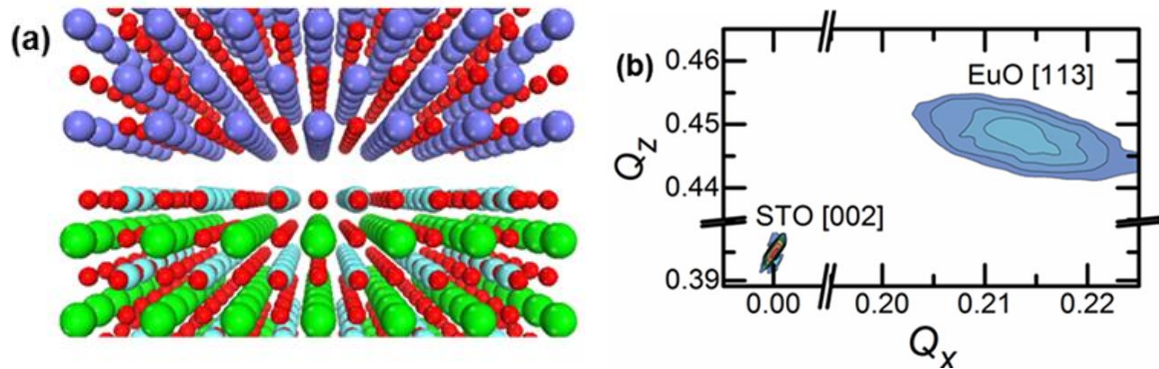


Figure 5.1 (a) Schematic plot of the EuO/SrTiO₃ heterointerface.(b) (b) Reciprocal space map of the STO (002) and EuO (113) peaks for 7 nm EuO on STO. The EuO rocksalt unit cell is rotated 45° with respect to the surface unit cell of the perovskite.

Since EuO films crystallize in the rock-salt structure, the primary EuO unit cell axis is rotated by 45° with respect to the axis of substrate surface to minimize lattice mismatch between EuO and SrTiO₃ ($\sim 7\%$). The schematic plot of the EuO/SrTiO₃ structure is presented in Figure 5.1(a) and the reciprocal space map is in Figure 5.1(b).

Additional x-ray diffraction results are presented in Figure 5.2. Lattice parameters extracted from the in-plane and out-of-plane scans are 0.513 and 0.515 nm, respectively, agreeing well with the bulk EuO value.

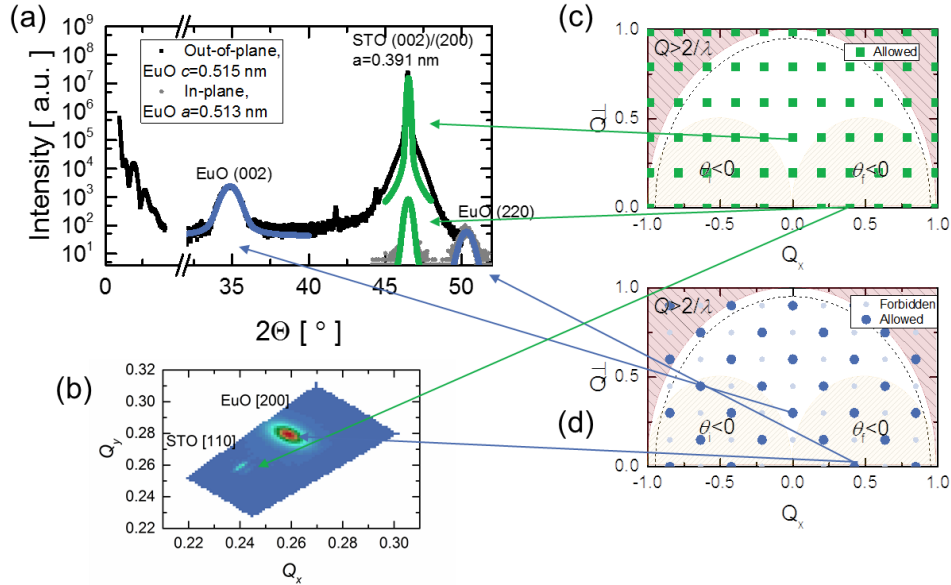


Figure 5.2 (a) X-ray diffraction coupled scans with corresponding (b) in-plane reciprocal space map and positions in reciprocal space for (c) STO and (b) EuO with a 45° rotation of the surface unit cell.

High-angle annular-dark-field image of the EuO/SrTiO₃ interface in Figure 5.3(a) demonstrates films are epitaxial with defects in the first few layers. False color maps of the Ti-L energy-loss near-edge fine-structure edge fitting in Figure 5.3(b) show oxygen vacancies are distributed at the interface. In Figure 5.3(c), with the image of heterostructure cross-section, proximity of EuO to the confined SrTiO_{3- δ} conducting layer is clearly seen. It has also been shown theoretically that due to large dielectric constant, the SrTiO₃ 2DEG can spread across 50 unit cells in the low density region ($n < 10^{14} \text{cm}^{-2}$). While in the high density region ($n > 5 \times 10^{14} \text{cm}^{-2}$) (relevant here), the 2DEG is mostly confined within a few unit cells, and the tail may still be quite long [141].

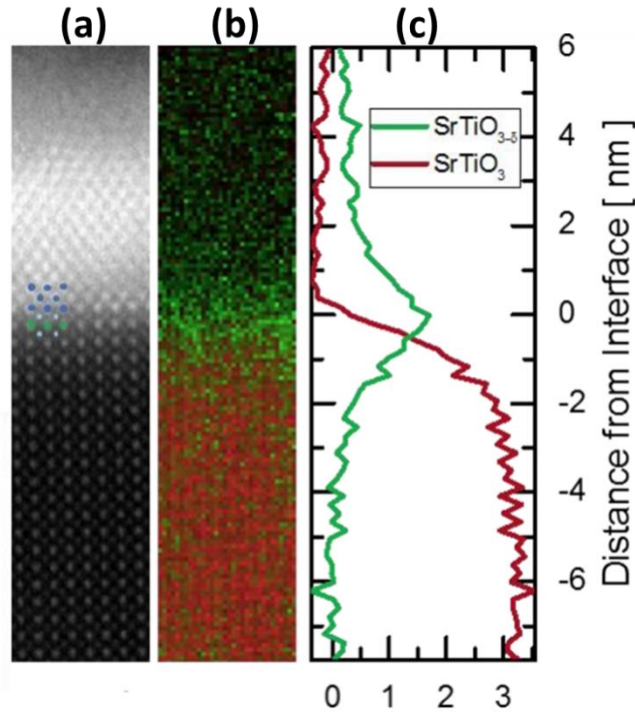


Figure 5.3 (a) High-angle annular-dark-field scanning transmission electron microscopy [100]-projection image of the EuO/STO interface. (b) Corresponding false color map shows a distribution map from the Ti L-edge fit (SrTiO₃, red; SrTiO_{3-δ}, green). (c) Ti-L coefficient as a function of position shows a sharp peak at the interface.

5.1.2 Photoemission Measurement

We use soft x-ray angle-resolved photoemission spectroscopy (SX-ARPES) to elucidate the t_{2g} character of the low dimensional electron system. The experimental X-ray absorption spectra and resonant (angle integrated) photoemission intensity across the Ti $2p$ edge is presented in Figure 5.4(a) and Figure 5.4(b). Figure 5.4(b) embeds the Eu $4f$ around $E_B \sim -2.5$ eV and the O $2p$ derived valence band states of EuO and SrTiO₃ below, while at E_F is the Ti t_{2g} derived 2DEG signal. The photoemission intensity variations in the corresponding E_B -regions are shown in Figure 5.4 (c): There the 2DEG and valence band response resonates near the Ti absorption peaks. This confirms that the the 2DEG

originates from Ti $3d$ states and they hybridize with the O $2p$ states, which are all very similar to $\text{LaAlO}_3/\text{SrTiO}_3$ interface [142,143]. On the other hand, the Eu $4f$ response shows no correlation with the Ti $2p$ absorption, indicating no hybridization is between the Eu $4f$ and Ti $3d$ states. Furthermore, resonant data of Eu $3d$ absorption edge shown in Figure 5.5 indicates no sign of any significant admixture of Eu $4f$ states in the 2DEG. All of these indicate that the 2DEG in the $\text{EuO}/\text{SrTiO}_3$ heterostructure resides on the SrTiO_3 side of the interface, in good agreement with density functional calculations presented in Chapter 4.

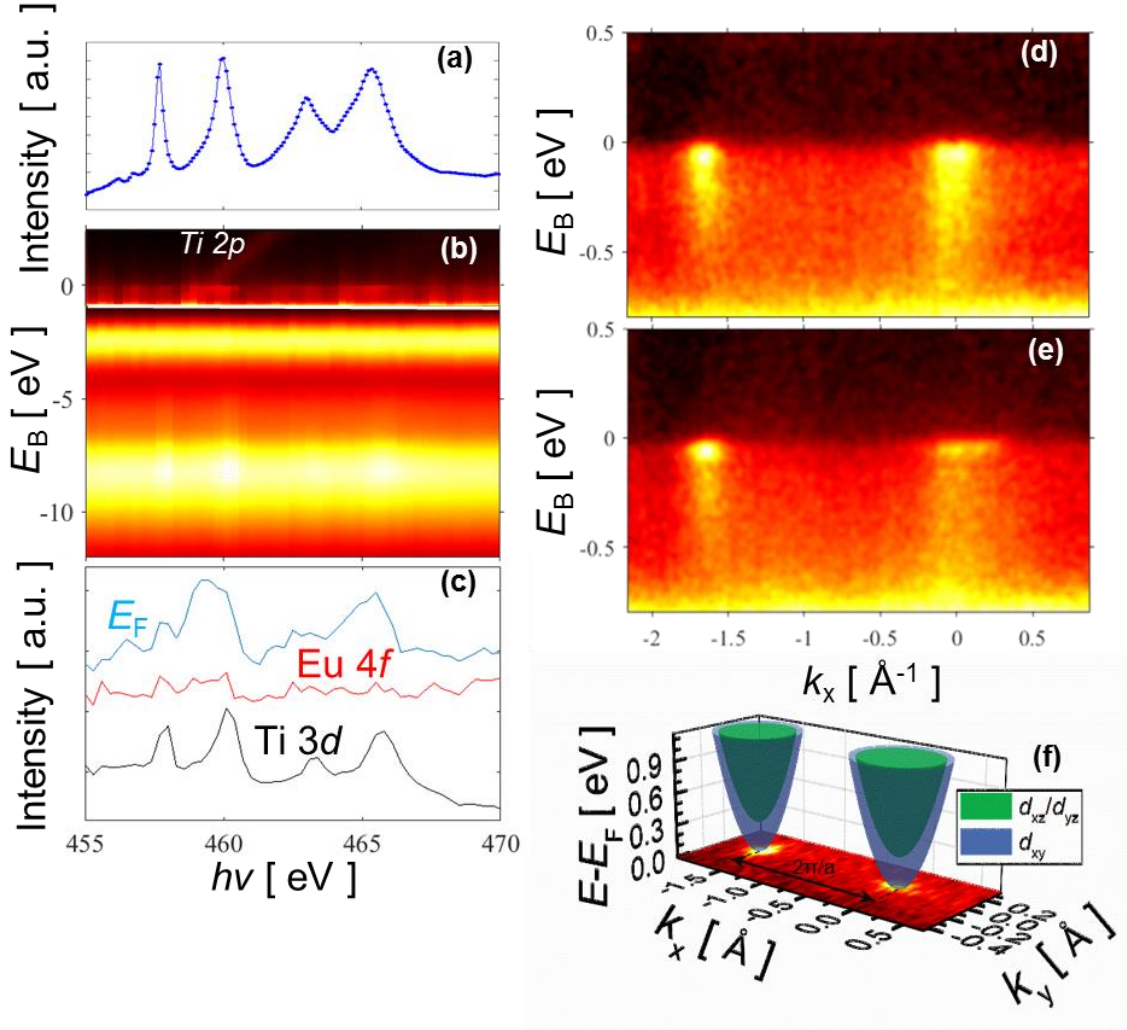


Figure 5.4 Resonant soft-X-ray ARPES of 2-nm EuO/STO heterointerface through the Ti *L*-edge. (a) XAS spectrum. (b) Resonant photoemission from the valence band as a function of excitation energy. Intensity the near- E_F region is scaled up by ~ 30 . (c) Resonant intensity for constant E_B in the valence band, Eu level and 2DEG. The valence band and 2DEG signals follow the Ti *L*-edge XAS spectrum that confirms their Ti-derived character. (d,e) SX-ARPES images at $h\nu = 460.3$ and 466 eV enhancing the d_{xy} - and d_{yz} -derived states, respectively. The intensity waterfalls are reveal polaronic nature of the interface charge carriers. (f) Fermi surface of the interface states measured at $h\nu = 466$ eV.

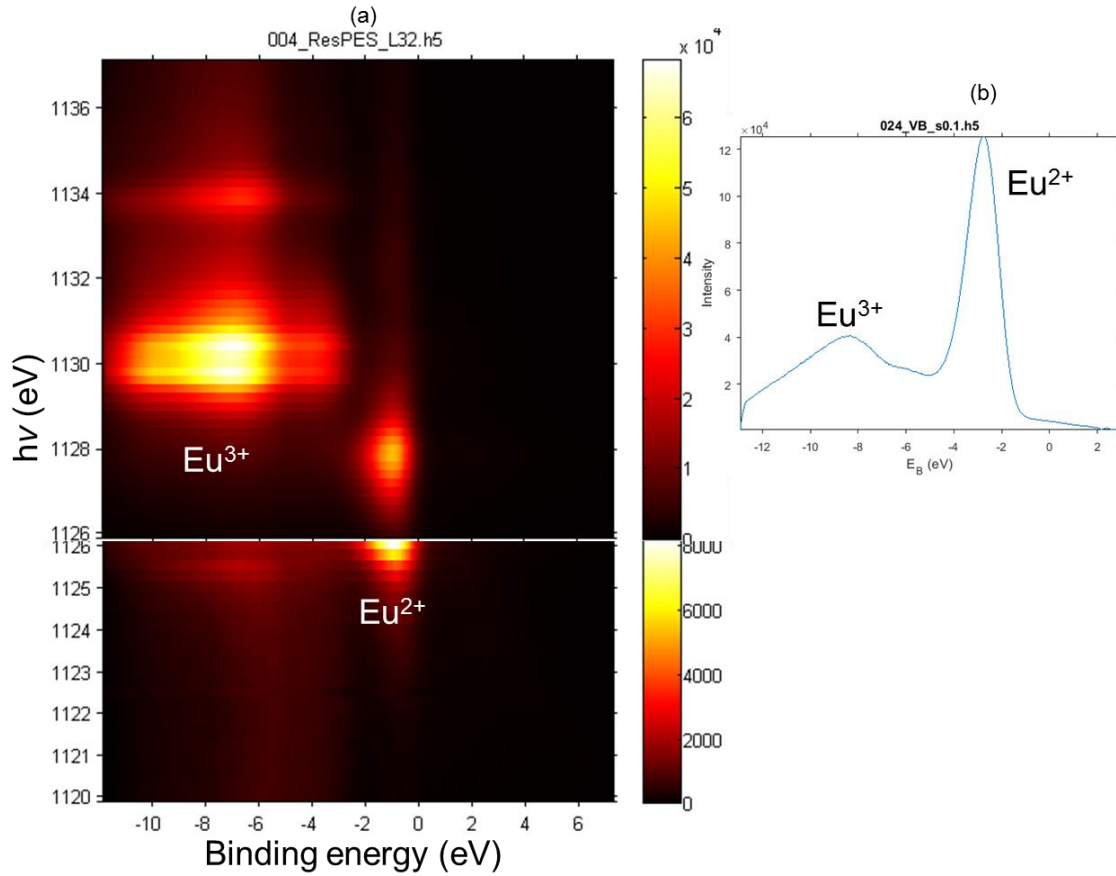


Figure 5.5 (a) Resonance photoemission spectra of valence band near Eu 3d threshold. Strong resonance of the Eu^{2+} states in the valence band at $h\nu = 1128$ eV and Eu^{3+} states at $h\nu = 1130$ eV. No resonating states at the E_F . (b) Valence band spectrum at $h\nu = 457$ eV shows the prevalence of Eu^{2+} .

Photoelectron images visualizing electron dispersions $E(\mathbf{k})$ in the 2DEG are shown in Figure 5.4(d) for $h\nu = 460.3$ eV. Compared with Figure 5.4(e) of a similar dispersion for 466 eV, the former emphasizes Ti d_{xy} states are localized near the interface, while the latter emphasizes Ti d_{yz}/d_{xz} states extended into the SrTiO_3 bulk [143]. However, we note the small Fermi vector k_F of the heavy d_{yz} band in Figure 5.4(e) demonstrates the band filling is smaller compared to the $\text{LaAlO}_3/\text{SrTiO}_3$ case [143]. Figure 5.4(f) shows the Fermi surface formed by the electrons at interface.

This was measured at $h\nu = 466$ eV to emphasize external contours formed by the ellipsoidal Ti d_{yz}/d_{xz} sheets. As expected from the experimental $E(\mathbf{k})$ dispersions, the Fermi surface is nevertheless dominated by the circular d_{xy} derived electron pocket with only small filling of the d_{yz}/d_{xz} sheets compared to the LaAlO₃/SrTiO₃ case [143]. Therefore, the overall electron density has in our case stronger interface localization compared to LaAlO₃/SrTiO₃ interface. These are all consistent with DFT calculations in the Chapter 4 very well.

5.1.3 Electrical Characterization

Figure 5.6(a) gives the measurement of the sheet resistance R_S for 7-nm EuO/STO. Results reveal in temperature range from 2-300 K the systems display metallic behavior. We also conduct Hall measurements shown as Figure 5.6(b). Sheet carrier densities can be as high as the order of 10^{16} cm⁻².

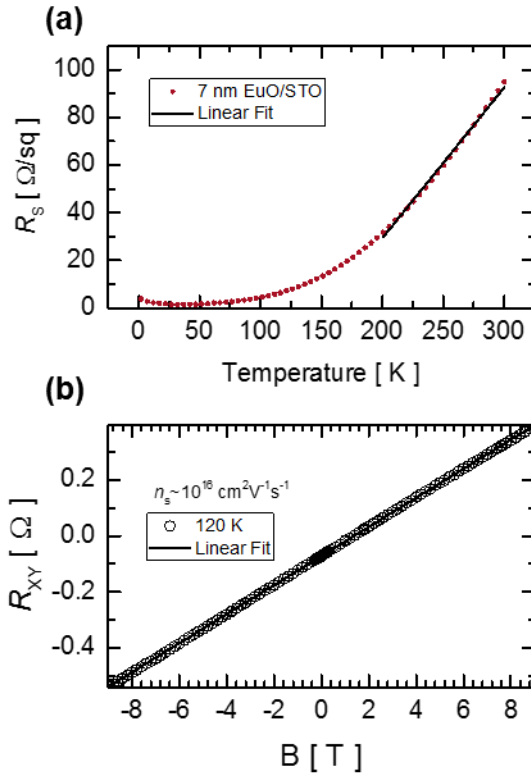


Figure 5.6 (a) Sheet resistance for a 7-nm EuO film as a function of temperature. (b) Hall resistance R_{XY} for a 7-nm EuO film at 120 K. Solid lines indicate linear fits.

Figure 5.7(a) shows the field-cooled magnetization of a 7-nm EuO film as a function of temperature. The EuO film exhibits a paramagnetic to ferromagnetic transition with decreasing temperature. Curie-Weiss fitting to this data give a Curie temperature of $T_C \sim 70$ K and an effective magnetization of $\sim 6.3 \mu_B$. From the magnetization loops measured at 10 K with magnetic fields applied in the plane of the film [see inset to Figure 5.7(a)] we extract a coercive field ~ 0.02 T and remnant magnetization $\sim 4.3 \mu_B$. These are essentially the values for bulk EuO.

Four-probe magnetoresistance $R_S(B)$ measurements for a 7-nm EuO film in a perpendicular magnetic field is shown in Figure 5.6(b). We find R_S increases linearly

with the magnetic field at 20 K and quadratically at 100 K. Solid lines indicate fits to the data of the form,

$$R_s(B) = R_s(0) \times [c_1|B| + (c_2B)^2], \quad (5.1)$$

where c_1 and c_2 are the linear and quadratic fit coefficients, respectively, shown in Figure 5.7(b) as a function of temperature. The quadratic magnetoresistance component is present below ~ 150 K, while the linear component emerges below ~ 80 K. The magnetoresistance (MR), defined as,

$$MR = \frac{R_s(B) - R_s(0)}{R_s(0)}, \quad (5.2)$$

decreases rapidly as the measurement temperature increases, and is essentially zero at room temperature as shown in Figure 5.6(c). These demonstrate our EuO/STO heterostructures display temperature-dependent linear positive magnetoresistance below the Curie temperature.

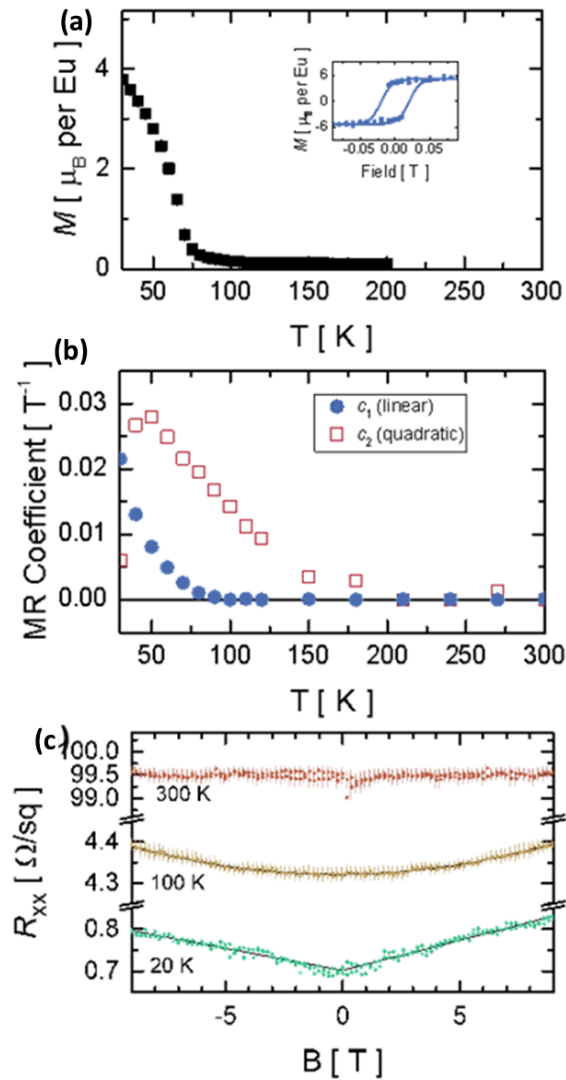


Figure 5.7 (a) Magnetoresistance (MR) data measured in a perpendicular magnetic field at 20 K, 100 K, and 300 K. Solid lines indicate fits to the data. The MR increases linearly with the magnetic field at 20 K, quadratically at 100 K, and is field-independent at room temperature. (b) Linear c_1 and quadratic c_2 MR fit coefficients for the same film as a function of temperature. (c) Field-cooled magnetization M of a similar 7-nm EuO film as a function of temperature at constant in-plane magnetic field of 0.01 T. Inset: corresponding magnetization loop measured at 10 K.

5.2 INTRODUCTION TO ORIGINS OF POSITIVE LINEAR MAGNETORESISTANCE

A positive linear magnetoresistance (LMR) can have several possible origins:

- (1) A classical mechanism proposed by Parish and Littlewood attributes LMR as a consequence of potential and mobility fluctuations in an inhomogeneous electronic system [144,145]. This is found in doped silver chalcogenides $\text{Ag}_{2+\delta}\text{Se}$ over a large temperature range between 4.5 K and 300 K. The classical mechanism considers the strong inhomogeneity of the system as the main influence and models a random resistor network. The hypothesis assumes inhomogeneous distribution of silver ions results in large spatial fluctuation of conductivity of the material, as the doped silver chalcogenides is “granular” material. The assumption also explains why MR decreases with increasing temperature as resistance only depends on mobility but is independent of carrier density.
- (2) A quantum mechanism proposed by Abrikosov includes effects due to electronic correlations [146,147]. The quantum mechanism is based on the assumption that the energy spectrum is gapless and linear. It also takes inhomogeneity of metals into consideration. LMR would occur at the quantum limit if the applied magnetic field is so large that only one or few Landau levels (LLs) are populated. The required condition is that only one Landau level is participating, and a condition that $n < \left(\frac{eH}{ch}\right)^{\frac{3}{2}}$ needs to be fulfilled. With H in the order of $\sim 10\text{T}$, the right-hand side value is 10^{18}cm^{-3} .
- (3) A quantum interference explanation introduced by Manya *et al.* attributes the LMR of to the interaction. In a weakly disordered

system, a magnetic field suppresses localization effect and predicts a negative MR. If interaction is considered, spin-orbit scattering and orbital effects of an interacting electron gas can lead to a positive LMR. This has been observed in $\text{Fe}_{1-x}\text{Co}_x\text{Si}$ and geometrically constrained ferromagnets Fe and Ni films [148,149]. For the former, it has been explained as the enhanced electron-electron interactions by disorder. For the latter, the magnetic field induces a spin gap suppressing the contribution to conductivity and leads to a positive MR.

- (4) LMR induced by Zeeman splitting, which is due to the gradual increase of the splitting between minority spin-up and majority spin-down carriers in presence of a magnetic field. For this mechanism, the differences in mobility are crucial in order to get specifically a positive sign (and not negative) of the magnetoresistance. Onose *et al.* have used this origin to explain the LMR observed in $\text{Fe}_{1-x}\text{Co}_x\text{Si}$ [150].

There is no strong evidence suggesting that the mechanism of LMR in our current system could be related with the inhomogeneity. Under the classical mechanism, LMR could exist over a large temperature range and has a weak dependence on temperature: Doped silver chalcogenides $\text{Ag}_{2+\delta}\text{Se}$ and $\text{Ag}_{2+\delta}\text{Te}$ display a positive LMR from 4.5 K to room temperature 300 K. While in our sample, the positive LMR is only present below the EuO Curie temperature T_c . Above T_c , the behavior is quadratic, similar to conventional semiconductors. It would be too much of a coincidence that it becomes linear at the transition temperature. Therefore, we rule out the first possibility.

For the second, in quantum mechanism, the predicted density of carriers is too low compared with the carrier density in our system. We have a carrier density of

10^{16}cm^{-2} within a conductive layer of $\sim 2.5\text{-}5$ nm, which corresponds to 10^{22}cm^{-3} , much larger than 10^{18}cm^{-3} .

For the third quantum correlation mechanism, we follow Gerber *et al.*'s work and calculate the correction to resistivity due to correlation. Though the MR is linearly dependent, the order of MR over magnetic field is over ten orders of magnitude smaller compared with our measurement. Thus we also excluded this mechanism.

Considering the quadratic MR to linear MR transition over T_C , we consider Zeeman splitting model applicable. We'd like to point out that though oxygen vacancies commonly exist in thin films of SrTiO_3 , no positive LMR in oxygen deficient SrTiO_3 has ever been reported.

5.3 PROPERTIES OF CONFINED TWO-DIMENSIONAL ELECTRON GAS IN SrTiO_3

When we talk about confined 2DEG in SrTiO_3 , we refer to SrTiO_3 heterostructure with polar perovskites, electrostatically-gated SrTiO_3 or SrTiO_3 surfaces. In these systems, several subbands are confined in direction perpendicular to the interface (z direction) and 2DEG can spread within N layers. As suggested by [141], an intralayer hopping t and interlayer hopping t' parameter can be introduced for the t_{2g} states ($t > t'$). In this way, we can use a tight-binding model to describe these states and the one electron energy dispersion has a familiar trigonometric function form. Near the Γ point, the energy of three bulk t_{2g} -derived bands are:

$$\begin{aligned} \varepsilon &= \frac{\hbar^2}{2m_L} k_x^2 + \frac{\hbar^2}{2m_L} k_y^2 + \frac{\hbar^2}{2m_H} k_z^2 && d_{xy} \text{ orbital} \\ \varepsilon &= \frac{\hbar^2}{2m_L} k_x^2 + \frac{\hbar^2}{2m_H} k_y^2 + \frac{\hbar^2}{2m_L} k_z^2 && d_{xz} \text{ orbital} \quad (5.3) \\ \varepsilon &= \frac{\hbar^2}{2m_H} k_x^2 + \frac{\hbar^2}{2m_L} k_y^2 + \frac{\hbar^2}{2m_L} k_z^2 && d_{yz} \text{ orbital} \end{aligned}$$

Here, m_L stands for light mass while m_h stands for heavy mass. According to the APRES data [106], $m_L \approx 0.7m_e$, $m_h \approx 10\sim 20m_e$. Therefore, three bands are degenerate at the Γ point, and the d_{xy} - and d_{xz} -derived bands have the same larger curvature along x axis.

If states are confined within a few layers along the z direction, there would be no hopping along the z direction so there should be no dispersion in the k_z direction. Then for the confined 2DEG, we have:

$$\varepsilon = \begin{cases} \frac{\hbar^2}{2m_L}k_x^2 + \frac{\hbar^2}{2m_L}k_y^2 - 4t & d_{xy} \text{ band} \\ \frac{\hbar^2}{2m_L}k_x^2 + \frac{\hbar^2}{2m_H}k_y^2 - 2(t + t') & d_{xz} \text{ band} \\ \frac{\hbar^2}{2m_H}k_x^2 + \frac{\hbar^2}{2m_L}k_y^2 - 2(t + t') & d_{yz} \text{ band} \end{cases} \quad (5.4)$$

Now at the Γ point, the splitting between the d_{xy} and d_{xz}/d_{yz} states is $2(t - t')$. From the density of states (DOS) in our *ab-initio* calculation, we see that the interfacial d_{xy} band is shifted down in energy by 0.3 eV relative to the other t_{2g} bands.

The DOS for the anisotropic 2DEG is calculated first. The energy is:

$$\varepsilon = \frac{\hbar^2}{2m_L}k_x^2 + \frac{\hbar^2}{2m_H}k_y^2 \quad (5.5)$$

Without considering the spin degree of freedom, we can calculate the DOS:

$$\begin{aligned} D(\varepsilon) &= \frac{1}{(2\pi)^2} \int dk_x dk_y \delta(\varepsilon - \varepsilon_k) \\ &= \frac{1}{(2\pi)^2} \int dk_x dk_y \delta\left(\varepsilon - \frac{\hbar^2}{2m_L}k_x^2 - \frac{\hbar^2}{2m_H}k_y^2\right) \end{aligned} \quad (5.6)$$

By changing variables,

$$\bar{k}_x = \frac{k_x}{\sqrt{\frac{2m_L\varepsilon}{\hbar^2}}}, \quad \bar{k}_y = \frac{k_y}{\sqrt{\frac{2m_H\varepsilon}{\hbar^2}}}, \quad (5.7)$$

and also by changing from the orthogonal coordinate system to the polar coordinate system, we calculate:

$$\begin{aligned}
D(\varepsilon) &= \frac{1}{(2\pi)^2} \frac{2\varepsilon}{\hbar^2} \sqrt{m_L m_H} \int d\bar{k}_x d\bar{k}_y \delta\left(\varepsilon \left(1 - \bar{k}_x^2 - \bar{k}_y^2\right)\right) \\
&= \frac{1}{(2\pi)^2} \frac{2\varepsilon}{\hbar^2} \sqrt{m_L m_H} \frac{1}{\varepsilon} \int 2\pi \bar{k} d\bar{k} \delta\left((1 - \bar{k}^2)\right) \\
&= \frac{1}{(2\pi)^2} \frac{2\varepsilon}{\hbar^2} \sqrt{m_L m_H} \frac{1}{\varepsilon} \int \pi d\bar{k}^2 \delta\left((1 - \bar{k}^2)\right) \\
&= \frac{\sqrt{m_L m_H}}{2\pi \hbar^2}
\end{aligned} \tag{5.8}$$

If $m_L = m_H$, Then $D(\varepsilon) = \frac{m_L}{2\pi \hbar^2}$. This can be considered as the DOS for confined d_{xy} 2DEG in SrTiO₃. Similarly, we can obtain the density of states for the d_{xz} and d_{yz} 2DEG, respectively. To summarize, the DOS for the 2DEG in all three t_{2g} -derived bands is:

$$D = \begin{cases} \frac{m_L}{2\pi \hbar^2} & d_{xy} \text{ band} \\ \frac{\sqrt{m_L m_H}}{2\pi \hbar^2} & d_{xz} \text{ band} \\ \frac{\sqrt{m_L m_H}}{2\pi \hbar^2} & d_{yz} \text{ band} \end{cases} \tag{5.9}$$

We note that in the 2D case, the DOS is independent of the energy. Also, $D(d_{xz}) = D(d_{yz})$. As a comparison, we calculate the DOS of 3D electron gas (3DEG) and show the relationship between DOS and energy. The energy is:

$$\varepsilon = \frac{\hbar^2}{2m_L} k_x^2 + \frac{\hbar^2}{2m_L} k_y^2 + \frac{\hbar^2}{2m_H} k_z^2, \tag{5.10}$$

and the DOS is:

$$\begin{aligned}
D(\varepsilon) &= \frac{1}{(2\pi)^3} \left(\sqrt{\frac{2m_L\varepsilon}{\hbar^2}} \right)^2 \sqrt{\frac{2m_H\varepsilon}{\hbar^2}} \int dk_x dk_y dk_z \delta \left(\varepsilon - \left(\frac{\hbar^2}{2m_L} k_x^2 + \frac{\hbar^2}{2m_L} k_y^2 + \frac{\hbar^2}{2m_H} k_z^2 \right) \right) \\
&= \frac{1}{(2\pi)^3} \left(\sqrt{\frac{2m_L\varepsilon}{\hbar^2}} \right)^2 \sqrt{\frac{2m_H\varepsilon}{\hbar^2}} \int d\bar{k}_x d\bar{k}_y d\bar{k}_z \delta \left(\varepsilon \left(1 - \bar{k}_x^2 - \bar{k}_y^2 - \bar{k}_z^2 \right) \right) \\
&= \frac{1}{(2\pi)^3} \left(\sqrt{\frac{2m_L\varepsilon}{\hbar^2}} \right)^2 \sqrt{\frac{2m_H\varepsilon}{\hbar^2}} \frac{1}{\varepsilon} \int d\bar{k}_x d\bar{k}_y d\bar{k}_z \delta \left(1 - \bar{k}_x^2 - \bar{k}_y^2 - \bar{k}_z^2 \right) \\
&= \frac{1}{(2\pi)^3} \left(\sqrt{\frac{2m_L\varepsilon}{\hbar^2}} \right)^2 \sqrt{\frac{2m_H\varepsilon}{\hbar^2}} \frac{1}{\varepsilon} 2\pi = \frac{1}{4\pi^2} \frac{2m_L}{\hbar^2} \sqrt{\frac{2m_H}{\hbar^2}} \sqrt{\varepsilon} \quad (5.11)
\end{aligned}$$

Therefore, for the 3DEG, the DOS has a $\sim\varepsilon^{1/2}$ relationship.

5.4 CLASSICAL CONDUCTIVITY FOR TWO-DIMENSIONAL ELECTRON GAS

Our calculation starts from the original derivation of the electrical conductivity, as introduced in Chapter 7.2 of [151]. When scattering occurs, there would be a change in the distribution function $g_k = f_k - f_k^{t=0}$, and f_k , g_k obey:

$$-\frac{\partial f_k}{\partial t} = -\frac{\partial g_k}{\partial t} = \frac{g_k}{\tau} \quad (5.12)$$

Here we assume $g_k(t) = g_k(0)e^{-t/\tau}$, and consider τ as the relaxation time. According to the Boltzmann equation, we have:

$$-\frac{\partial f_k}{\partial t} = \left(-\frac{\partial f^0}{\partial \varepsilon} \right) \mathbf{v}_k \cdot e\mathbf{E} \quad (5.13)$$

$$g_k = \left(-\frac{\partial f^0}{\partial \varepsilon} \right) \tau \mathbf{v}_k \cdot e\mathbf{E} \quad (5.14)$$

Therefore, the corresponding current density is:

$$\begin{aligned}
\mathbf{j} &= \int e \mathbf{v}_k f_k d^3 \mathbf{k} = \int e \mathbf{v}_k (f_k^0 + g_k) d^3 \mathbf{k} = \int e \mathbf{v}_k g_k d^3 \mathbf{k} \\
&= \frac{1}{(2\pi)^3} \int e^2 \tau \mathbf{v}_k (\mathbf{v}_k \cdot \mathbf{E}) \left(-\frac{\partial f^0}{\partial \varepsilon} \right) d^3 \mathbf{k} \\
&= \frac{1}{(2\pi)^3} \int e^2 \tau \mathbf{v}_k \mathbf{v}_k \left(-\frac{\partial f^0}{\partial \varepsilon} \right) d^3 \mathbf{k} \cdot \mathbf{E} \tag{5.15}
\end{aligned}$$

As the current density is defined as the product of the conductivity tensor and the external electric field, the conductivity tensor is:

$$\sigma^{\alpha\beta} = \frac{1}{(2\pi)^3} \int e^2 \tau \mathbf{v}_k^\alpha \mathbf{v}_k^\beta \left(-\frac{\partial f^0}{\partial \varepsilon} \right) d^3 \mathbf{k} \tag{5.16}$$

For isotropic systems, the conductivity tensor is symmetric:

$$\sigma^{xx} = \sigma^{yy} \text{ (2D)}, \quad \sigma^{xx} = \sigma^{yy} = \sigma^{zz} \text{ (3D)}, \tag{5.17}$$

and the 2D conductivity tensor is obtained as:

$$\begin{aligned}
\sigma^{xx} &= \frac{1}{(2\pi)^2} \int e^2 \tau \mathbf{v}_k^x \mathbf{v}_k^x \left(-\frac{\partial f^0}{\partial \varepsilon} \right) d^3 \mathbf{k} = \frac{e^2 \tau}{(2\pi)^2} \int \frac{v_k^2}{2} \left(-\frac{\partial f^0}{\partial \varepsilon} \right) d^3 \mathbf{k} = \\
&= \frac{e^2 \tau}{(2\pi)^2} \int v_k^2 \delta(\varepsilon - \varepsilon_F) d^3 \mathbf{k} = \frac{e^2 \tau v(\varepsilon_F)^2}{2 (2\pi)^2} \int \delta(\varepsilon - \varepsilon_F) d^3 \mathbf{k} = \\
&= \frac{e^2 \tau v(\varepsilon_F)^2}{2} D(\varepsilon_F) \tag{5.18}
\end{aligned}$$

We note that $v(\varepsilon_F)$ only depends on the Fermi energy rather than direction of the Fermi vector. For the 3D conductivity tensor, the derivation is similar:

$$\sigma^{xx} = \frac{e^2 \tau v(\varepsilon_F)^2}{3} D(\varepsilon_F) \tag{5.19}$$

Below we show the conductivity tensor for the anisotropic case, which is more general.

We first deal with the d_{xz} 2DEG:

$$\varepsilon = \frac{\hbar^2}{2m_L} k_x^2 + \frac{\hbar^2}{2m_H} k_y^2 \tag{5.20}$$

The xx component of the conductivity tensor is:

$$\begin{aligned}
\sigma^{xx} &= \frac{1}{(2\pi)^2} \int e^2 \tau \mathbf{v}_{\mathbf{k}^x} \mathbf{v}_{\mathbf{k}^x} \left(-\frac{\partial f^0}{\partial \varepsilon} \right) d^3 \mathbf{k} \\
&= \frac{1}{(2\pi)^2} \int e^2 \tau \left(\frac{\hbar k_x}{m_L} \right)^2 \delta \left(\frac{\hbar^2}{2m_L} k_x^2 + \frac{\hbar^2}{2m_H} k_y^2 - \varepsilon_F \right) d^3 \mathbf{k} \\
&= \frac{e^2 \tau}{(2\pi)^2} \left(\frac{\hbar}{m_L} \right)^2 \frac{2m_L \varepsilon_F}{\hbar^2} \sqrt{\frac{2m_L \varepsilon_F}{\hbar^2}} \sqrt{\frac{2m_H \varepsilon_F}{\hbar^2}} \int d\bar{k}_x d\bar{k}_y \bar{k}_x^2 \delta \left(\varepsilon_F \left(1 - \bar{k}_x^2 \right. \right. \\
&\quad \left. \left. - \bar{k}_y^2 \right) \right) = \frac{e^2 \tau \varepsilon_F \sqrt{m_L m_H}}{2\pi m_L \hbar^2} = \frac{e^2 \tau \varepsilon_F \sqrt{m_L m_H}}{2 m_L \pi \hbar^2} \tag{5.21}
\end{aligned}$$

To summarize, the 2D σ^{xx} for all three t_{2g} 2DEG is:

$$\sigma^{xx} = \begin{cases} \frac{e^2 \tau \varepsilon_F}{2 \pi \hbar^2} = \frac{e^2 \tau v(\varepsilon_F)^2}{2} D(\varepsilon_F) & d_{xy} \text{ band} \\ \frac{e^2 \tau \varepsilon_F}{2 \pi \hbar^2} \sqrt{\frac{m_H}{m_L}} & d_{xz} \text{ band} \\ \frac{e^2 \tau \varepsilon_F}{2 \pi \hbar^2} \sqrt{\frac{m_L}{m_H}} & d_{yz} \text{ band} \end{cases} \tag{5.22}$$

Since $\frac{\sigma_{xz}}{\sigma_{yz}} = \frac{m_H}{m_L}$ is very large, the contribution from the d_{yz} 2DEG to the total σ^{xx} can be neglected.

We end the current section by calculating 3D σ^{xx} . Result for the d_{xy} state is shown first:

$$\begin{aligned}
\sigma^{xx} &= \frac{1}{(2\pi)^3} \int e^2 \tau \mathbf{v}_{\mathbf{k}^x} \mathbf{v}_{\mathbf{k}^x} \left(-\frac{\partial f^0}{\partial \varepsilon} \right) d^3 \mathbf{k} \\
&= \frac{1}{(2\pi)^3} \int e^2 \tau \left(\frac{\hbar k_x}{m_L} \right)^2 \delta \left(\frac{\hbar^2}{2m_L} k_x^2 + \frac{\hbar^2}{2m_L} k_y^2 + \frac{\hbar^2}{2m_H} k_z^2 - \varepsilon_F \right) d^3 \mathbf{k} \\
&= \frac{e^2 \tau}{(2\pi)^3} \left(\frac{\hbar}{m_L} \right)^2 \frac{2m_L \varepsilon_F}{\hbar^2} \frac{2m_L \varepsilon_F}{\hbar^2} \sqrt{\frac{2m_H \varepsilon_F}{\hbar^2}} \int d\bar{k}_x d\bar{k}_y d\bar{k}_z \bar{k}_x^2 \delta \left(\varepsilon_F \left(1 - \bar{k}_x^2 \right. \right. \\
&\quad \left. \left. - \bar{k}_y^2 - \bar{k}_z^2 \right) \right) = \frac{e^2 \tau \varepsilon_F}{3\pi^2 \hbar^2} \sqrt{\frac{2m_H \varepsilon_F}{\hbar^2}} = \frac{e^2 \tau \varepsilon_F m_L}{3 m_L \pi^2 \hbar^2} \sqrt{\frac{2m_H \varepsilon_F}{\hbar^2}} \\
&= \frac{e^2 \tau v(\varepsilon_F)^2}{3} D(\varepsilon_F) \tag{5.23}
\end{aligned}$$

And the 3D σ^{xx} for all three t_{2g} states is summarized as:

$$\begin{aligned}
\sigma^{xx} &= \frac{e^2 \tau \varepsilon_F}{3\pi^2 \hbar^2} \sqrt{\frac{2m_H \varepsilon_F}{\hbar^2}} && d_{xy} \text{ band} \\
&= \frac{e^2 \tau \varepsilon_F}{3\pi^2 \hbar^2} \sqrt{\frac{2m_H \varepsilon_F}{\hbar^2}} && d_{xz} \text{ band} \\
&\left(\frac{e^2 \tau m_L \varepsilon_F}{3\pi^2 m_H \hbar^2} \sqrt{\frac{2m_H \varepsilon_F}{\hbar^2}} \right) && d_{yz} \text{ band}
\end{aligned} \tag{5.24}$$

Similar to a 2D system, we can neglect the d_{yz} contribution to σ^{xx} in a 3D system.

5.5 MAGNETORESISTANCE IN SPIN-POLARIZED SrTiO₃ TWO-DIMENSIONAL ELECTRON GAS

Now we come back to our spin-polarized 2DEG system at the interface of the EuO/SrTiO₃ heterostructure. First we talk about the band shift under a magnetic field: With an external field H , the majority spin band is shifted down in energy while the minority band is shifted up. Functions related with energy ε will change as:

$$f^\uparrow(\varepsilon) \rightarrow f^\uparrow\left(\varepsilon + \frac{1}{2}g\mu_B H\right) \tag{5.25}$$

$$f^\downarrow(\varepsilon) \rightarrow f^\downarrow\left(\varepsilon - \frac{1}{2}g\mu_B H\right) \tag{5.26}$$

With a magnetic field, the Fermi level ε_F is adjusted accordingly. We start from the simplest two-bands model. Without the magnetic field, $D_+(\varepsilon) = D_-(\varepsilon)$, and the total number of electrons is:

$$N = \int_{-\infty}^{\varepsilon_F} D_+(\varepsilon) d\varepsilon + \int_{-\infty}^{\varepsilon_F} D_-(\varepsilon) d\varepsilon \tag{5.27}$$

With a magnetic field, the total number is counted as:

$$N = \int_{-\infty}^{\varepsilon_F + \delta\varepsilon_F} D_+(\varepsilon + \frac{1}{2}g\mu_B H) d\varepsilon + \int_{-\infty}^{\varepsilon_F + \delta\varepsilon_F} D_-(\varepsilon - \frac{1}{2}g\mu_B H) d\varepsilon \tag{5.28}$$

The change of Fermi level $\delta\varepsilon_F$ is:

$$\delta\varepsilon_F = \frac{1}{2}g\mu_B H \frac{D_\downarrow(\varepsilon_F) - D_\uparrow(\varepsilon_F)}{D_\downarrow(\varepsilon_F) + D_\uparrow(\varepsilon_F)} \tag{5.29}$$

In the current system, we have one interfacial (IF) d_{xy}^\uparrow band, and three non-spin-polarized t_{2g} bands in the bulk-like region (we call them bulk t_{2g} bands). From the *ab-initio* calculation, IF band is shifted down by Δ relative to the bulk-like t_{2g} bands. We show the confined 2DEG in SrTiO₃ in a schematic plot in Figure 5.8.

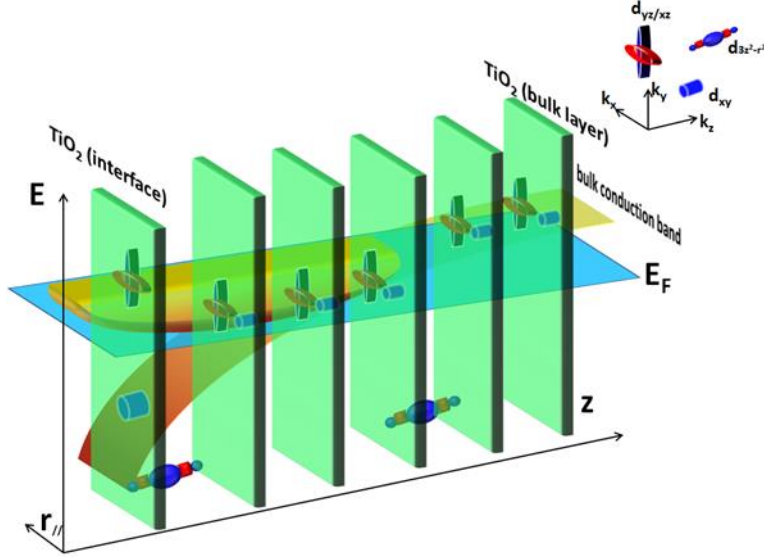


Figure 5.8 Schematic plot of the two dimensional t_{2g} electron gas in SrTiO₃.

The energy of these bands is given by:

$$\varepsilon = \begin{cases} \frac{\hbar^2}{2m_L} k_x^2 + \frac{\hbar^2}{2m_L} k_y^2 - \Delta & \text{IF } d_{xy}^\uparrow \text{ bands} \\ \frac{\hbar^2}{2m_L} k_x^2 + \frac{\hbar^2}{2m_L} k_y^2 & \text{bulk } d_{xy} \text{ band} \\ \frac{\hbar^2}{2m_L} k_x^2 + \frac{\hbar^2}{2m_H} k_y^2 & \text{bulk } d_{xz} \text{ band} \\ \frac{\hbar^2}{2m_H} k_x^2 + \frac{\hbar^2}{2m_L} k_y^2 & \text{bulk } d_{yz} \text{ band} \end{cases} \quad (5.30)$$

With an external magnetic field, the change of the Fermi level $\delta\varepsilon_F$ is:

$$\delta\varepsilon_F = \frac{1}{2} g\mu_B H \frac{\sum_{\text{bulk } t_{2g}} D^\downarrow(\varepsilon_F) - \sum_{\text{bulk } t_{2g}} D^\uparrow(\varepsilon_F) - D^\uparrow_{IF}(\varepsilon_F + \Delta)}{\sum_{\text{bulk } t_{2g}} D^\downarrow(\varepsilon_F) + \sum_{\text{bulk } t_{2g}} D^\uparrow(\varepsilon_F) + D^\uparrow_{IF}(\varepsilon_F + \Delta)} \quad (5.31)$$

$$D^\downarrow(\varepsilon_F) = D^\uparrow(\varepsilon_F), \quad D^\uparrow_{IF}(\varepsilon_F) = D^\uparrow(\varepsilon_F + \Delta) \quad (5.32)$$

The total conductivity tensor is:

$$\begin{aligned}
\sigma^{xx}(H = 0) &= \sigma_{IF_{xy}(l)}^{xx} + \sigma_{bulk\ d_{xy}(l)}^{xx} + \sigma_{bulk\ d_{xy}(l)}^{xx} + \sigma_{bulk\ d_{xz}(l)}^{xx} \\
&+ \sigma_{bulk\ d_{xz}(l)}^{xx} + \sigma_{bulk\ d_{yz}(l)}^{xx} + \sigma_{bulk\ d_{yz}(l)}^{xx} \\
&= \frac{e^2 \tau_{IF} \varepsilon_F + \Delta}{2 \pi \hbar^2} + 2 \times \frac{e^2 \tau_{bulk\ d_{xy}} \varepsilon_F}{2 \pi \hbar^2} + 2 \times \frac{e^2 \tau_{bulk\ d_{xz}} \varepsilon_F}{2 \pi \hbar^2} \sqrt{\frac{m_H}{m_L}} + 2 \\
&\times \frac{e^2 \tau_{bulk\ d_{yz}} \varepsilon_F}{2 \pi \hbar^2} \sqrt{\frac{m_L}{m_H}} \tag{5.33}
\end{aligned}$$

When we apply magnetic field, the conductivity tensor becomes:

$$\begin{aligned}
\sigma^{xx}(H \neq 0) &= \frac{e^2 \tau_{IF} \varepsilon_F + \delta \varepsilon_F + \Delta + \frac{1}{2} g \mu_B H}{2 \pi \hbar^2} + \frac{e^2 \tau_{bulk\ d_{xy}} \varepsilon_F + \delta \varepsilon_F + \frac{1}{2} g \mu_B H}{2 \pi \hbar^2} \\
&+ \frac{e^2 \tau_{bulk\ d_{xy}} \varepsilon_F + \delta \varepsilon_F - \frac{1}{2} g \mu_B H}{2 \pi \hbar^2} \\
&+ \frac{e^2 \tau_{bulk\ d_{xz}} \varepsilon_F + \delta \varepsilon_F + \frac{1}{2} g \mu_B H}{2 \pi \hbar^2} \sqrt{\frac{m_H}{m_L}} \\
&+ \frac{e^2 \tau_{bulk\ d_{xz}} \varepsilon_F + \delta \varepsilon_F - \frac{1}{2} g \mu_B H}{2 \pi \hbar^2} \sqrt{\frac{m_H}{m_L}} \\
&+ \frac{e^2 \tau_{bulk\ d_{yz}} \varepsilon_F + \delta \varepsilon_F + \frac{1}{2} g \mu_B H}{2 \pi \hbar^2} \sqrt{\frac{m_L}{m_H}} \\
&+ \frac{e^2 \tau_{bulk\ d_{yz}} \varepsilon_F + \delta \varepsilon_F - \frac{1}{2} g \mu_B H}{2 \pi \hbar^2} \sqrt{\frac{m_L}{m_H}} \tag{5.34}
\end{aligned}$$

By taking the difference between $\sigma^{xx}(H \neq 0)$ and $\sigma^{xx}(H = 0)$, we obtain:

$$\begin{aligned}
& \sigma^{xx}(H \neq 0) - \sigma^{xx}(H = 0) \\
&= \frac{e^2 \tau_{IF}}{2} \frac{\delta \varepsilon_F + \frac{1}{2} g \mu_B H}{\pi \hbar^2} + 2 \times \frac{e^2 \tau_{bulk\ d_{xy}}}{2} \frac{\delta \varepsilon_F}{\pi \hbar^2} + 2 \times \frac{e^2 \tau_{bulk\ d_{xz}}}{2} \frac{\delta \varepsilon_F}{\pi \hbar^2} \sqrt{\frac{m_H}{m_L}} + 2 \\
&\times \frac{e^2 \tau_{bulk\ d_{yz}}}{2} \frac{\delta \varepsilon_F}{\pi \hbar^2} \sqrt{\frac{m_L}{m_H}} \\
&= \frac{e^2 \tau_{IF}}{2} \frac{\frac{1}{2} g \mu_B H}{\pi \hbar^2} \frac{2 \sum_{bulk\ t_{2g}} D^\downarrow(\varepsilon_F)}{\sum_{bulk\ t_{2g}} D^\downarrow(\varepsilon_F) + \sum_{bulk\ t_{2g}} D^\uparrow(\varepsilon_F) + D^\uparrow_{IF}(\varepsilon_F)} \\
&+ \frac{e^2 \tau_{bulk\ d_{xy}}}{2} \frac{\frac{1}{2} g \mu_B H}{\pi \hbar^2} \frac{2 \left(\sum_{bulk\ t_{2g}} D^\downarrow(\varepsilon_F) - \sum_{bulk\ t_{2g}} D^\uparrow(\varepsilon_F) - D^\uparrow_{IF}(\varepsilon_F) \right)}{\sum_{bulk\ t_{2g}} D^\downarrow(\varepsilon_F) + \sum_{bulk\ t_{2g}} D^\uparrow(\varepsilon_F) + D^\uparrow_{IF}(\varepsilon_F)} \\
&+ \frac{e^2 \tau_{bulk\ d_{xz}}}{2} \sqrt{\frac{m_H}{m_L}} \frac{\frac{1}{2} g \mu_B H}{\pi \hbar^2} \frac{2 \left(\sum_{bulk\ t_{2g}} D^\downarrow(\varepsilon_F) - \sum_{bulk\ t_{2g}} D^\uparrow(\varepsilon_F) - D^\uparrow_{IF}(\varepsilon_F) \right)}{\sum_{bulk\ t_{2g}} D^\downarrow(\varepsilon_F) + \sum_{bulk\ t_{2g}} D^\uparrow(\varepsilon_F) + D^\uparrow_{IF}(\varepsilon_F)} \\
&+ \frac{e^2 \tau_{bulk\ d_{yz}}}{2} \sqrt{\frac{m_L}{m_H}} \frac{\frac{1}{2} g \mu_B H}{\pi \hbar^2} \frac{2 \left(\sum_{bulk\ t_{2g}} D^\downarrow(\varepsilon_F) - \sum_{bulk\ t_{2g}} D^\uparrow(\varepsilon_F) - D^\uparrow_{IF}(\varepsilon_F) \right)}{\sum_{bulk\ t_{2g}} D^\downarrow(\varepsilon_F) + \sum_{bulk\ t_{2g}} D^\uparrow(\varepsilon_F) + D^\uparrow_{IF}(\varepsilon_F)} \quad (5.35)
\end{aligned}$$

After cancelling the bulk t_{2g} $D^\downarrow(\varepsilon_F)$ with the bulk t_{2g} $D^\uparrow(\varepsilon_F)$, we obtain:

$$\begin{aligned}
& \sigma^{xx}(H \neq 0) - \sigma^{xx}(H = 0) \\
&= \frac{e^2 \frac{1}{2} g \mu_B H}{2} \frac{2 \left(\begin{aligned} & \tau_{IF} \sum_{bulk\ t_{2g}} D^\downarrow(\varepsilon_F) - \tau_{bulk\ d_{xy}} D^\uparrow_{IF}(\varepsilon_F) - \\ & \sqrt{\frac{m_H}{m_L}} \tau_{bulk\ d_{xz}} D^\uparrow_{IF}(\varepsilon_F) - \sqrt{\frac{m_L}{m_H}} \tau_{bulk\ d_{yz}} D^\uparrow_{IF}(\varepsilon_F) \end{aligned} \right)}{\sum_{bulk\ t_{2g}} D^\downarrow(\varepsilon_F) + \sum_{bulk\ t_{2g}} D^\uparrow(\varepsilon_F) + D^\uparrow_{IF}(\varepsilon_F)} \quad (5.36)
\end{aligned}$$

Using equation (5.9), we obtain:

$$\begin{aligned}
& \sigma^{xx}(H \neq 0) - \sigma^{xx}(H = 0) \\
& 2 \left(\begin{array}{l} \tau_{IF} \left(\frac{m_L}{2\pi\hbar^2} + 2 \frac{\sqrt{m_L m_H}}{2\pi\hbar^2} \right) - \tau_{bulk\ d_{xy}} \frac{m_L}{2\pi\hbar^2} \\ - \sqrt{\frac{m_H}{m_L}} \tau_{bulk\ d_{xz}} \frac{m_L}{2\pi\hbar^2} - \sqrt{\frac{m_L}{m_H}} \tau_{bulk\ d_{yz}} \frac{m_L}{2\pi\hbar^2} \end{array} \right) \\
& = \frac{e^2 \frac{1}{2} g \mu_B H}{2} \frac{3 \frac{m_L}{2\pi\hbar^2} + 4 \frac{\sqrt{m_L m_H}}{2\pi\hbar^2}}{\pi\hbar^2} \\
& 2 \left(\begin{array}{l} (\tau_{IF} - \tau_{bulk\ d_{xy}}) \frac{m_L}{2\pi\hbar^2} + (\tau_{IF} - \tau_{bulk\ d_{xz}}) \frac{\sqrt{m_L m_H}}{2\pi\hbar^2} \\ + \left(\tau_{IF} - \frac{m_L}{m_H} \tau_{bulk\ d_{yz}} \right) \frac{\sqrt{m_L m_H}}{2\pi\hbar^2} \end{array} \right) \\
& = \frac{e^2 \frac{1}{2} g \mu_B H}{2} \frac{3 \frac{m_L}{2\pi\hbar^2} + 4 \frac{\sqrt{m_L m_H}}{2\pi\hbar^2}}{\pi\hbar^2} \tag{5.37}
\end{aligned}$$

A positive linear magnetoresistance is:

$$\begin{aligned}
\rho(H) - \rho(0) &= \frac{1}{\sigma(H)} - \frac{1}{\sigma(0)} = \frac{1}{\sigma(0)} \left(\frac{1}{\left(1 + \frac{\sigma(H) - \sigma(0)}{\sigma(0)}\right)} - 1 \right) \\
&\approx -\frac{1}{\sigma(0)^2} (\sigma(H) - \sigma(0)) > 0 \tag{5.38}
\end{aligned}$$

The condition to make $\sigma^{xx}(H \neq 0) - \sigma^{xx}(H = 0) < 0$ is

$$\tau_{IF} < \tau_{bulk\ d_{xy}}, \quad 2\tau_{IF} < \tau_{bulk\ d_{xz}} + \frac{m_L}{m_H} \tau_{bulk\ d_{yz}} \approx \tau_{bulk\ d_{xz}} \tag{5.39}$$

Considering strong scattering at interface, which is enhanced due to FM alignment of the vacancy-related moments and d_{xy} 2DEG, it is highly possible that this condition can be satisfied. Therefore, we argue that the proximity-induced-Zeeman effect from the magnetic insulator EuO is the origin of the positive LMR in our system.

Chapter 6 The LaAlO₃/SrTiO₃ Quantum Well

In this chapter, we discuss a different application of the confined 2DEG in SrTiO₃: the creation of quantum well (QW) states. Experimentally, LaAlO₃/SrTiO₃ (LAO/STO) quantum wells (QW) are grown by molecular beam epitaxy (MBE) in our lab at the University of Texas at Austin. The electronic structure and particularly the band alignment is analyzed by *in-situ* X-ray photoemission in our lab and electron energy loss spectroscopy (EELS) in the Oak Ridge National Lab. Using density function theory, we examine the density of states (DOS) of confined t_{2g} 2DEG in the LAO/STO heterostructure. We compute the band offset of the heterostructure, investigate the orbital character of conduction states, and identify their features corresponding to the QW states. In addition, we model the EELS spectrum using first-principle calculations by adopting the Z+1 approximation and considering the core-hole effect. Site-projected unoccupied p and d DOS are extracted and compared with the experimental O K and Ti L edges that correspond to $1s$ to $2p$ and $2p$ to $3d$ transitions, respectively. We find that in the LAO/STO QW, there are evanescent Ti-originated states in the LAO layer and relate them with the peak in the EELS spectrum. We show that the LaAlO₃/SrTiO₃ system could potentially be a good candidate for QW device applications.

6.1 COMPUTATIONAL DETAILS

We use the Vienna *ab initio* simulation package (VASP) code to carry out the calculations [30,31]. The exchange-correlation functional is approximated within the local density approximation (LDA) and projection augmented wave (PAW) pseudopotentials are used) [19,28]. The electronic configurations for each element are as follows: $5s^2 5p^6 5d^1 6s^2$ for La, $3s^2 3p^1$ for Al, $2s^2 2p^4$ for O, $4s^2 4p^6 5s^2$ for Sr, and $3s^2 3p^6 3d^2 4s^2$ for Ti. The cutoff energy of 700 eV is chosen and an

$8 \times 8 \times 8$ k -point mesh is selected to achieve the Brillouin zone integration convergence, for both bulk STO and LAO [29]. Bulk structures are optimized first and the lattice constants are found to be 3.86\AA and 3.74\AA for STO and LAO, respectively. This is typical of LDA calculations to have the lattice constant slightly smaller when compared with experiment as the calculation is done at zero Kelvin and LDA tends to over-bind. The spin-orbit interaction is not included. For the quantum well, we construct a $(\text{LAO})_{4.5}/(\text{STO})_{5.5}$ supercell with the $\text{LaO}^+/\text{TiO}_2$ interfaces on both sides. We take the LAO as the substrate and use the theoretical $a_{\text{LAO}} = 3.74 \text{ \AA}$ as the in-plane lattice constant. A 1×1 lateral cell dimension is adopted. All atomic positions were fully relaxed until residual forces were less than 0.01 eV \AA^{-1} . We sampled the Brillouin zone with $8 \times 8 \times 1$ Monkhorst-Pack k -point grids for self-consistent calculation.

The main method we use is the analysis of the layer-resolved DOS that is projected onto different elements and orbitals. In this way, we can analyze the composition of the electronic states and their behavior in real space. Therefore, to ensure the accuracy of the spectrum, a $16 \times 16 \times 16$ and a $16 \times 16 \times 1$ k -point meshes are used for the bulk and supercell accurate DOS calculation, respectively. The accuracy was checked further with a finer $32 \times 32 \times 32$ k -point mesh. Due to symmetry, we only need to consider a half of the simulation cell along the z axis. The simulation cell is shown in Figure 6.1.

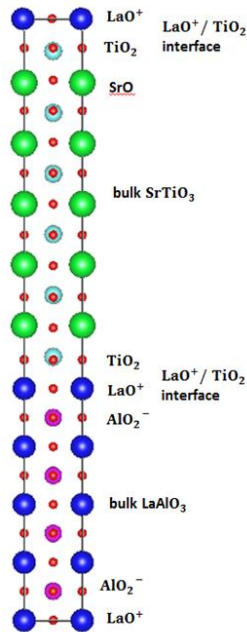


Figure 6.1. A $(\text{LAO})_{4.5}/(\text{STO})_{5.5}$ simulation cell with two symmetric n-type interfaces.

In the EELS experiment, a core-electron excitation leaves a hole in the inner core shell, resulting in a change in the electrostatic screening of the nucleus and the effective potential felt by remaining electrons. This is usually referred to as a “core-hole effect,” and it can be approximately accounted for in the so-called $Z+1$ approximation, where the excited atom can be substituted by an atom of the element with the next higher atomic number. With the dipole selection rule, O K edge in STO and LAO corresponds to a $1s \rightarrow 2p$ excitation at oxygen sites, while Ti L_2/L_3 edge is related to a $2p \rightarrow 3d$ process. Therefore, O and Ti at specific sites in the QW structure are replaced with fluorine and vanadium, and after a self-consistent calculation, locally-projected unoccupied p and d DOS are extracted, to be compared with the experimental O K and Ti L_2/L_3 edges. The electronic structure of F and V are $2s^2 2p^5$ and $3s^2 3p^6 3d^3 4s^2$, and we use Gaussian broadening of 0.7 eV to make the projected DOS (PDOS) look smoother.

6.2 BULK DENSITY OF STATES OF SrTiO_3 AND LaAlO_3

We focus on bulk STO first. Figure 6.2 below shows the DOS projected onto SrO and TiO_2 planes. The conduction band edge mostly comes from the TiO_2 layer. In Figure 6.3(a) we show the DOS projected onto Sr, Ti and O. The antibonding Ti 3d t_{2g} band is found around 2.0 eV above the valence band top energy. Meanwhile, the Sr states start around 5.0 eV, overlapping with the Ti e_{2g} band. The oxygen states mainly form the top of the valence band, but are also found in the conduction band in the same region as Ti states due to p-d hybridization. However, the density is low and we have to zoom in to see more details (see figure 6.3(b)).

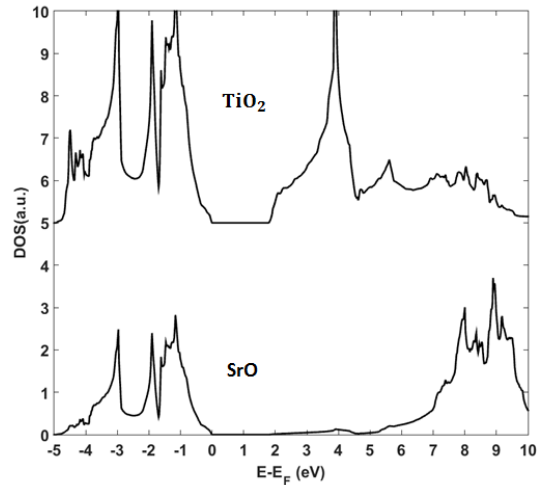


Figure 6.2. Total DOS of bulk STO projected onto TiO_2 and SrO layers. Zero of energy is set at the top of the valence band.

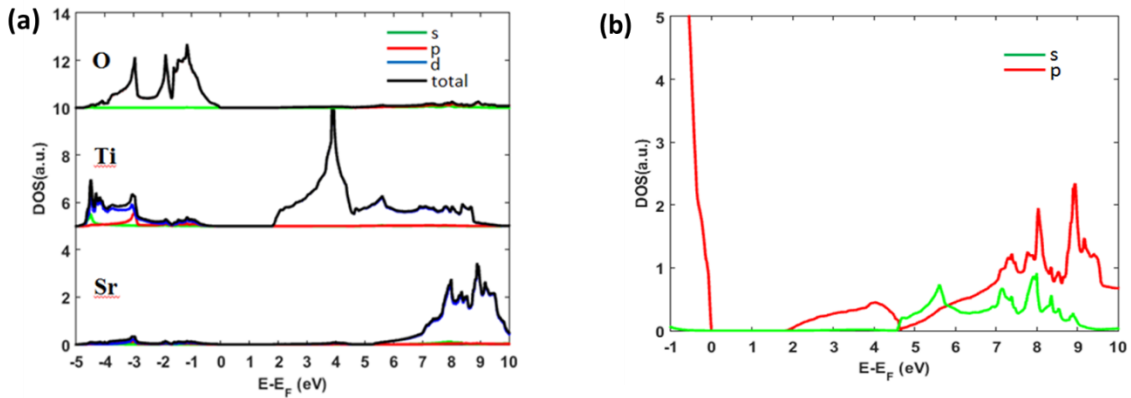


Figure 6.3. (a) PDOS for Sr, Ti and O atoms individually. (b) Magnified PDOS of O atoms ($10\times$).

Next, we consider bulk LAO. We show the DOS projected onto the LaO and AlO_2 layers in Figure 6.4(a). The LaO layer plays the dominant role at the edge of the conduction band as can be seen from the prominent La peak in Figure 6.4(b). This peak has a significant f component and a relatively small d component. But above 5.0 eV, the states are composed almost entirely of the La d -orbitals. Here bonding is between La and O atoms and Al appears to be in the ionic limit.

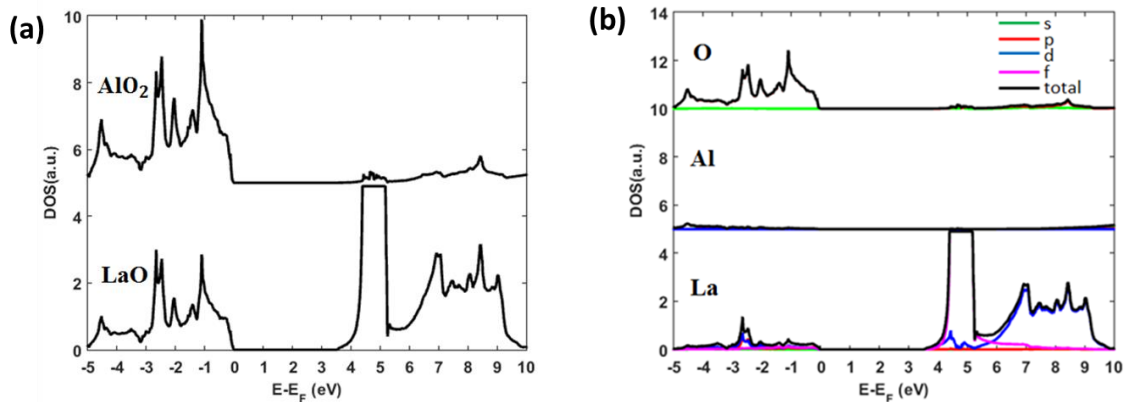


Figure 6.4. (a) Total DOS of bulk LAO projected onto AlO_2 and LaO layers. Zero of energy is set at the top of the valence band. (b) PDOS of bulk La, Al and O atoms individually.

6.3 BAND OFFSET AND ORBITAL ANALYSIS FOR SrTiO₃/LaAlO₃ SUPERCELL

We show the total DOS of a QW structure projected layer-by-layer in Figure 6.5 (a). The valence-band offset between LAO and STO is -0.2eV and this is in agreement with previous calculations. Albina *et al.* report a valence-band offset of -0.3eV~-0.4eV, with the same DOS approach by comparing valence band edges [152]. Using the reference potential method, Lee and Demkov found a -0.1 eV valence-band offset [153]. Pentcheva and Pickett calculated the band offset using the difference between the O-1s core level in bulk-like regions of two oxides. With the energy difference from the valence band top and core level in bulk, they obtain a band offset of -0.15eV [154].

Due to the inability of the LDA to give a correct band gap, the conduction band offset taken directly from the calculation is not reliable. We first use the metal-induced gap states (MIGS) model to estimate the conduction band offset [155,156]. In this model, the conduction band offset between two semiconductors is given by $\phi = (\chi_a - \Phi_a) - (\chi_b - \Phi_b) + S(\Phi_a - \Phi_b)$, where χ is the electron affinity, Φ is the charge neutrality level (CNL) measured from vacuum level, and S is the pinning parameter of the wider-gap semiconductor. If $S = 1$, the offset is given by a difference in electron affinities, which is called the Schottky limit and no pinning happens. On the other hand, when $S = 0$, the strong pinning controls the charge neutrality level line up and this is called the Bardeen limit. Generally, the pinning parameter can be estimated by an empirical formula: $S = \frac{1}{1+0.1(\epsilon_\infty-1)^2}$ [157], where ϵ_∞ is the high frequency component of the dielectric constant. The electron affinities of STO and LAO are 3.9 and 2.5 eV, respectively [157,158]. The CNL is the Fermi level of the ideal surface and is associated with the branch point of the complex band structure of the bulk. It can also be calculated using the bulk Green's function [159]. Demkov and co-workers estimated the CNL of STO to be 5.9 eV below the vacuum level by adopting the complex band structure

method [160], while Peacock and Robertson obtained the CNL of LAO to be 3.8 eV above the valence band maximum, or 4.3 eV below vacuum level from shifted LDA bands [158], considering the experimental band gaps of STO and LAO are 3.2 and 5.6 eV. Thus, in the Schottky limit, the conduction band offset between STO and LAO is -1.4 eV while in the Bardeen limit, the CBO is 0.2 eV. Actually, Peacock and Robertson also gave an approximated S value as 0.53 [158] and with this, CBO is calculated as -0.85 eV. It is interesting to point out that through pure serendipity this is close to our value of -1.25eV from the DOS analysis.

As the f -peak in LaO is very large it dominates all other states making the visualization hard, therefore, we remove the f component in LAO in Figure 6.5(b). If one looks at the energy window from 0 to 1eV, the gap states appear in the interface LaO layer but then vanish quickly, deeper in the LAO bulk. These states have mainly d -character and they are STO-originated Ti- d evanescent states as they decay very fast away from the interface. The complex band structures of La_2O_3 , $\alpha\text{-Al}_2\text{O}_3$ and STO suggest the decay lengths of 3.6, 2.8 and 2.0 Å, respectively [160]. This is consistent with the situation at the STO/LAO interface.

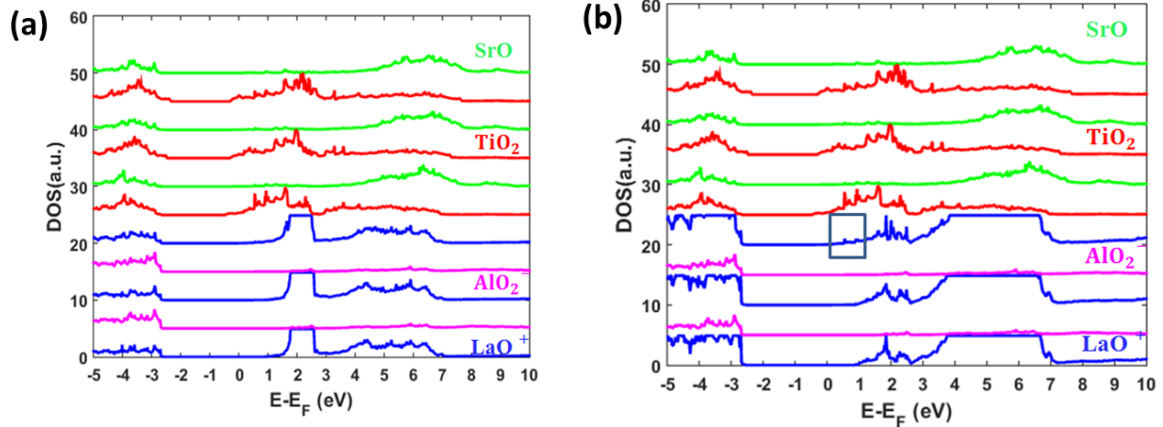


Figure 6.5 (a). Total DOS of the LAO/STO QW, layer by layer. (b) Total DOS of QW, layer by layer without La *f* components. DOS on 3 LaO layers are magnified by 5 times to show evanescent states, which is highlighted by square box.

To compare with the measured EELS O K edge (that records the dipole transition magnitude from O *1s* \rightarrow *2p*), we calculate the O-*p* PDOS in a QW layer by layer. The result is shown in the left of Figure 6.6. Clearly, the *p*-states within the energy range from 0 to 1eV are located only in the LaO layer at the interface. Compared with the EELS spectrum on the right, these states may correspond to peak *a* as the height decreases gradually and disappears eventually when it goes to bulk LAO. This effect is more evident from p-type interface side. Nevertheless, peak *a* disappears completely within two LaO layers (a unit cell) in experiment, while in the calculation one layer (half a unit cell) is enough for it to decay.

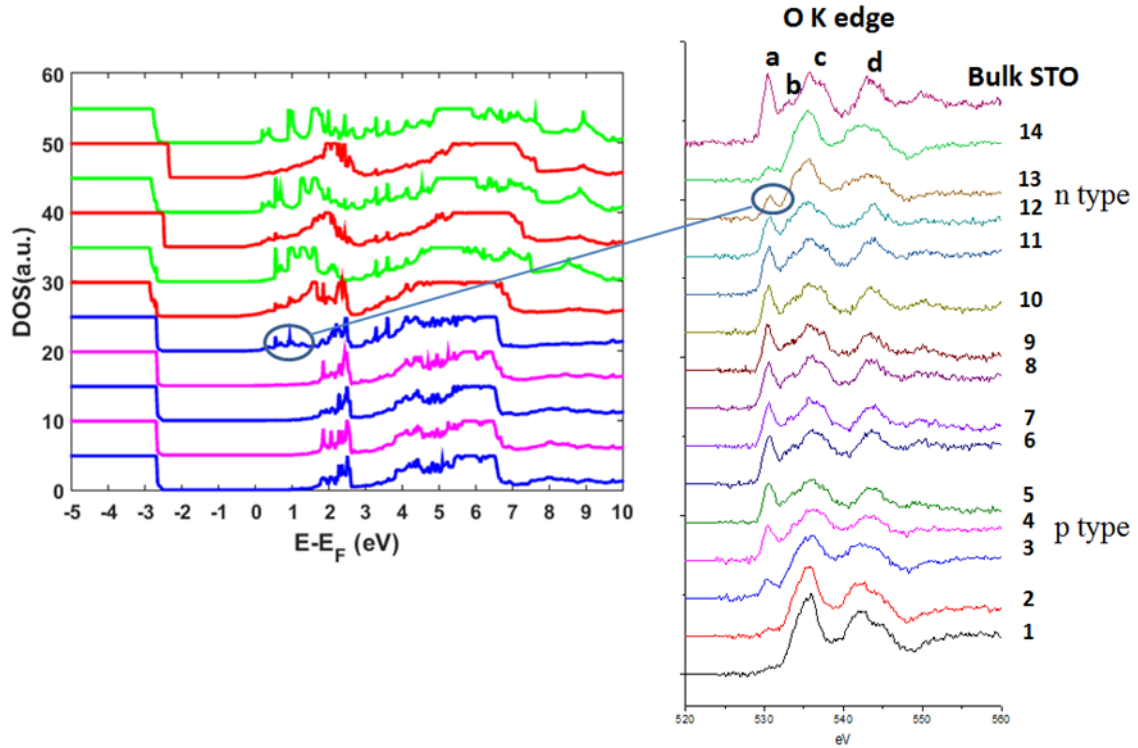


Figure 6.6. p -PDOS of QW, layer by layer and experimental EELS O K edge.

It is well known that a two-dimensional electron gas (2DEG) may form at the n-type LAO/STO interface and electrons occupy the Ti- d states [92]. Therefore, it is of interest to look at the orbital composition of the states near the Fermi level in the well. In Figure 6.7 we show the Ti- d DOS projected onto three different layers going from the interface to the bulk. At the interface, the occupied d -states are mainly d_{xy} orbitals, and further away from interface, d_{xy} and d_{yz}/d_{xz} contributions are almost equal to each other.

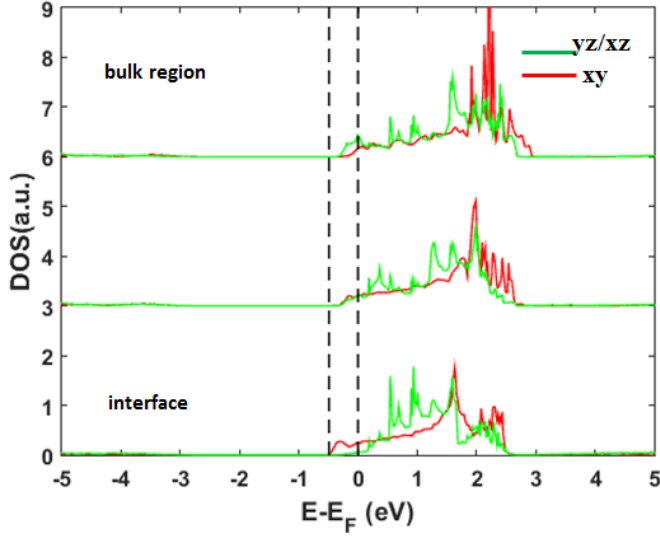


Figure 6.7. Ti- d PDOS of QW, layer by layer.

Finally, for the most bulk-like layer, the contribution of the d_{yz}/d_{xz} is larger than d_{xy} . We can get a direct view of the 2DEG, by plotting the 3D charge density projected on the occupied conduction bands (from -0.5eV to 0 in Figure 6.8(a)). The d_{xy} character of the charge distribution in the interface layer is clearly seen. Also, in Figure 6.8(b) we show a cut through the charge distribution with an yz/xz plane. The distinctively d_{yz}/d_{xz} -like character is observed in the bulk region. Furthermore, if we set the density range to a relatively low value, even the evanescent states in the LaO layer could be captured, though it is a little hard to see (Figure 6.8(c)). From the DOS (Figure 6.8(d)) we conclude that the evanescent state is a combination of the f and d states. The d -states have the d_{xy} character (not the d_{yz}/d_{xz}) suggesting that this is a decaying state of the STO 2DEG. It should be pointed out that the charge itself is due to the stoichiometry of the well (it has one extra TiO_2 plane) and not due to a polar catastrophe or doping.

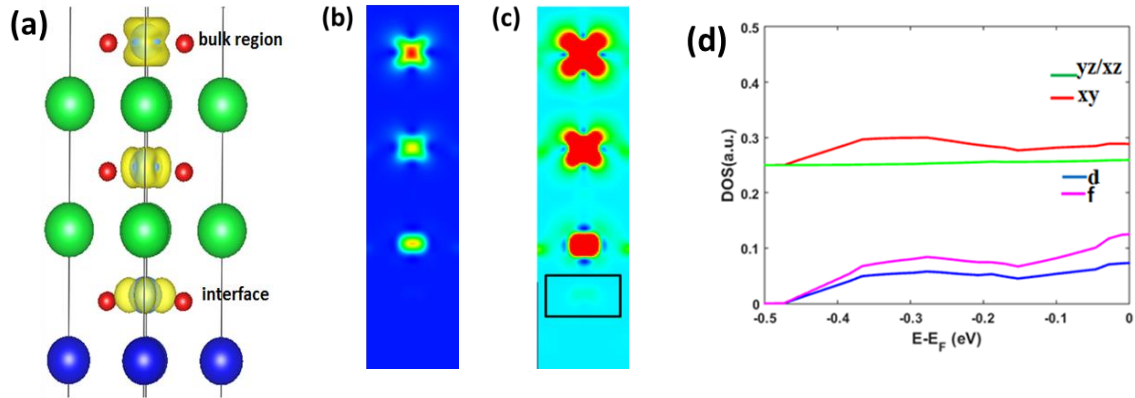


Figure 6.8. (a) 3D charge density of electron gas. (b) 2D yz plane of the electron gas (c) Same as Figure 8(b). Color bar range is from [0, 10%]. (d) PDOS of evanescent states highlighted by square box in Figure 6.8(c).

6.4 EELS MODELING FOR SrTiO₃/LaAlO₃ SUPERCCELL

Figure 6.9 below shows the Z+1 approximation results for the O K edge in bulk STO computed with different cell sizes. At the site of interest, oxygen is replaced by fluorine. Zero energy is set at the Fermi level and the bulk sample experimental result is in the top panel for comparison. Here, we align the first peak for all data, as we are mostly interested in the peak separation. From the figure, we can see the three main peaks within the 15 eV energy range in good agreement with experiment. Overall, the peak position and separation looks reasonable even for the smallest simulation cell. Theoretically, results appear to converge with the cell size (the larger the cell the better the k-point sampling). The peak separation however, appears to be consistently underestimated. However, this may be a matrix element effect. Also, we will need to average the PDOS computed for different oxygen atoms in the same plane. As you can see the degeneracy is lifted in the p -shell, but this is because this is just one atom.

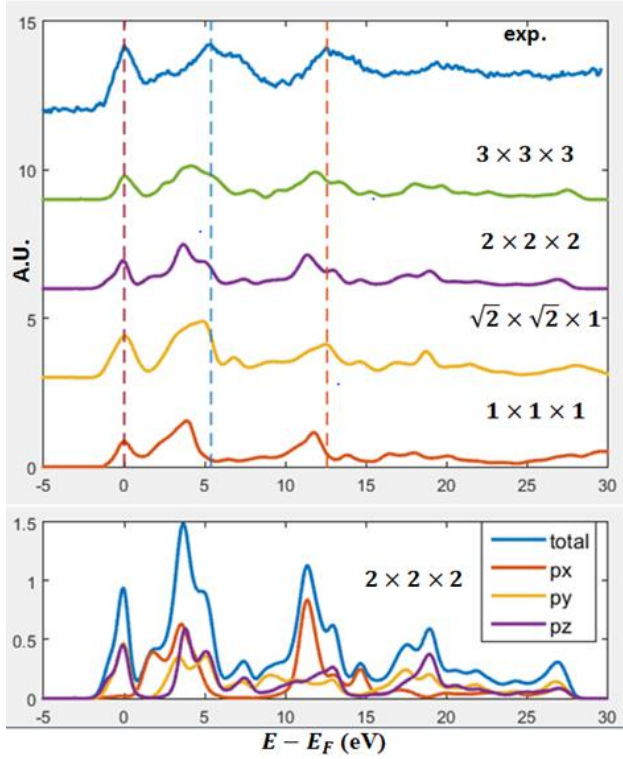


Figure 6.9. Computed O K edge spectrum in bulk SrTiO_3 as a function of the simulation cell size.

Next we show the $Z+1$ approximation results for the Ti L_2/L_3 edges in figure 6.10. The zero energy is set to the Fermi level and the first peak is aligned to experiment. We should point out that in the experimental data there are four peaks, of which two are L_2 and the other two are L_3 peaks. This is due to the spin-orbital coupling and initial states for L_2 and L_3 peaks are $2p^{1/2}$ and $2p^{3/2}$. In our calculation, the spin-orbital coupling is not considered, which results in a double degeneracy of our peaks. We can see that a $3 \times 3 \times 3$ cell gives results that are closest to experiment as two peaks are almost at the same position. The height of corresponding peaks in experiment looks different as it is influenced by the matrix element $|\langle \varphi_i | \mathbf{p} | \varphi_f \rangle|^2$, while in calculation it is only the density of states. From the crystal field theory, we know that the Ti d states will be split

into two levels due to octahedral cubic environment. At the bottom of Figure 6.10, we show the decomposed results of L_2/L_3 edges. The e_g and t_{2g} peaks are well separated and the crystal field splitting is approximately 2.4 eV.

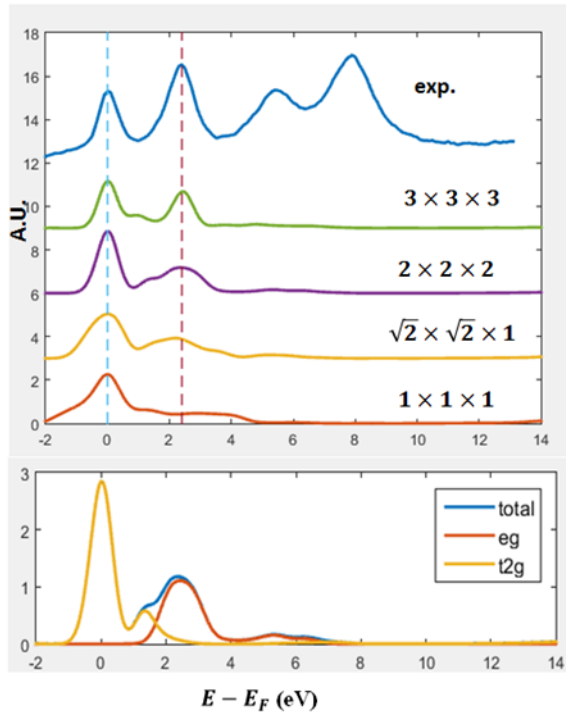


Figure 6.10. Computed Ti L_2/L_3 edge in bulk SrTiO_3 .

We also have the results for the O K edge in bulk LaAlO_3 . As there is no directly related experimental data, we take the LaAlO_3 layer furthest from the interface in the quantum well structure, as reference. The result is shown in figure 6.11 below.

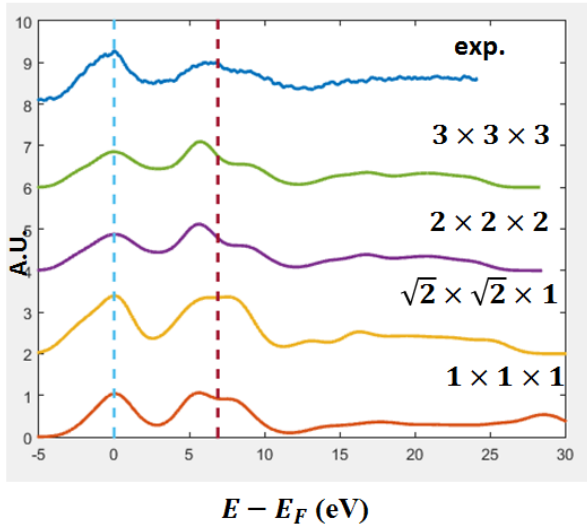


Figure 6.11. Computed oxygen K edge spectrum in bulk LaAlO_3 as a function of the simulation cell size (2.0 eV broadening is applied). Experimental data is shown in the top panel for comparison.

As shown above, the bulk cell with the $\sqrt{2} \times \sqrt{2}$ lateral dimensions allows to model L_2/L_3 edge accurately. Therefore, results for the $\sqrt{2} \times \sqrt{2}$ cell of $\text{LAO}_{4.5}/\text{STO}_{5.5}$ QW will be demonstrated in the following. Results of L_2/L_3 edge are shown in figure 6.12. Because the spectrum for each layer comes from an independent calculation, there exists a problem of alignment. Nevertheless, since there is only one substitution out of 200 atoms, the valence band maximum (VBM) shouldn't change significantly though substitution occur at different layers. We check the VBM of the total DOS for each calculation and the band offset is indeed at most 0.1 eV. Thus we align the VBM of three spectra and then shift them as a whole to match the position of the experimental peaks. In the experiment, spectra don't vary a lot from the interface to the bulk region and this also happens in our calculation.

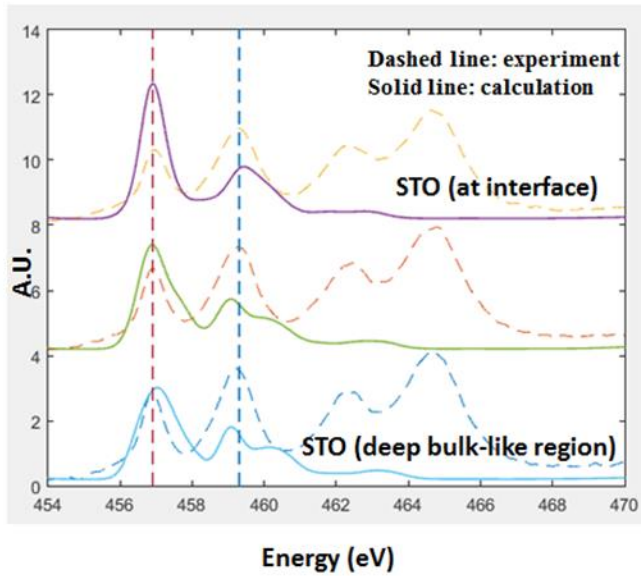


Figure 6.12. Computed L_2/L_3 edge in the QW structure.

In Figure 6.13(a) we show the results for the O K edge. It is well known that LDA couldn't give a correct band gap and this problem becomes even worse when we use fluorine instead of oxygen. Figure 6.13(b) is the p-PDOS spectra of non-fluorine system and though band gap is not correct, we can easily tell the difference between LAO and STO band gaps. However, once fluorine is added, the difference in the band gap becomes pretty small. Thus we couldn't get the conduction band offsets directly from calculation and had to shift the LAO part manually to make up for the band gap difference.

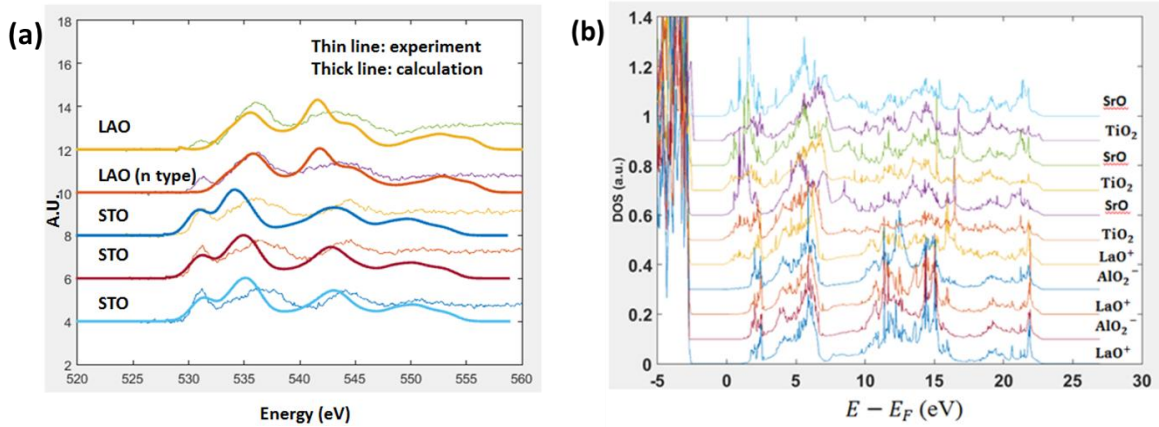


Figure 6.13. (a) O K edge for the LAO/STO QW heterostructure (broadening of 2.0 eV is applied). Thick solid lines are calculated and thin lines are experiment. (b) p-PDOS for the LAO/STO QW heterostructure layer by layer.

In the $Z+1$ approximation, even for the independent calculation, the VBM is almost the same (valence band offset is at most 0.2 eV). Experimentally, the valence band offset is around 0.1 eV [161] and in real experiment the LAO band gap is 5.6 eV and that of STO is 3.2 eV. So we shifted LAO spectra to the right by 2.3 eV and then shift all calculated spectra until the first peak in the calculation aligns with the peak in experiment.

In Figure 6.13(a), three peaks in STO part agrees with experiments well, just as in the bulk case while for the LAO part, apart from two peaks shown in bulk case, there is still one peak in front of the edge, which is not very clear in calculation. A possible explanation is that this peak comes from surface state from STO side. However, we didn't capture that in our calculation. Another possible reason is that it is due to the diffusion of Ti atoms into the LAO region. Actually we can see the gradual decay of this peak when it is further away from the interface and this is more significant from the p-type interface side as there is one more layer of LAO.

In conclusion, we use density functional theory and $Z+1$ approximation to model the EELS spectra of STO/LAO heterostructures. We modelled the O K and L_2/L_3 edges for bulk STO, and O K edge for bulk LAO and identified the EELS peaks and their orbital composition. The cell's size effect is also investigated. We then performed similar analysis for a SrTiO₃/LaAlO₃ heterostructure. However, due to the limitations of the LDA, we couldn't obtain the correct conduction band offset, which had to be included *ad hoc*. There is also one peak in the LAO O K edge structure that is out of expectation from calculation and it might be explained as diffusion of Ti atoms. Overall the calculation reproduces the experimental results reasonably well.

6.5 QUANTUM WELL STATES IN SrTiO₃/LaAlO₃ SUPERCELL

In Chapter 4 we have discussed several properties of the 2DEG in transition metal oxide heterostructures. Here we talk about a different application of the confined 2DEG in SrTiO₃: the creation of quantum well (QW) states. Lin *et al.* has explored the possibility of creating QW states in SrO/STO/SrO heterostructures with density functional theory and tight-binding model [162]. As introduced in Section 5.3, the energy dispersion along k_x and k_y of the three t_{2g} states has the trigonometric function form. However, For the Ti d_{xy} -derived band, the dominant bonding is along x and y direction, while coupling along the z direction is weak. Therefore, if STO is confined in the z direction, the d_{xy} -spectrum is only slightly modified and change of the d_{xy} density of states (DOS) profile is negligible. However, for the Ti d_{xz}/d_{yz} -derived bands, since coupling along the z direction is strong, the z -direction confinement will modify the d_{xz}/d_{yz} -spectrum strongly. According to the tight-binding model analysis [162], sharp peaks will rise in the d_{xz}/d_{yz} density of states (DOS) profile. These peaks correspond to different levels of quantum well states and the number of peaks depends on the STO thickness.

Therefore, we only focus on DOS of the d_{xz}/d_{yz} -derived bands and count energy spacing between the sharp peaks as the observed absorption energy.

We vary symmetric QWs composition from $(\text{LAO})_{7.5}/(\text{STO})_{3.5}$ to $(\text{LAO})_{7.5}/(\text{STO})_{5.5}$, which correspond to three-, four-, and five-u.c. QWs in experiment, respectively. In Figure 6.14(a), we plot the calculated density of states (DOS) for three-, four-, and five-u.c. QW heterostructures. The energy differences between the ground state and the first-excited state peaks in the DOS are 510 meV, 420 meV and 350 meV for three-, four-, and five-u.c. QWs, respectively. DFT results for the five-u.c. QW agree closely with our experiment while the calculated energy spacing of the three- and four-u.c. QWs are about 0.1 eV smaller than the observed peaks in our experiment [163].

In Figure 6.14(b), we plot the charge density of the QW subbands for an $(\text{LAO})_{7.5}/(\text{STO})_{4.5}$ QW in real space. The excess charge is introduced into the STO conduction band automatically via the symmetric interfaces, analogous to the n -type La doping in the experimental structures. In the figure, the nodal character of each subband is illustrated to the right of each sub-panel, indicating the shape of the corresponding wave function in real space. The nodal structure in our calculations is consistent with that of the QW wave functions, with the charge density varying sinusoidally between neighboring Ti atoms. The correspondence between the expected charge density for the QW states and the calculated charge density in our structures supports our claim that the sharp features we have calculated in the DOS of the STO conduction band are indeed the QW states we hope to probe via absorption measurements and the spacing between the adjacent peaks corresponds to the intersubband absorption energy in the real system.

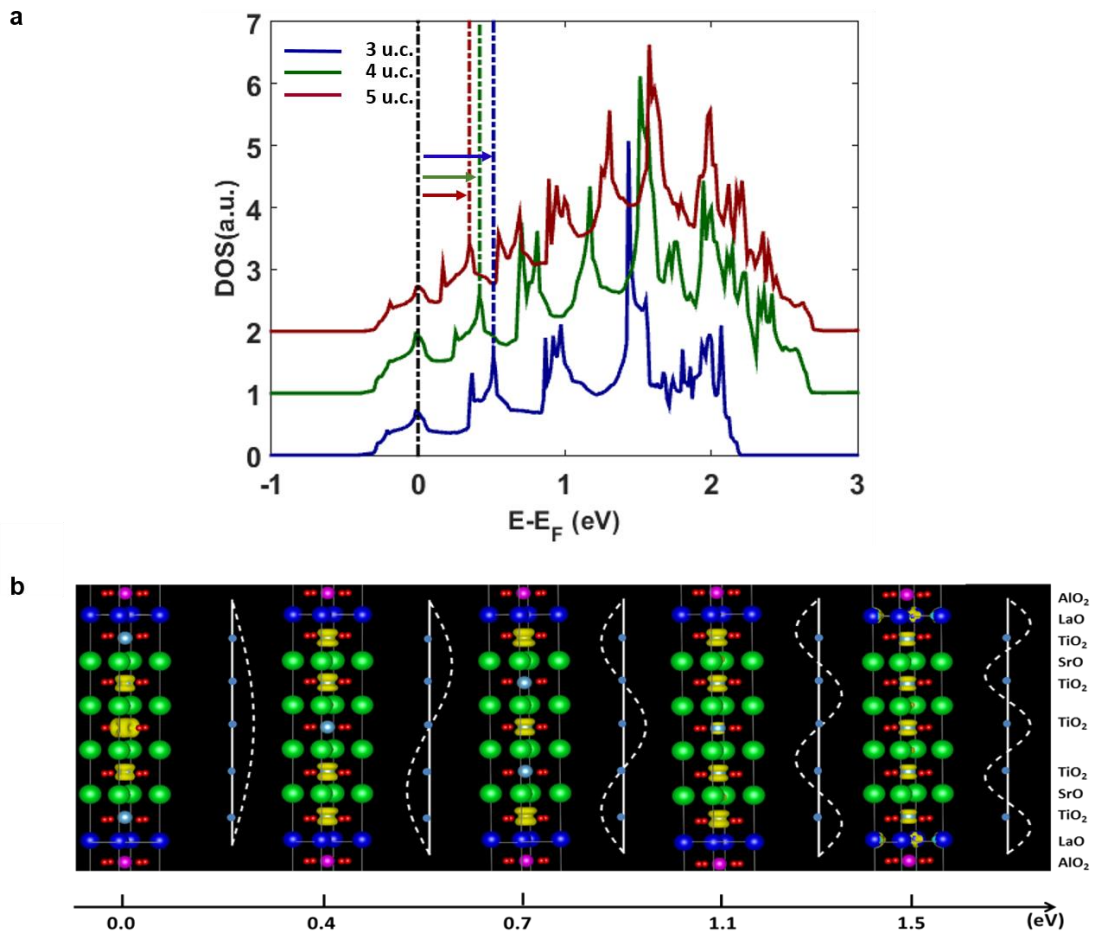


Figure 6.14. Density functional theory calculations of quantum well states. (a) The calculated density of states (DOS) displaying the sum of $d_{xz/yz}$ states for three-, four-, and five-u.c. QW structures. The red, green, and blue arrows indicate the transition energy between the ground state and first-excited state in five-, four-, and three-u.c. QWs, respectively. (b) Charge distribution in real space corresponding to the five QW subbands in an $(\text{LAO})_{7.5}/(\text{STO})_{4.5}$ cell. The energy of each state is labeled below the figure. Each plot is accompanied with its schematic wave function on the right. The width of each state is 0.2 eV. La, Al, Sr, Ti, and O atoms are colored as dark blue, magenta, green, light blue and red, respectively.

As explained in several theoretical reports about the STO/LAO system [154,164,165], in an asymmetric supercell with both n - and p -type interfaces, polar nature of LAO will induce an electric field inside LAO, and this will cause a

potential drop throughout LAO layers. Due to the periodic boundary condition limit in DFT calculation, in the supercell, the potential at top LAO layer should be the same as the bottom STO layer. As a result, to cancel the potential drop in LAO part, an electric field is automatically formed in STO region. This does not accurately model the reality in a doped-LAO/STO system, as the high electron doping density within the STO quantum wells will screen the electric field. Therefore, a symmetric supercell is reasonable, as it would introduce the n-type doping automatically, and avoid the formation of an electric field across the STO region. However, we also model the asymmetric $(\text{LAO})_7/(\text{STO})_4$ supercell, which is exactly the same as we use in experiment. The calculated DOS is presented in Figure 6.15: Four QW peaks can be clearly seen, in both undoped and La-doped supercells. The electric field in STO is 0.035 eV/\AA , which is contributed by formal ionic charges of $(\text{LaO})^+$ and $(\text{AlO}_2)^-$ planes, and the polarization inside SrTiO_3 and LaAlO_3 . This demonstrates that the QW states also form in the asymmetric LAO/STO supercell, and supports our claim of intersubband transitions in LAO/STO QWs.

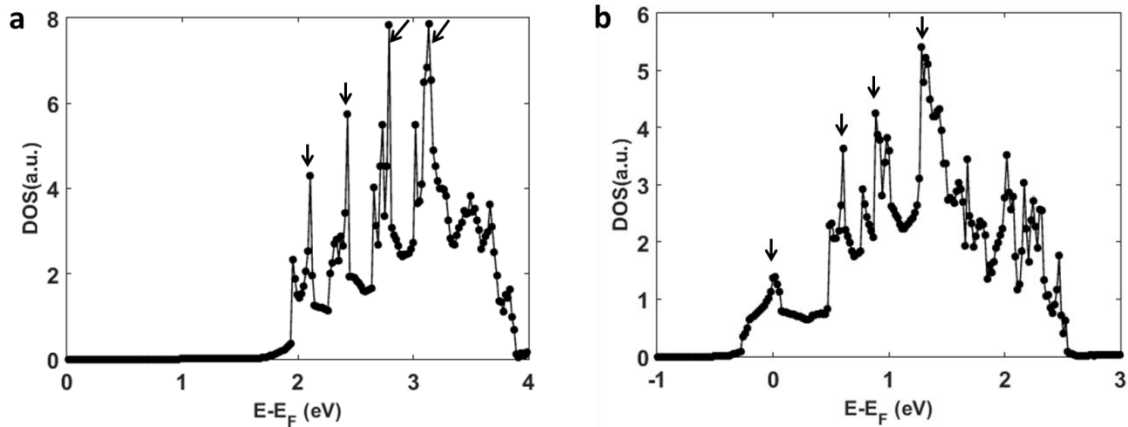


Figure 6.15. The calculated density of states (DOS) displaying the sum of $d_{xz/yz}$ states for stoichiometric (asymmetric) QW structures. (a) Pure $(\text{LAO})_7/(\text{STO})_4$ cell. (b) La doped $(\text{LAO})_7/(\text{STO})_4$ cell. Each QW state peak is denoted by the black arrow.

References

- [1] P. Zubko, S. Gariglio, M. Gabay, P. Ghosez, and J.-M. Triscone, *Annu. Rev. Condens. Matter Phys.* **2**, 141 (2011).
- [2] B. M. Hudak, S. W. Depner, G. R. Waetzig, A. Talapatra, R. Arroyave, S. Banerjee, and B. S. Guiton, *Nat. Commun.* **8**, 15316 (2017).
- [3] F. W. Lytle, *J. Appl. Phys.* **35**, 2212 (1964).
- [4] H. Thomas and K. A. Müller, *Phys. Rev. Lett.* **21**, 1256 (1968).
- [5] G. Shirane and Y. Yamada, *Phys. Rev.* **177**, 858 (1969).
- [6] K. A. Müller and H. Burkard, *Phys. Rev. B* **19**, 3593 (1979).
- [7] Y.-Y. Pai, A. Tylan-Tyler, P. Irvin, and J. Levy, *Rep. Prog. Phys.* **81**, 036503 (2017).
- [8] A. A. Demkov and A. B. Posadas, *Integration of Functional Oxides with Semiconductors* (2014).
- [9] A. S. Foster, F. Lopez Gejo, A. L. Shluger, and R. M. Nieminen, *Phys. Rev. B - Condens. Matter Mater. Phys.* **65**, 1741171 (2002).
- [10] M. Born and R. Oppenheimer, *Ann. Phys.* **389**, 457 (1927).
- [11] D. R. Hartree, *Math. Proc. Cambridge Philos. Soc.* **24**, 426 (1928).
- [12] V. Fock, *Zeitschrift F♦r Phys.* **61**, 126 (1930).
- [13] L. H. Thomas, *Math. Proc. Cambridge Philos. Soc.* **23**, 542 (1927).
- [14] E. Fermi, *Rend. Accad. Naz. Lincei* **6**, 602 (1927).
- [15] P. A. M. Dirac, *Math. Proc. Cambridge Philos. Soc.* **26**, 376 (1930).
- [16] P. Hohenberg and W. Kohn, *Phys. Rev.* **136**, B864 (1964).
- [17] R. M. Martin, *Electronic Structure : Basic Theory and Practical Methods* (Cambridge University Press, 2004).
- [18] D. M. Ceperley and B. J. Alder, *Phys. Rev. Lett.* **45**, 566 (1980).
- [19] J. P. Perdew and A. Zunger, *Phys. Rev. B* **23**, 5048 (1981).
- [20] A. D. Becke, *Phys. Rev. A* **38**, 3098 (1988).
- [21] J. P. Perdew and Y. Wang, **45**, 13244 (1992).
- [22] J. P. Perdew, K. Burke, and M. Ernzerhof, *Phys. Rev. Lett.* **77**, 3865 (1996).
- [23] V. I. Anisimov, J. Zaanen, and O. K. Andersen, *Phys. Rev. B* **44**, 943 (1991).
- [24] V. I. Anisimov, F. Aryasetiawan, and A. I. Lichtenstein, *J. Phys. Condens. Matter* **9**, 767 (1997).

- [25] A. D. Becke, *J. Chem. Phys.* **98**, 1372 (1993).
- [26] N. Troullier and J. L. Martins, *Phys. Rev. B* **43**, 1993 (1991).
- [27] D. Vanderbilt, *Phys. Rev. B* **41**, 7892 (1990).
- [28] P. E. Blöchl, *Phys. Rev. B* **50**, 17953 (1994).
- [29] H. J. Monkhorst and J. D. Pack, *Phys. Rev. B* **13**, 5188 (1976).
- [30] G. Kresse and J. Furthmüller, *Comput. Mater. Sci.* **6**, 15 (1996).
- [31] G. Kresse and J. Furthmüller, *Phys. Rev. B* **54**, 11169 (1996).
- [32] M. Methfessel and A. T. Paxton, *Phys. Rev. B* **40**, 3616 (1989).
- [33] P. E. Blöchl, O. Jepsen, and O. K. Andersen, *Phys. Rev. B* **49**, 16223 (1994).
- [34] J. R. Chelikowsky, N. Troullier, and Y. Saad, *Phys. Rev. Lett.* **72**, 1240 (1994).
- [35] M. Alemany, M. Jain, L. Kronik, and J. Chelikowsky, *Phys. Rev. B* **69**, 075101 (2004).
- [36] J. R. Chelikowsky, *J. Phys. D. Appl. Phys.* **33**, R33 (2000).
- [37] L. Kronik, A. Makmal, M. L. Tiago, M. M. G. Alemany, M. Jain, X. Huang, Y. Saad, and J. R. Chelikowsky, *Phys. Status Solidi Basic Res.* **243**, 1063 (2006).
- [38] C. J. Fall, N. Binggeli, and a. Baldereschi, *Phys. Rev. Lett.* **88**, 156802 (2002).
- [39] C. J. Fall, N. Binggeli, and a. Baldereschi, *Phys. Rev. B* **66**, 075405 (2002).
- [40] D. M. Wood, *Phys. Rev. Lett.* **46**, 749 (1981).
- [41] J. P. Perdew, *Phys. Rev. B* **37**, 6175 (1988).
- [42] J. Zhao, X. Chen, and G. Wang, *Eur. Lett* **28**, 311 (1994).
- [43] E. Roduner, *Chem. Soc. Rev.* **35**, 583 (2006).
- [44] G. D. Wilk, R. M. Wallace, and J. M. Anthony, *J. Appl. Phys.* **89**, 5243 (2001).
- [45] J. Robertson, *Eur. Phys. J. Appl. Phys.* **28**, 265 (2004).
- [46] D. G. Schlom and J. H. Haeni, *MRS Bull.* **27**, 198 (2002).
- [47] J. J. Yang, D. B. Strukov, and D. R. Stewart, *Nat. Nanotechnol.* **8**, 13 (2012).
- [48] J. Aarik, H. Mändar, M. Kirm, and L. Pung, *Thin Solid Films* **466**, 41 (2004).
- [49] P. K. de Boer and R. A. de Groot, *J. Phys. Condens. Matter* **10**, 10241 (1998).
- [50] X. Zhao and D. Vanderbilt, *Phys. Rev. B* **65**, 233106 (2002).
- [51] S. N. Tkachev, M. H. Manghnani, A. Niilisk, J. Aarik, and H. Mändar, *Spectrochim. Acta. A. Mol. Biomol. Spectrosc.* **61**, 2434 (2005).
- [52] P. E. Quintard, P. Barbéris, A. P. Mirgorodsky, and T. Merle-Méjean, *J. Am.*

- Ceram. Soc. **85**, 1745 (2004).
- [53] C. W. Li, M. M. McKerns, and B. Fultz, *Phys. Rev. B* **80**, 054304 (2009).
- [54] G. A. Kourouklis and E. Liarokapis, *J. Am. Ceram. Soc.* **74**, 520 (1991).
- [55] A. Debernardi and M. Fanciulli, *Mater. Sci. Semicond. Process.* **9**, 1014 (2006).
- [56] E. Cockayne, *Phys. Rev. B* **75**, 094103 (2007).
- [57] X. Luo, W. Zhou, S. V. Ushakov, A. Navrotsky, and A. A. Demkov, *Phys. Rev. B* **80**, 134119 (2009).
- [58] B. Zhou, H. Shi, X. D. Zhang, Q. Su, and Z. Y. Jiang, *J. Phys. D: Appl. Phys.* **47**, 115502 (2014).
- [59] J. Wang, H. P. Li, and R. Stevens, *J. Mater. Sci.* **27**, 5397 (1992).
- [60] H. Arashi, *J. Am. Ceram. Soc.* **75**, 844 (1992).
- [61] J. M. Leger, A. Atouf, P. E. Tomaszewski, and A. S. Pereira, *Phys. Rev. B* **48**, 93 (1993).
- [62] O. Ohtaka, H. Fukui, T. Kunisada, T. Fujisawa, K. Funakoshi, W. Utsumi, T. Irifune, K. Kuroda, and T. Kikegawa, *J. Am. Ceram. Soc.* **84**, 1369 (2004).
- [63] G. S. Belo, F. Nakagomi, A. Minko, S. W. da Silva, P. C. Morais, and D. A. Buchanan, *Appl. Surf. Sci.* **261**, 727 (2012).
- [64] S. Monaghan, P. K. Hurley, K. Cherkaoui, M. A. Negara, and A. Schenk, *Solid State Electron.* **53**, 438 (2009).
- [65] P. D. Kirsch, M. A. Quevedo-Lopez, H.-J. Li, Y. Senzaki, J. J. Peterson, S. C. Song, S. A. Krishnan, N. Moumen, J. Barnett, G. Bersuker, P. Y. Hung, B. H. Lee, T. Lafford, Q. Wang, D. Gay, and J. G. Ekerdt, *J. Appl. Phys.* **99**, 023508 (2006).
- [66] K. Kukli, M. Ritala, T. Pilvi, T. Aaltonen, J. Aarik, M. Lautala, and M. Leskelä, *Mater. Sci. Eng. B* **118**, 112 (2005).
- [67] E. Anastassakis, A. Pinczuk, E. Burstein, F. H. Pollak, and M. Cardona, *Solid State Commun.* **8**, 133 (1970).
- [68] Z. H. Ni, T. Yu, Y. H. Lu, Y. Y. Wang, Y. P. Feng, and Z. X. Shen, *ACS Nano* **2**, 2301 (2008).
- [69] F. J. Lopez, U. Givan, J. G. Connell, and L. J. Lauhon, *ACS Nano* **5**, 8958 (2011).
- [70] C. Rice, R. J. Young, R. Zan, U. Bangert, D. Wolverson, T. Georgiou, R. Jalil, and K. S. Novoselov, *Phys. Rev. B* **87**, 081307 (2013).
- [71] J. Buckeridge, D. O. Scanlon, A. Walsh, C. R. A. Catlow, and A. A. Sokol, *Phys. Rev. B* **87**, 214304 (2013).
- [72] M. K. Gupta, P. Goel, R. Mittal, N. Choudhury, and S. L. Chaplot, *Phys. Rev. B*

- 85**, 184304 (2012).
- [73] R. M. Fracchia, G. D. Barrera, N. L. Allan, T. H. K. Barron, and W. C. Mackrodt, *J. Phys. Chem. Solids* **59**, 435 (1998).
- [74] P. Broqvist and A. Pasquarello, *Appl. Phys. Lett.* **89**, 262904 (2006).
- [75] L. Goux, P. Czarnecki, Y. Y. Chen, L. Pantisano, X. P. Wang, R. Degraeve, B. Govoreanu, M. Jurczak, D. J. Wouters, and L. Altimime, *Appl. Phys. Lett.* **97**, 243509 (2010).
- [76] D. A. Tenne, I. E. Gonenli, A. Soukiassian, D. G. Schlom, S. M. Nakhmanson, K. M. Rabe, and X. X. Xi, *Phys. Rev. B* **76**, 024303 (2007).
- [77] E. Blokhin, R. a. Evarestov, D. Gryaznov, E. a. Kotomin, and J. Maier, *Phys. Rev. B* **88**, 241407 (2013).
- [78] J. Schaeffer, N. V Edwards, R. Liu, D. Roan, B. Hradsky, R. Gregory, J. Kulik, E. Duda, L. Contreras, J. Christiansen, S. Zollner, P. Tobin, B.-Y. Nguyen, R. Nieh, M. Ramon, R. Rao, R. Hegde, R. Rai, J. Baker, and S. Voight, *J. Electrochem. Soc.* **150**, F67 (2003).
- [79] M. Villanueva-Ibañez, C. Le Luyer, O. Marty, and J. Mugnier, *Opt. Mater. (Amst.)* **24**, 51 (2003).
- [80] M. Modreanu, J. Sancho-Parramon, O. Durand, B. Servet, M. Stchakovsky, C. Eypert, C. Naudin, A. Knowles, F. Bridou, and M.-F. Ravet, *Appl. Surf. Sci.* **253**, 328 (2006).
- [81] T. Tan, Z. Liu, H. Lu, W. Liu, and H. Tian, *Opt. Mater. (Amst.)* **32**, 432 (2010).
- [82] A. Togo, F. Oba, and I. Tanaka, *Phys. Rev. B* **78**, 134106 (2008).
- [83] P. Simoncic and A. Navrotsky, *J. Mater. Res.* **22**, 876 (2007).
- [84] T. A. Lee and A. Navrotsky, *J. Mater. Res.* **19**, 1855 (2004).
- [85] S. S. Todd, *J. Am. Chem. Soc.* **75**, 3035 (1953).
- [86] Q.-J. Liu, N.-C. Zhang, F.-S. Liu, and Z.-T. Liu, *Chinese Phys. B* **23**, 047101 (2014).
- [87] Y. Al-Khatatbeh, K. K. M. Lee, and B. Kiefer, *Phys. Rev. B* **82**, 144106 (2010).
- [88] D. M. Adams, S. Leonard, D. R. Russell, and R. J. Cernik, *J. Phys. Chem. Solids* **52**, 1181 (1991).
- [89] T. Tsuchiya, H. Imai, S. Miyoshi, P.-A. Glans, J. Guo, and S. Yamaguchi, *Phys. Chem. Chem. Phys.* **13**, 17013 (2011).
- [90] K. Xiong, J. Robertson, M. C. Gibson, and S. J. Clark, *Appl. Phys. Lett.* **87**, 183505 (2005).
- [91] J. W. Jiang and J. S. Wang, *Phys. Rev. B - Condens. Matter Mater. Phys.* **81**, 1

(2010).

- [92] A. Ohtomo and H. Y. Hwang, *Nature* **427**, 423 (2004).
- [93] S. Thiel, *Science* (80-.). **313**, 1942 (2006).
- [94] a Brinkman, M. Huijben, M. van Zalk, J. Huijben, U. Zeitler, J. C. Maan, W. G. van der Wiel, G. Rijnders, D. H. a Blank, and H. Hilgenkamp, *Nat. Mater.* **6**, 493 (2007).
- [95] N. Reyren, S. Thiel, A. D. Caviglia, L. F. Kourkoutis, G. Hammerl, C. Richter, C. W. Schneider, T. Kopp, A.-S. Rüetschi, D. Jaccard, M. Gabay, D. A. Muller, J.-M. Triscone, and J. Mannhart, *Science* **317**, 1196 (2007).
- [96] L. Li, C. Richter, J. Mannhart, and R. C. Ashoori, *Nat. Phys.* **7**, 762 (2011).
- [97] J. A. Bert, B. Kalisky, C. Bell, M. Kim, Y. Hikita, H. Y. Hwang, and K. a. Moler, *Nat. Phys.* **7**, 767 (2011).
- [98] N. Nakagawa, H. Y. Hwang, and D. A. Muller, *Nat. Mater.* **5**, 204 (2006).
- [99] A. Kalabukhov, R. Gunnarsson, J. Börjesson, E. Olsson, T. Claeson, and D. Winkler, *Phys. Rev. B* **75**, 121404 (2007).
- [100] G. Herranz, M. Basletić, M. Bibes, C. Carrétéro, E. Tafrá, E. Jacquet, K. Bouzehouane, C. Deranlot, A. Hamzić, J.-M. Broto, A. Barthélémy, and A. Fert, *Phys. Rev. Lett.* **98**, 216803 (2007).
- [101] L. Qiao, T. C. Droubay, V. Shutthanandan, Z. Zhu, P. V Sushko, and S. A. Chambers, *J. Phys. Condens. Matter* **22**, 312201 (2010).
- [102] S. A. Chambers, M. H. Engelhard, V. Shutthanandan, Z. Zhu, T. C. Droubay, L. Qiao, P. V. Sushko, T. Feng, H. D. Lee, T. Gustafsson, E. Garfunkel, A. B. Shah, J. M. Zuo, and Q. M. Ramasse, *Surf. Sci. Rep.* **65**, 317 (2010).
- [103] L. Qiao, T. C. Droubay, T. C. Kaspar, P. V. Sushko, and S. A. Chambers, *Surf. Sci.* **605**, 1381 (2011).
- [104] K. J. Kormondy, A. B. Posadas, T. Q. Ngo, S. Lu, N. Goble, J. Jordan-Sweet, X. P. A. Gao, D. J. Smith, M. R. McCartney, J. G. Ekerdt, and A. A. Demkov, *J. Appl. Phys.* **117**, 095303 (2015).
- [105] T. Q. Ngo, N. J. Goble, A. Posadas, K. J. Kormondy, S. Lu, M. D. McDaniel, J. Jordan-Sweet, D. J. Smith, X. P. A. Gao, A. A. Demkov, and J. G. Ekerdt, *J. Appl. Phys.* **118**, 115303 (2015).
- [106] A. F. Santander-Syro, O. Copie, T. Kondo, F. Fortuna, S. Pailhès, R. Weht, X. G. Qiu, F. Bertran, A. Nicolaou, A. Taleb-Ibrahimi, P. Le Fèvre, G. Herranz, M. Bibes, N. Reyren, Y. Apertet, P. Lecoeur, A. Barthélémy, and M. J. Rozenberg, *Nature* **469**, 189 (2011).
- [107] W. Meevasana, P. D. C. King, R. H. He, S.-K. Mo, M. Hashimoto, A. Tamai, P.

- Songsiriritthigul, F. Baumberger, and Z.-X. Shen, *Nat. Mater.* **10**, 114 (2011).
- [108] W. Sitaputra, N. Sivadas, M. Skowronski, D. Xiao, and R. M. Feenstra, *Phys. Rev. B* **91**, 205408 (2015).
- [109] D. D. Cuong, B. Lee, K. M. Choi, H. Ahn, S. Han, and J. Lee, *Phys. Rev. Lett.* **98**, 115503 (2007).
- [110] Y. S. Kim, J. Kim, S. J. Moon, W. S. Choi, Y. J. Chang, J.-G. Yoon, J. Yu, J.-S. Chung, and T. W. Noh, *Appl. Phys. Lett.* **94**, 202906 (2009).
- [111] Z. Hou and K. Terakura, *J. Phys. Soc. Japan* **79**, 114704 (2010).
- [112] C. Mitra, C. Lin, J. Robertson, and A. A. Demkov, *Phys. Rev. B* **86**, 155105 (2012).
- [113] J. Shen, H. Lee, R. Valentí, and H. O. Jeschke, *Phys. Rev. B* **86**, 195119 (2012).
- [114] A. Lopez-Bezaniilla, P. Ganesh, and P. B. Littlewood, *Phys. Rev. B* **92**, 115112 (2015).
- [115] C. Lin and A. A. Demkov, *Phys. Rev. Lett.* **111**, 217601 (2013).
- [116] F. Lechermann, W. Heckel, O. Kristanovski, and S. Müller, *Phys. Rev. B* **95**, 195159 (2017).
- [117] A. Mauger and C. Godart, *Phys. Rep.* **141**, 51 (1986).
- [118] J. Schoenes and P. Wachter, *Phys. Rev. B* **9**, 3097 (1974).
- [119] J. Lee, N. Sai, and A. A. Demkov, *Phys. Rev. B* **82**, 235305 (2010).
- [120] Y. Wang, M. K. Niranjana, J. D. Burton, J. M. An, K. D. Belashchenko, and E. Y. Tsybal, *Phys. Rev. B* **79**, 212408 (2009).
- [121] P. G. Steeneken, L. H. Tjeng, I. Elfimov, G. A. Sawatzky, G. Ghiringhelli, N. B. Brookes, and D.-J. Huang, *Phys. Rev. Lett.* **88**, 047201 (2002).
- [122] T. S. Santos and J. S. Moodera, *Phys. Rev. B* **69**, 241203 (2004).
- [123] H. X. Yang, A. Hallal, D. Terrade, X. Waintal, S. Roche, and M. Chshiev, *Phys. Rev. Lett.* **110**, 046603 (2013).
- [124] J. Qi, X. Li, Q. Niu, and J. Feng, *Phys. Rev. B* **92**, 121403 (2015).
- [125] A. G. Swartz, P. M. Odenthal, Y. Hao, R. S. Ruoff, and R. K. Kawakami, *ACS Nano* **6**, 10063 (2012).
- [126] J. C. Leutenantsmeyer, A. A. Kaverzin, M. Wojtaszek, and B. J. van Wees, *2D Mater.* **4**, 014001 (2016).
- [127] A. B. Posadas, K. J. Kormondy, W. Guo, P. Ponath, J. Geler-Kremer, T. Hadamek, and A. A. Demkov, *J. Appl. Phys.* **121**, 105302 (2017).
- [128] E. Pavarini, S. Biermann, A. Poteryaev, A. I. Lichtenstein, A. Georges, and O. K.

- Andersen, Phys. Rev. Lett. **92**, 176403 (2004).
- [129] M. Choi, F. Oba, and I. Tanaka, Phys. Rev. Lett. **103**, 185502 (2009).
- [130] H. O. Jeschke, J. Shen, and R. Valentí, New J. Phys. **17**, 23034 (2015).
- [131] E. Bousquet, N. A. Spaldin, and P. Ghosez, Phys. Rev. Lett. **104**, 037601 (2010).
- [132] W.-Y. Tong, H.-C. Ding, Y.-C. Gao, S.-J. Gong, X. Wan, and C.-G. Duan, Phys. Rev. B **89**, 064404 (2014).
- [133] D. G. Schlom, L.-Q. Chen, C.-B. Eom, K. M. Rabe, S. K. Streiffer, and J.-M. Triscone, Annu. Rev. Mater. Res. **37**, 589 (2007).
- [134] A. A. Demkov, Phys. Rev. B **74**, 085310 (2006).
- [135] C. Lin, C. Mitra, and A. A. Demkov, Phys. Rev. B **86**, 161102 (2012).
- [136] R. Pentcheva and W. E. Pickett, Phys. Rev. B **74**, 035112 (2006).
- [137] R. Pentcheva and W. E. Pickett, Phys. Rev. Lett. **99**, 016802 (2007).
- [138] J. Lee and A. A. Demkov, Phys. Rev. B **78**, 193104 (2008).
- [139] J.-S. Lee, Y. W. Xie, H. K. Sato, C. Bell, Y. Hikita, H. Y. Hwang, and C.-C. Kao, Nat. Mater. **12**, 703 (2013).
- [140] J. Hubbard, Proc. R. Soc. A Math. Phys. Eng. Sci. **276**, 238 (1963).
- [141] G. Khalsa and A. H. MacDonald, Phys. Rev. B **86**, 125121 (2012).
- [142] C. Cancellieri, M. L. Reinle-Schmitt, M. Kobayashi, V. N. Strocov, T. Schmitt, P. R. Willmott, S. Gariglio, and J. M. Triscone, Phys. Rev. Lett. **110**, 137601 (2013).
- [143] C. Cancellieri, A. S. Mishchenko, U. Aschauer, A. Filippetti, C. Faber, O. S. Barišić, V. A. Rogalev, T. Schmitt, N. Nagaosa, and V. N. Strocov, Nat. Commun. **7**, 10386 (2016).
- [144] M. M. Parish and P. B. Littlewood, Nature **426**, 162 (2003).
- [145] M. M. Parish and P. B. Littlewood, Phys. Rev. B **72**, 094417 (2005).
- [146] A. A. Abrikosov, Phys. Rev. B **58**, 2788 (1998).
- [147] A. A. Abrikosov, Europhys. Lett. **49**, 789 (2000).
- [148] N. Manyala, Y. Sidis, J. F. DiTusa, G. Aeppli, D. P. Young, and Z. Fisk, Nature **404**, 581 (2000).
- [149] A. Gerber, I. Kishon, I. Y. Korenblit, O. Riss, A. Segal, M. Karpovski, and B. Raquet, Phys. Rev. Lett. **99**, 27201 (2007).
- [150] Y. Onose, N. Takeshita, C. Terakura, H. Takagi, and Y. Tokura, Phys. Rev. B **72**, 224431 (2005).
- [151] Ziman J.M., *Principles of the Theory of Solids* (1972).

- [152] J.-M. Albina, M. Mrovec, B. Meyer, and C. Elsässer, *Phys. Rev. B* **76**, 165103 (2007).
- [153] L. Jaekwang and A. A. Demkov, *MRS Symp. Proc.* **966**, 0966 (2007).
- [154] R. Pentcheva and W. E. Pickett, *Phys. Rev. B* **78**, 205106 (2008).
- [155] J. Robertson and C. W. Chen, *Appl. Phys. Lett.* **74**, 1168 (1999).
- [156] J. Robertson, *J. Vac. Sci. Technol. B Microelectron. Nanom. Struct.* **18**, 1785 (2000).
- [157] W. Monch, *Surf. Sci.* **300**, 928 (1994).
- [158] P. W. Peacock and J. Robertson, *J. Appl. Phys.* **92**, 4712 (2002).
- [159] J. Tersoff, *Phys. Rev. Lett.* **52**, 465 (1984).
- [160] A. A. Demkov, L. R. C. Fonseca, E. Verret, J. Tomfohr, and O. F. Sankey, *Phys. Rev. B* **71**, 195306 (2005).
- [161] M. Choi, C. Lin, M. Butcher, C. Rodriguez, Q. He, A. B. Posadas, A. Y. Borisevich, S. Zollner, and A. A. Demkov, *Appl. Phys. Lett.* **106**, 192902 (2015).
- [162] C. Lin, A. Posadas, M. Choi, and A. A. Demkov, *J. Appl. Phys.* **117**, 034304 (2015).
- [163] J. E. Ortmann, N. Nookala, Q. He, L. Gao, C. Lin, A. B. Posadas, A. Y. Borisevich, and A. A. Demkov, (Unpublished) (n.d.).
- [164] M. S. Park, S. H. Rhim, and A. J. Freeman, *Phys. Rev. B* **74**, 205416 (2006).
- [165] N. C. Bristowe, E. Artacho, and P. B. Littlewood, *Phys. Rev. B* **80**, 045425 (2009).